The Pennsylvania State University

The Graduate School

DEVELOPMENT OF SELF-LUBRICATING COATINGS VIA COLD SPRAY

PROCESS: FEEDSTOCK FORMULATION AND DEFORMATION MODELING

A Thesis in

Engineering Science and Mechanics

by

Gaurav Aggarwal

Submitted in Partial Fulfillment

of the Requirements

for the Degree of

Doctor of Philosophy

August 2007

The thesis of Gaurav Aggarwal was reviewed and approved* by the following:

Ivica Smid
Associate Professor of Engineering Science and Mechanics
Co-Thesis Advisor, Co-Chair of Committee

Albert E. Segall
Associate Professor of Engineering Science and Mechanics
Co-Thesis Advisor, Co-Chair of Committee

Bernhard R. Tittmann
Schell Professor of Engineering Science and Mechanics

Robert Voigt
Professor of Industrial Engineering

Timothy J. Eden
Head of Materials Science Processing Division
Applied Research Laboratory
Special Member

Judith A. Todd
P. B. Breneman Department Head Chair
Head of the Department of Engineering Science and Mechanics

*Signatures are on file in the Graduate School

ABSTRACT

Because of their low density, high specific strength and high stiffness, titanium alloys are one of the prime candidates for structural application often requiring specific tribological properties. However, their relatively high friction coefficients and low wear resistance are limiting their application over a wider temperature range. Various coatings deposited with technologies like- high velocity oxy flame (HVOF), detonation gun (D-Gun), electron beam physical vapor deposition (EB-PVD), etc., can improve wear performance and decrease corrosion damage. These technologies require high processing temperatures precluding the integration of thermally vulnerable lubricants.

This research looks at a relatively new coating process called Cold Spray for self-lubricating coatings on Ti-6Al-4V alloys. Cold Spray can produce coatings without significant heating of the sprayed powder or substrate. The particles are in solid state as they hit the substrate, and the formation of coatings occurs mainly due to the kinetic energy of the particles. Therefore, the impact velocity plays an important role. Below a critical value, the particles can cause densification and abrasion of the substrate. The focus of this study is to design composite coatings for the cold spray process and determination of the critical velocity through finite element modeling.

Different powders and feedstock formulation techniques are discussed in order to find an optimum formulation for self-lubricating coatings. A composite powder (Ni coated hBN) was found to be the best candidate for the feedstock. The deformation of composite particles upon impact on the substrate was modeled and compared to the experiments. A number of approaches involving different modeling platforms, particle-

substrate geometries, and material models have been tried. This work presents the results of ANSYS (version 10.0) analysis using an axisymmetric model of the particle impact. Stress and strain distributions in the particle-substrate interface have been observed for a wide range of impact velocities (200 to 1000 m/s). The results are evaluated to predict particle size, lubricant content, and finally the critical velocities for composite particles during the cold spray process.

For the first time, the cold spray process is used to deposit $Ni-MoS_2$ and Ni-hBN self-lubricating coatings. The modeling results are matched with the experimental results to provide guidelines for composite coatings via cold spray processing.

TABLE OF CONTENTS

LIST OF FIGURES

LIST OF TABLES

ACKNOWLEDGEMENTS

First and foremost acknowledgment goes to my thesis advisor, Dr. Ivi Smid, for his expert guidance, encouragement, and support during the course of this research. He was available every time, whenever I needed him.

I express deep gratitude to my co-advisor Dr. Al Segall, who provided me with an opportunity to work on the project and his continuous guidance during its course. Thanks to Dr. Tim Eden for providing the cold spray facility and valuable suggestions during the course of this work.

I would like to thank my fellow graduate student Parul Walia for her constant support in this project. This work would not had been possible without the help of John Potter, Brock Golesich, and Bruce Gossard who helped me carry the cold spray experiments. Kristina Cowan and Lou Campbell at CISP were helpful with the characterization of the powders. Special thanks to Tim Dumm at Diamond Innovations for permitting me to travel to Penn State to finish up this work.

Thanks to all my friends for making my stay at Penn State rewarding and enjoyable. I would like to thank Nitesh, Rupi, Sheshu, Mahesh Papa, Pranav, and Jaskaran for their support.

Most of all, I'll like to thank my family- my parents, sister and my wife-Reeva, for their confidence in me. This effort would not have been possible without their love and support.

Chapter 1

Introduction

1.1 Cold Spray Process

Titanium alloys are promising candidates for tribological applications because of their low density, high specific strength, and high modulus. In addition to resistance to compressive failure and strength per unit weight, titanium alloys are resistant to most common forms of corrosion. However, titanium alloys have rather poor surface properties. In fact, fretting wear, a destructive phenomenon that occurs when two contacting surfaces oscillate at minute relative displacements, is prevalent in self-mating titanium contacts. Fretting wear often occurs at the blade/disk interface of fan and compressor stages in turbine engines when direct contact follows the breakdown of the protective coatings and/or lubrication. This occurs as a result of high coefficient of friction and low resistance to wear exhibited by titanium alloys.

As would be expected, there are many coating technologies currently available to improve the wear and friction characteristics of a surface either through increased hardness, added lubricity, or acting channels or reservoirs for lubricants. The most widely used methods include high velocity oxy-fuel (HVOF), detonation-guns, plasma spray, flame spray, arc spray, and electron-beam physical vapor deposition (EB-PVD). While

these methods have been successfully used to improve the wear performance, act as thermal barriers, and decrease corrosion damage, their application is not without problems because of the high depositions temperatures. Unfortunately, these temperatures often preclude coatings to the surfaces of any materials where phase transformations, excessive oxidation, evaporation, and/or crystallization are possible. Additional problems often arise from residual stresses and debonding induced by large temperature difference.

Due to many difficulties associated with traditional thermal spray methods, at the end of the 1980's, investigations into two-phase flow over bodies led to the development of a coating deposition method known as the cold spray process. The process is characterized by the solid-state, high-velocity impact of powder particles onto the substrate. High particle velocities are obtained by the acceleration of an expanding gas stream to velocities in the range of 500-1200 m/s in a converging-diverging nozzle. In this process, the gas is heated, without using combustion, only to increase the gas and particle velocity and to facilitate the deformation of particles upon impact. The particles are in solid-state as they hit the substrate and both the gas and particle temperature remain below the melting point of the spray material. Therefore, formation of coatings mainly occurs due to the kinetic energy of the particles. Because of its non-combustive nature, cold spray process is of great interest for spraying oxidation sensitive materials such as aluminum, copper, titanium and others. More importantly, the method allows the introduction of lower temperature lubricants directly into the coating with all the anticipated benefits for reducing friction and related wear damage. While the reduced deposition temperature is clearly a significant advantage in and of itself, there are

additional and important benefits as the cold spray process can also be used repeatedly to repair variety of surfaces, as well create functionally graded alloys and near net-shape components.

1.2 Necessity of Research

Given its tremendous and largely unexplored potential, cold sprays offers a number of intriguing possibilities for the reduction of friction and wear related damage. Earlier research on titanium dovetail and related fretting at elevated temperatures has shown the threat of fretting and protective benefit of solid film lubricant. In fact, there appears to be virtually no damage to the coatings as long as some lubricant remains intact. However, given the temperature limitations of most solid film lubricants, and relatively high operational temperatures experienced by the dovetail joints, the benefits are relatively short lived. Therefore, combining the best solid film lubricants with good high temperature and wear resistant material to form a new self-lubricating coating would offer tremendous potential at the necessary high temperature range.

There have been numerous studies exploring the relationships between the measured deposition efficiencies and the particle velocities as evaluated by semi-empirical methods and numerical modeling. These studies propose the existence of a critical particle velocity, below which impacting particles would only cause densification and abrasion of the substrate in a way similar to grit blasting or short peening. Finite element modeling of composite particle impact would offer an insight in determination of

critical particle velocity. The stress and strain distribution in particle & substrate will provide valuable information to optimize the actual process.

1.3 Research Objectives

Development of self-lubricating coatings for self-mating titanium contacts will prevent fretting wear and therefore, increase energy efficiency and component reliability in jet turbine engines. This requires retaining lubricants in the wear resistant coatings. The current research attempts to explore cold spray as a possible method, so as to allow the introduction of lower temperature lubricants directly into the coating and hence reduce friction and related wear damage. The overarching objective of this research has been to develop self-lubricating coatings via cold spray. This is mainly achieved with cold spray experiments. Based on the experiments, an optimized feedstock is selected, which is been used to build a finite-element model. The finite-element model is used to identify the critical particle velocity. The overarching objective of the research has been met by satisfying the following intermediate objectives.

- Understand the cold spray process particularly the impact modeling as it related to the determination of critical particle velocity. [Chapter 2]
- Formulate the feedstock for development of self-lubricating coatings via cold spray. [Chapter 3, 4]

- Identify the threshold lubricant content (wt%) in the feedstock for development of coatings. [Chapter 4, 6]

- Finite-element modeling of composite particle impact. [Chapter 5]

- Determination of stress and strains in particle and particle/substrate interface, to identify the critical particle velocity. [Chapter 6]

1.4 Organization of the Thesis

This thesis is divided into seven chapters. Chapter 2 begins with the history and design of jet turbine engines that is specifically of importance to dovetail joints. In addition, Chapter 2 reviews the basic cold spray process and prior studies done in the field of cold spray. Chapter 3 gives the details of the experimental procedures that have been used in this study, followed by the experimental results in Chapter 4. Chapter 5 gives the details of the model used to study the particle impact. Chapter 6 discusses the both the experimental and modeling results. Finally, the findings are summarized and conclusions made in Chapter 6 including future recommendations.

Chapter 2

Background

This chapter lays down the foundation of the key concepts in the creation of the hypothesis for this research. It presents the historical significance of jet turbine engines with the associated fretting wear. Various thermal spray methods for applying wear resistant coatings are discussed with their respective advantages and disadvantages. In particular, a relatively new coating process, Cold Spray is presented. A review of the past work in bonding mechanisms of cold spray and deformation modeling is discussed, leading up to the statement of hypothesis and it's significance for development of self-lubricating coatings.

2.1 History

The airplane age began at Kitty Hawk, North Carolina. Although the 1902 flyer was the first truly effective aircraft heavier than air, it didn't have a propulsion system, so it counts only as glider, not as an airplane. Powered flight began when two brothers, Wilbur and Orville Wright, invented and tested the first airplane on December 17, 1903. Since then, throughout the years, aviation has confronted engineers and researchers equally. With the advancement of technology, the demand for better, faster, and more

efficient aircraft has increased. The subsequent enthusiasm for aviation resulted into enormous activities, spanning many different disciplines. Even as modern aviation possesses a remarkable list of undertakings, the demand for better aircraft still exists and will continue to encourage the engineering community.

One of the most important inventions in aviation was the inception of the jet turbine engine. A French engineer, René Lorin, patented a jet propulsion engine in 1913, but was an Athodyd (aero-dynamic-duct, with no major rotating parts). From 1913 to the late 1930's the gas powered reciprocating internal combustion engine with a propeller was the sole means used to propel jet planes. It was Frank Whittle, a British pilot, who was granted his first patent in 1930 for using a gas turbine to produce a propulsive jet. The first Whittle engine, which featured a multistage compressor, a combustion chamber, single stage turbine and a nozzle, flew in April 1937. The first jet airplane to successfully use this type of engine was the German He 178 invented by Hans Von Ohain. Similar to an aircraft, the turbine engine has undergone many developmental stages since it's early days and had grown in complexity. However, its sophistication does not make it perfect without any flaws, and there is a continuing need for refinement. For example, complexity in design introduces a potential for wear in many moving components. Excessive wear can lead to engine failure and cause serious damage. Component replacement becomes compelling in cases where wear cannot be avoided. This frequent replacement has been a costly alternative and motivation behind finding new materials and measures to increase life in turbine engines.

2.2 Jet Turbine Engines

In the design of rotor discs, drums and blades of turbine engines, centrifugal forces dominate, requiring metals with the highest ratio of strength to density. This results in the lightest possible rotor assembly, which in turn reduces the forces on the engine structure enabling a further reduction in weight. For this reason, titanium alloys are the prime candidates because of their low density, high specific strength, and high modulus[1]. Approximately one third of the structural weight of modern turbine engines is made up of titanium. As higher temperature titanium alloys are developed and produced, they are progressively replacing nickel-alloys for discs and blades at the rear of the jet engine[2]. The ASTM figure of merit of materials has ranked titanium alloys ahead of conventional bearing steels in tribological applications. Due to the above properties, high-strength titanium alloys are used in critical rotating components of gas turbine engines. Particular examples include fan and compressor sections of many jet turbine engines in which dovetail joints are used to attach the titanium fan and compressor blades to the titanium disks within the engine Figure **2.1**. As fan and compressor sections of the engine are at or near the intake, floating debris entering into the engine often damages these blades during normal operation. The dovetail joint allows for the replacement of a single blade if damage from a foreign object occurs. Dovetail joints made of Ti-alloys, exhibit good resistance to compressive failures and the most common forms of corrosion. However, dovetail joints create a problem resulting from titanium-on-titanium contact within the joints. Titanium alloys have high coefficients of friction, low resistance to wear, and are not effectively lubricated by conventional liquids,

greases, and solid lubricants[3]. As a result dovetail joints promote fretting wear, a destructive wear mechanism that drastically reduces fatigue resistance of a component causing premature failure.
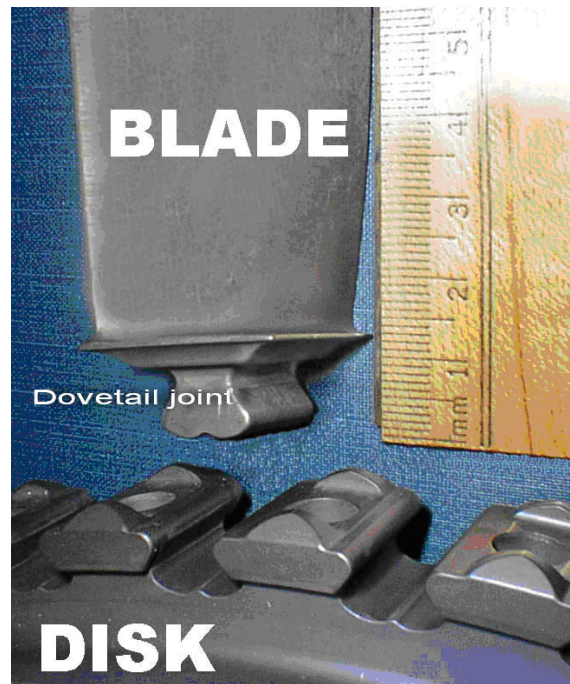
Figure **2.1**: Dovetail joint in the blade/disk interface

2.3 Fretting

Fretting is both complex in its definition and phenomenon. It is important to understand it before any preventive measures can be taken. According to the ASM glossary of terms, fretting is a damage which results from small amplitude oscillatory

motion, usually tangential, between two solid surfaces in contact[4]. Other authors describe it as a combination of wear and fatigue, or differentiate it from wear by the facts that the relative velocity of the two surfaces is much lower than usually encountered in wear[5]. The term fretting corrosion is used due to the nature of the degradation, often with the presence of oxide debris or a predominant chemical reaction[6]. However, it differs from corrosion, since the two surfaces are never brought out of contact and there is no chance for corrosion products to be removed. Fretting, wear and combined 'fretting wear' occur when the movement is the result of external vibrations applied to surfaces not submitted to impose displacement. If the relative movement is a consequence of a cyclic loading of one of the components, loading is called 'fretting fatigue'[6]. In short, fretting is caused by a combination of mechanical and chemical effects. Metal is removed from the surface either by a grinding action or by alternate welding and tearing away of the high spots. The removed particles become oxidized and form an abrasive powder which continues the destructive process. Oxidation of the metal surface occurs and the oxide film is destroyed by the relative motion of the surfaces. it can be concluded that fretting is a synergistic combination of wear, corrosion and fatigue phenomena driven by small relative displacement of two surfaces in contact.

In the early 20th century, deleterious effects of fretting on fatigue life were recognized[7]. However, despite extensive research efforts there are still points of contention about the operating mechanisms. Due to fretting action, fretting-fatigue failure initially begins as a surface and near surface damage. This damage results in considerable plastic strain at the surface[8, 9], disruption of surface films or oxides[10] and material transfer[11]. The disruption of surface films enhances direct metal to metal contact,

leading to micro-welding of the surfaces, and eventually high local shear forces. The continuous generation-destruction cycle of the oxide may produce particles that act as an abrasive third body to produce fretting wear and initiate cracks[12]. These cracks can be located at the contact edge of the fretted region[13, 14], on the boundary between displaced and non-displaced[15], or in the center of the specimen[8, 16, 17]. Some of these initiated cracks propagate through the specimen while others remain dormant[18]. The propagation of the cracks into the specimen is generally at an oblique angle[15, 18, 19] influenced by fretting action[19, 20], normal pressure[21, 22] and alternating stresses. With the progression of cracks into the material, fretting influence decreases[13] and the rate of crack growth depends on the alternating stresses. Titanium alloys in highly stressed regions are known to be particularly susceptible to fretting-initiated fatigue[23-25]. This may be because titanium alloys exhibit a greater tendency for material transfer when sliding over other materials or over itself. The above problems can be tackled by various methods, including applying wear resistant coatings on titanium alloys by thermal spray.

2.4 Thermal Spray Methods

Thermal spraying constitutes coating processes in which particulate metallic or non-metallic materials in a molten or semi-molten condition are deposited to form a coating[26]. Thermal spray processes can be divided based upon the heat source, into flame spraying and electric spraying. Flame spraying is based on gas combustion used at 1000° to 3000°C, and can be classified on the condition of the powder to be sprayed.

Electrical spray methods use electrical energy and include non-transferred arc plasma, RF plasma, and wire arc. The most promising electric spray method is deposition. Plasma arc spraying is a thermal spray process in which a non-transferred arc is the source of heat that ionizes a gas which melts the coating material and propels it to the work piece[26]. In the gas flame-spray method a velocity of 50 to 100 m/s is imparted to powder particles, and the surface is treated with the gas and powder flow containing fused particles which results in coating. The low values of velocity and temperature of the applied particles is a major disadvantage of this process. Another flame spraying method, called detonation (D-gun) flame spraying eliminates these disadvantages in part. In a D-gun, the energy of detonating gases (mainly a mixture of acetylene and oxygen) at 2000° to 3500°C is used resulting in a substantial increase of particle velocities to 400 to 700 m/s. This method has low productivity because shock waves and tailing gas flow cause a high level of thermal and dynamic pulse effects on the product.

The plasma spray method takes care of the above disadvantages and is applied to powder particles in a size range of 40 to 100μm. In this, powder particles are heated to their melting point or higher and accelerated by the plasma jet gas flow, which is directed to the substrate. Upon impingement, the powder particles interact with the substrate surface thus forming the coating. This process results in local heating, oxidation and thermal deformation because of the high-temperature plasma jet used to accelerate powder particles. The high temperature jet also intensifies chemical and thermal processes leading to phase transformations and appearance of over-saturated and non-stoichiometeric structures. The process of acceleration is not efficient in plasma spray, as with increment in temperature of the plasma jet, the plasma density linearly decrease as

compared to gas density. Therefore, with a plasma jet velocity of 1000 to 2000 m/s

(which is approximately in the range of sonic velocity), the particles are accelerated only

up to 50 to 200 m/s. The intense heat involved in the above process limits the use of fine

powders (< 10μm), as they are heated above the melting point and material intensively

evaporates. Plasma spray also has the following disadvantages regarding the use of its

equipment: short service life of the nozzle (15 to 100 hours); inefficient acceleration of

the deposited particles because the nozzle design is not optimal and is subjected to

changes entailed by the electrical erosion of the inner duct, jamming of drum-type

metering feeder caused by the powder getting into the space between moving parts.

2.5 Cold Spray: 1980-present

2.5.1 Background of Technology

The thermal spray processes just discussed presented a challenge to provide a

method and apparatus for coating, without local heating, oxidation, phase transformation,

and appearance of oversaturated structures, and thereby preserving the initial structure of

powder material. An efficient process was therefore required which could prevent

evaporation of fine powders with particle sizes from 1 to 10μm, a low level of thermal

and erosion exposure of the apparatus, prolonged equipment life up to 1000 hours

without using expensive refractory and erosion-resistant materials, and the operation of

the duct for the powder particles acceleration being improved and operation reliability of the metering feeder being enhanced, even in metering fine powder fractions.

A relatively new thermal spray process which meets the above challenges, known as the Cold Spray process, was introduced to produce metal, alloy, and composite coatings with superior qualities. Cold spray, also known as "cold gas dynamic spray," and a high-velocity non-combustion spraying," was originally developed by chance in the mid-1980's at the Institute of Theoretical and Applied Mechanics of the Siberian Division of the Russian Academy of Science in Novosibirsk. While conducting experiments involving mounted solid models in a supersonic wind tunnel with particle-laden flows, researchers noted that with the increase in the flow velocity there is a transition from abrasion and erosion of the models by particles to deposition on the leading edges. Though this phenomenon may also have been observed earlier under similar conditions, the Russian investigators recognized its potential, and they developed a spray coating device based on this principle[27]. A U.S. patent for this process was issued in 1994[28], and the European patent in 1995[29]. In the United States, initial research in this field was conducted by a consortium formed under the auspices of the National Center for Manufacturing Sciences (NCMS) of Ann Arbor, MI. The membership included major U.S. companies such as Ford Motor Company, General Motors, General Electric- Aircraft Engines, and Pratt & Whitney Division of United Technologies. Sandia National Laboratories (SNL) and Penn State University (PSU) have taken up small development activities with funds available from above listed private companies. The last few years have seen exponential growth of the cold spray technology around the globe[30-56].

2.5.2 Cold Spray Process

Figure **2.2** shows a typical cold spray device. Compressed gas (nitrogen, helium, or air) is introduced to a heater and a powder feeder. The pressure gas (1-3 MPa) is expanded through a converging-diverging or de'Laval-type nozzle where it leaves the nozzle at a supersonic speed (300-1200 m/s). The powder particles are metered into the gas flow immediately upstream of the converging section of the nozzle and are accelerated by the rapidly expanding gas. The powder velocity ranges from 180-1000 m/s depending on particle size and material. The incoming compressed gas can be introduced at room temperature, or it can be preheated in order to achieve higher velocities.
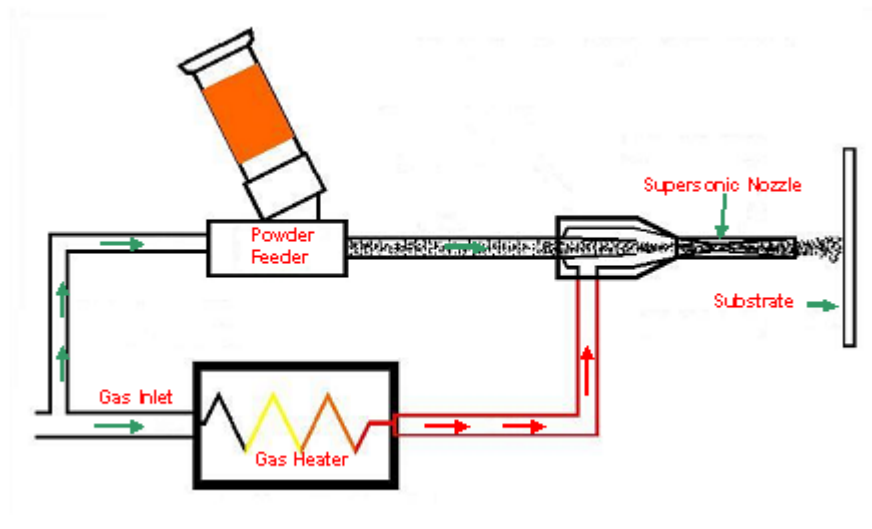
Figure **2.2**: Schematic of cold spray process

The preheating of gas increases the particle temperature and the velocity, both effects improve the deposition efficiency[56]. However, the gas temperature at the inlet is clearly below the melting temperature of the coating material, so the particles will not melt in the gas jet. Although preheat temperatures as high as 900K are sometimes used, the gas rapidly cools as it expands in the diverging section of the nozzle. As they accelerate, the particles begin to cool. But because the residence time in the nozzle is short, the temperature decrease is relatively small.

- the particles impact and bond to the substrate located approximately 25 mm from the exit plane of the nozzle. The distance from the nozzle can be adjusted to change the width of the coating and deposition efficiency. As cold spray does not use a high temperature heat source, such as flame or plasma to melt the feed material, it generally offers a number of advantage over the conventional thermal spray technologies. The most important advantages of cold spray is that: the amount of heat involved in the process is relatively small so that microstructural changes in the substrate material are minimal or non-existent.

- due to the absence of in-flight oxidation and other chemical reactions, thermally- and oxygen-sensitive depositing materials (e.g. copper or titanium) can be cold sprayed without significant material degradation.

- nanophase, intermetallic and amorphous materials, which are not amenable to conventional thermal-spray processes (due to major degradation of the depositing material), can be cold sprayed. grain growth and formation of the embrittling phases are generally avoided.

- macro- and microsegregations of the alloying elements during solidification that accompany conventional thermal-spray techniques, and can considerably compromise materials' properties do not develop during cold spraying. Consequently, attractive feed-powder properties are retained in cold-sprayed bulk materials.

- The ''peening'' effect of the impinging solid particles can induce beneficial compressive stresses in cold-spray deposited materials[57] in contrast to the highly detrimental tensile residual stresses induced by solidification shrinkage accompanying the conventional thermal spray processes.

- cold spray of materials like copper, solder, and polymeric coatings offers exciting new possibilities for cost-effective and environmentally friendly alternatives to electroplating, soldering, and painting[58].

One of the important limitations of cold spray is that the process is a line-of-sight process. Further, not all materials can be cold sprayed; ceramics and other non-ductile materials do not seem amenable. The deposition efficiency is strongly dependent on particle velocity[59]. It is difficult to achieve high-particle-impact velocities with dense materials like tungsten.

2.5.3 Bonding Mechanisms

The actual bonding mechanisms in cold spray are not fully understood and difficult to study because of the small particle sizes of the feedstock material (of the order

of a few microns), the short period of interaction ($\sim 10^{-8}$ s) and the uncertain phases of the interacting objects in micro volumes near the contact boundaries[60]. It is generally accepted in thermal spray coatings that the bonding strength is controlled by three main forces caused by mechanical, physical, and metallic interactions[61-63]. One, or the combination of these interactions have been found to be possible bonding mechanism. However, in cold spray, it seems reasonable that the feedstock particles and the substrate/deposited material undergo an extensive localized deformation during impact. This plastic deformation may disrupt thin surface films, such as oxides, and provide intimate conformal contact between the particles and the substrate/deposited material. The intimate conformal contact of clean surfaces combined with high contact pressures promote bonding[64, 65]. Therefore, bonding of particles in cold spray is acknowledged to be the result of severe plastic deformation and associated phenomena at the interface[30, 66-68].

Various researchers have reported the bonding mechanisms in cold spray to be related to those in processes such as explosive welding or shock wave powder compaction[67-70]. The bonding mechanisms of these latter processes have been well studied with their respective applications[71-74]. In explosive welding, bonding occurs at certain impact angles, impact velocities and material properties, and it is generally manifested by the formation of a solid-state jet of metal at the impact point of two metal plates. Within a distance of a few millimeters from the interface, there is a sequence of regions of severe deformation, highly elongated grains, recrystallized grains, and sometimes resolidified microstructures, though melting and resoldification are often limited to a thickness of less than a micrometer at the interface[75]. In explosive shock

wave powder consolidation, successful bonding has been related to severe plastic deformation at the particle/particle interface[76, 77]. Microstructures of some nickel-base alloys indicate formation of amorphous phases due to rapid cooling[78]. There is also proof of formation of a high-speed jet at the particle/particle interface in powder compaction studies[76, 79]. The craters created in the cold spray process reveal evidence of similar jet formation. The crater geometry has also been related to the success of bonding[67]. In general, crater lips appear sharper in the craters where the particle has bonded, whereas empty craters appear smoother.

Regardless of the existing analogies among the above mentioned processes, it has not yet become clear as to what extent the concepts of explosive cladding or shock wave powder consolidation can be applied to cold gas spraying. Few studies have explored the interfacial bonding mechanisms in cold spray and held the above mechanisms in perspective[53, 64]. However, investigation showed that explosive powder compaction is suitable to determine critical conditions for bonding materials which have a potential for applications in cold spraying[80]. As discussed earlier, interfacial melting may occur and enhance the particle/substrate interfacial bonding but it is not believed to be a major factor controlling the bonding strength. Formation of a solid-state jet of metal at the impact point and high pressures are generally considered as prerequisites for good particle/substrate bonding. Although these factors are critical for attaining clean particle and substrate surfaces and an intimate contact between them, they do not per se offer any insight into the character of the dominant mechanisms of interfacial bonding under cold-spray conditions.

The most often cited particle/substrate bonding mechanisms under the dynamic cold-spray conditions are atomic diffusion, surface adhesion, and plastic deformation. As particle/substrate contact times are very short, atomic diffusion is not expected to play a significant role in particle/substrate bonding. This can be explained using the Al-Cu inter-diffusion coefficient (=10^{-15} to 10^{-14} m^2/s[81]), the atomic inter-diffusion distance, during the time period of ~20 ns over which the particle/substrate interface is subjected to the highest temperatures, is found to be only 0.004-0.1 nm. Since this distance is only a fraction of the inter-atomic distance, atomic diffusion at the particle/substrate interface should be excluded as a dominant particle/substrate bonding mechanisms under dynamic cold-spray deposition conditions. Adhesion is a nano-length scale phenomenon and its occurrence requires clean surfaces and relatively high contact pressures to make the surfaces mutually conformal. The strength of adhesion then depends on the (attractive or repulsive) character of the atomic interactions and crystallographic details of the interface. Atomic scale simulations can model adhesion, but this is an involved task; one can generally infer the character of atomic interaction by examining the corresponding binary phase diagram. Specifically, the existence of solubility limits indicates repulsive atomic interactions, while the formation of an intermediate or intermetallic compound is an indication of attractive atomic interactions. In addition to the above factors, the overall strength of adhesion based particle/substrate bonding depends on the size of the particle substrate interfacial area. It is generally observed that stronger bonding occurs when the interfaces are wavy and when it contains vortex-like features. This observation can be, at least partly, attributed to the associated increase in the interfacial area. As discussed in the context of explosive welding[74], interfacial perturbations (roll-ups and vortices) can

give rise to nano/microscale material mixing and mechanical interlocking, both of which enhance the interfacial bonding. Plastic deformation is generally considered to be a mechanism for energy dissipation, i.e. a source of heat in the interfacial region. However, as shown earlier, increased temperature in the interfacial region is not sufficient to enhance interfacial melting or atomic diffusion to a level at which they act as dominant interfacial bonding mechanisms.

Grujicic *et al.*[64, 82] discuss the role of interfacial instability as a possible bonding mechanism in the cold-spray process. They suggest two interfacial instability-based mechanisms by which mixing/interlocking may occur. The first is the Kelvin-Helmholtz instability phenomenon, which arises when two fluids are in contact and moving at different velocities in a direction parallel to their interface. Instability can occur even if the two fluids have identical densities. When the interface is subjected to a perturbation a centrifugal force is generated as one fluid flows around the other. This, in turn gives rise to a change in pressure which may promote amplification of the interfacial perturbation. These instabilities may subsequently lead to the formation of interfacial roll-ups and vortices may enhance the overall strength of interfacial bonding by at least three ways: (a) by significantly increasing the interfacial area available for adhesion; (b) by producing fine length-scale mixing of the two materials; and (c) by creating mechanical interlocking between two materials. Interfacial instabilities can also be explained within the context of inertial instabilities. In this phenomena, flow inertia acts to promote the instability and viscosity acts to dampen it. The ratio of these two effects determines if the instability actually grows or decays and is quantified by the Reynolds number as Equation **2.1**

$$R_e = \frac{UL}{v}$$
(2.1)

where U is the characteristic velocity, L is the characteristic length scale, and v (=μ(dynamic viscosity)/ρ(density)) is the kinematic viscosity. For the situation considered here, the characteristic velocity would be the particle impact velocity which is on the order of 1000 m/s, and a characteristic length scale would be the particle diameter which is on the order of 10 μm. The values of dynamic viscosity cited earlier range from 10^5 to 10^6 Pa·s, which translates to a kinematic viscosity of 100 m²/s, assuming a metal density of 1000 kg/m³. Using these numbers, a value of $R_e \sim 10^{-4}$ is obtained. Since instabilities arise when the Reynolds number is larger than one, inertial instability is not expected to occur in the present situation, notwithstanding the rather rough estimates of length, velocity and kinematic viscosity. Grucijic *et al.* [82] also suggested the creation of a 'rivet-like particle/cavity assembly' as a possible topological bonding mechanism. They suggest that the cavity formed by the impact is reentrant, and it prevents the particles to separate from the substrate, see Figure **2.3**.
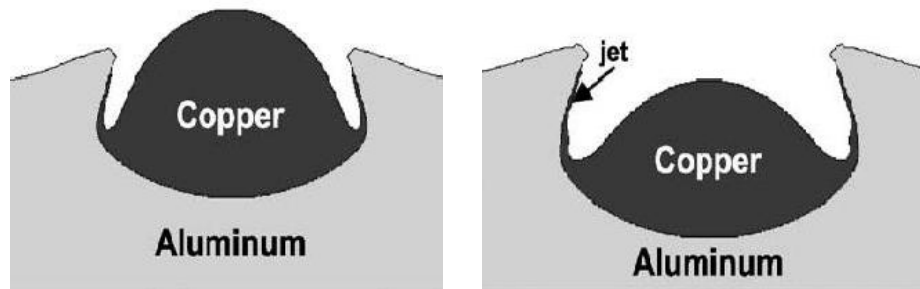
Figure **2.3**: Substrate-crater shapes during an impact

2.5.4 Critical Particle Velocity

The above discussions show that the mechanisms of adhesion are still not well known in cold spray coating. As such, the aforementioned hypotheses, though unproven, are consistent with the fact that a wide range of ductile materials such as metals and polymers have been cold-spray deposited. These theories also explain the requirement of certain minimum critical velocity necessary for plastic deformation resulting in adhesion. Calculations indicate that the particle kinetic energy at the impact is typically much less than the energy required to melt the particle, suggesting that the deposition mechanism is mainly a solid-state process[35, 59, 82-84]. The lack of melting is also confirmed by micrographs of cold-sprayed materials[85].

There have been numerous studies exploring the relationships between the measured deposition efficiencies and the particle velocities as evaluated by semi-empirical methods and numerical modeling[57, 84, 86, 87]. These studies propose the existence of a critical particle velocity, below which impacting particles would only cause densification and abrasion of the substrate, in a way similar to that in grit blasting or shot peening.

As the particle velocity is so critical for the success of cold-spray deposition, it is pivotal to develop a sound understanding of the factors on which the critical velocity depends. The critical velocity is specific to the geometry and material, i.e. it would depend on particle size, melting temperature, ductility, density, etc. of the powder. It also

depends on the particle temperature at the time of impact, which in turn depends on the

working/carrier gas involved. The critical velocity in the cold spray process is mainly

limited by the carrier gas velocity[59]. The use of a high pressure gas flow, long nozzles,

and small particles results in a particle traveling nearly at the gas velocity. The gas-flow

model developed by Dykhuizen and Smith[59] assumes: (a) gas to be isentropic

(adiabatic and frictionless) and one-dimensional; (b) carrier gas to be a perfect gas with

constant specific heats, and will not be discussed in detail here. However, the gas velocity

at the nozzle throat is equal to the speed of sound and defined as Equation **2.2**

$$v = \sqrt{\gamma R T^*} \qquad\qquad (2.2)$$

where γ is the ratio of the constant-pressure and the constant-volume specific heats which

is typically set to 1.66 for monoatomic gases like helium, and to 1.4 for diatomic gases

like nitrogen and oxygen, respectively, R is the specific gas constant (universal gas

constant divided by the gas molecular weight), and T^* is the gas temperature in the throat.

Hence, Equation **2.2** demonstrates why helium, with its slightly larger ratio of specific

heats and substantially lower molecular weight would be expected to provide

significantly higher gas velocities than air (mixture of nitrogen and oxygen), and

consequently, higher particle velocities. Equation **2.2** also shows that the critical velocity

increases with gas temperature at the throat. Since T^* is directly proportional to the inlet

gas temperature for a given working gas (i.e. constant γ), the particle velocity increases

monotonically with inlet gas temperature. Raising the temperature to achieve higher

particle velocities decreases the gas density, thereby, decreasing the gas consumption.

While not as significant as gas temperature, the gas pressure also helps in increasing the particle velocity[35]; the gas pressure does not affect the critical velocity directly, but increasing the gas pressure increases the density of the gas in the nozzle. A denser gas exerts greater drag forces on the particles, resulting in more effective particle acceleration over a given nozzle length. But this leads to an increase in consumption of the process gas. According to the particle acceleration model[59], particle acceleration increases with gas velocity and gas density. However, according to gas-dynamic equations, the gas density decreases as the gas velocity increases through the supersonic nozzle. Thus there exists an optimal condition that maximizes acceleration, and can be obtained by determining a maximum drag force on the particle. It has been proved, both analytically and experimentally that a relative gas velocity of Mach$\sqrt{2}$ yields the optimal gas density and gas velocity that maximizes spray acceleration[59].

2.5.5 Modeling of Deformation

In cold spray, processing techniques do not allow a precise description of each impact. The impact velocity corresponding to an individual crater is also not available. Fortunately, the use of modeling can provide the definition of each impacting event and allow variation of any parameter to obtain trends. The first numerical model to investigate the impact process in cold spray was conducted by Sandia National Laboratory [67]; they used a computer code CTH[88], developed to model a wide range of solid dynamics problems involving shock wave propagation and material motion in one, two, or three dimensions. These codes employ a two step Eulerian scheme, where

the first step is the Lagrangian step in which the cells distort to follow the material motion. The next step is to remesh, where the distorted cells are mapped back to the original Eulerian mesh. This modeling was done with 2-D axisymmtery, as a normal impact of fully dense spherical particles was assumed. The substrate was modeled using the Steinberg-Guinan-Lund viscoplastic model[89, 90]. While the Zerilli-Armstrong model[91] was used for the impacting particles. These simulations proposed that greater impact velocities result in deeper craters; large deformations caused by the solid state jetting of both substrate and particle from the crater promoted bonding of the particle to the substrate. The jetting can be related to the shock wave propagation in particle and substrate[92]. This model predicted the peak temperature at each impact, but these temperatures were overestimated because CTH does not model dissipation of heat via conduction. Also the code cannot be used to determine the critical velocity for bonding as it assumes that all contacting surfaces result in an intimate bond between the layers. Most models predicted the jetting phenomenon for numerous particles and different materials, but deformation modeling of particle impacting a rigid barrier by Alkhimov *et al.*[60] at the Institute of Theoretical and Applied Mechanics of the Siberian Division of the Russian Academy of Science predicted formation of a lamina of melted metal, in which the temperature is close to the melting point of the particle.

Melting at the bonding interface has also been documented for materials such as Ti-6Al-4V[93]. The formation of this layer resulted in adhesion of particles. The numerical model was based on the Lagrangian approach and Prandtl-Reuss mathematical model of an elastoplastic material in flow. The rationale behind modeling of the substrate as a rigid wall was provided in one of their recent reports[68], in which they predicted

that for metal particles (< 50 μm) heat transfer during contact is essential and adiabatic conditions usually applied in modeling of impact deformation of macro-bodies is not justified. Papyrin *et al.* [94] suggested another physical model based on a comparison of adhesion energy and energy of elastic deformation generated under the particle impact. They showed that particles adhere to the substrate only if the energy of adhesion exceeds the energy of elastic deformation. This model just presented a qualitative explanation of some regularities of adhesion between particle and substrate.

Ruling out the above prediction about adiabatic condition, Borchers *et al.*[66] carried out the first finite element modeling (FEM) of the dynamic deformation of the particles upon impact using ABAQUS. The analysis accounted for strain hardening, heat dissipation due to plastic deformation, and thermal softening. The results revealed high values for both strain and flow stress at the particle surface for low particle velocities (v = 300 m/s). The authors also mentioned adiabatic shear instabilities because at high velocities (v = 900 m/s) analyses indicated high plastic strains but flow stresses fell to zero at the surface. Various assumptions and results were mentioned but no clear explanation was provided for the occurrence of adiabatic shear instability (see Figure 2.4).

In another work, the results of modeling showed a change in almost all key parameters near the particle interface with the beginning of adiabatic shear instability at the interface[69]. Adiabatic shear instability which results from high strain rate deformation can be a cause for failure of mechanical components. In cold spray, this occurs close to the experimentally evaluated critical velocity[84]. Correspondingly, a criterion for bonding can be formulated by taking the critical velocity as being the same

as that required for reaching adiabatic shear instability. This allows the prediction of the critical velocity for a given material and particle temperature. Figure **2.4** shows a change in trend of variation of strain with time, indicating shear instability.
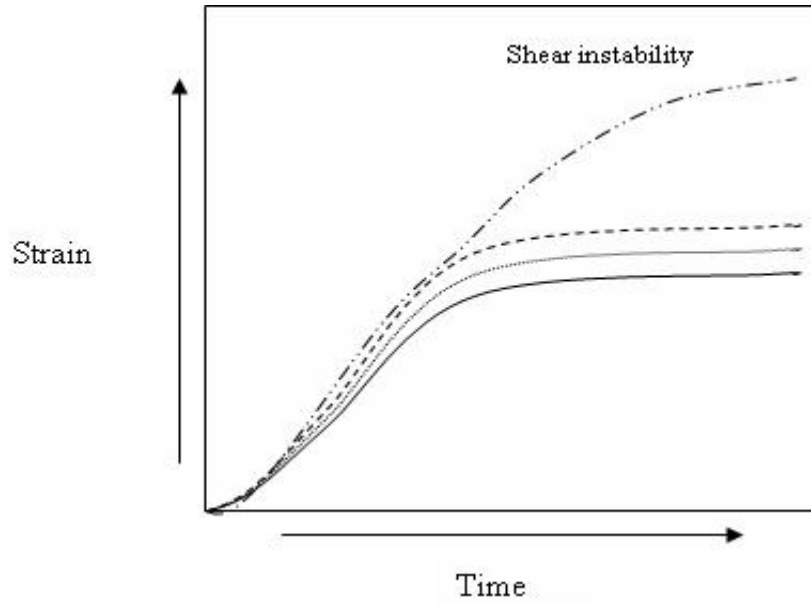
Figure **2.4**: Schematic indicating shear instability

Modeling of particle deformation by Assadi *et al.*[83] is based on the assumption of adiabatic heating in the cold spray process. This assumption can be assessed with respect to the value of the dimensionless parameter $x^2/D_{th}t$, in which x is a characteristic system dimension, D_{th} is the thermal diffusitivity and t is the process time[95]. For the typical values $D_{th} = 10^{-6}$ m^2/s, $t = 10^{-8}$ s and $x = 10^{-6}$ m, the parameter $x^2/D_{th}t$ goes well above unity, hence justifying the assumption of adiabatic heating. It was further shown that the adiabatic assumption made is justified for smaller particles, even if the value of $x^2/D_{th}t$ parameter falls below unity. At very small length scales, heat conduction would be dominated by a wave propagation mechanism rather than by diffusion[96]. This

implies that with decreasing particle size, the speed of the heat propagation would approach that of plastic waves, and would in any case be limited by the speed of sound in the particle. Therefore, for high speed impact of much smaller particles, heat conduction could be even slower than predicted by the diffusive heat equation. Adiabatic heating is also supported by the dependence of kinetic energy dissipation into heat on strain rate, i.e., the fraction of plastic work dissipated into heat would be larger for higher strain rates.

Considering the above assumptions, some authors have performed modeling using the finite element program ABAQUS/Explicit, Version 6.2[97] and 6.3[98]. Analyses have been performed using axisymmteric 3-D models of particle impact, with various parameter combinations concerning element type, initial and adaptive meshing, contact interaction, etc. Here work by Assadi *et al.*[83] will be discussed in detail who used the Johnson-Cook plasticity [99] to model plastic response of the material. The elastic response of the material was assumed to follow linear elasticity which was compared to a linear Mie-Gruneisen equation of state (EOS). For axisymmteric analyses, they used 4-node elements, and 4-node linear tetrahedron elements for 3-D analyses. The initial impact velocity was taken as prime input variable. They observed non-conserving energy variation of the output set and unphysical shape of the out flowing jet of material at the interface by frequent remeshing for moderate and high particle impact velocities. The deformation pattern and the key field variables were examined generally throughout the particle and substrate, but also particularly along various paths within the particle, Figure **2.5.** In **Figure 2.5**, the substrate has no degree of freedom at the bottom, but can slide in the vertical directions at the lateral edges (axisymmteric edge). The simulation

results gave the temperature distribution and the magnitude of velocity at the respective surfaces. The velocity of the node at the particle surface was twice the impact velocity, which was concluded as a measure to indicate jet formation.
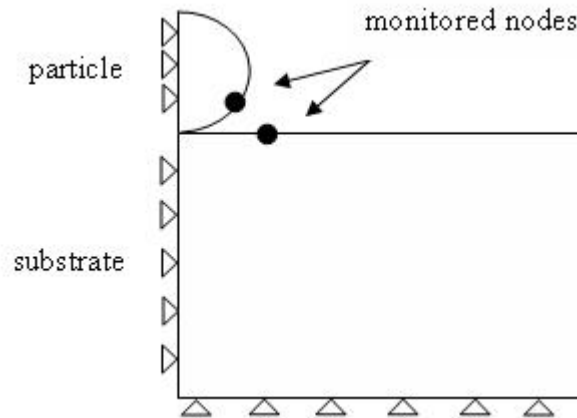
Figure **2.5**: Initial configuration and boundary conditions for axisymmetric geometry

Modeling also showed adiabatic shear instability as for a higher velocity (= 900 m/s) the shear stress in the particle fell to zero at the interface. For this velocity, despite the higher magnitude of plastic strain at the interface, the shear strength of the material falls to values near zero due to dominance of thermal softening over hardening effects Figure **2.6**. The effect of element size at the interface was discussed too; higher temperatures were obtained when a finer mesh was chosen. This problem was alleviated by extrapolating the temperature to zero element size and using this value as the corresponding threshold of adiabatic shear instability. To determine the extent of plastic deformation and viscous flow at the interface, equivalent plastic strain along the meridian path on the particle surface was applied. The authors also performed a 3-dimensional

simulation to simulate interaction of particles during deposition. The above work

demonstrated that the plastic deformation phenomenon in cold spray can be modeled

appropriately through finite element analysis. In a recent study, deformation kinetics and

the dependence of the impact pressure in terms of time in the cold spray process has been

simulated by the FEM code ANSYS/LS-DYNA3D for 316L stainless steel[31].
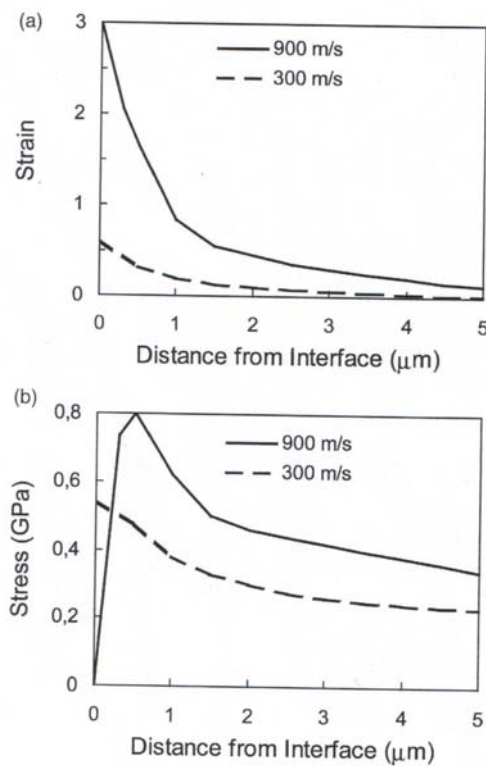
Figure **2.6**: Calculated profiles of (a) plastic strain and (b) flow stress

A strain-rate-dependent and temperature-dependent material model modified according to

the Zerilli-Armstrong model[91] was used for both the particle and the substrate material.

The authors of this paper further assumed adiabatic deformation; modeling was not a

coupled thermal/mechanical analysis. They concluded that in most materials, the process

leads to high plastic deformation as the dynamic yield strength is exceeded and elastic deformation can be neglected in a first approximation.

2.6 Self-Lubricating Coatings

2.6.1 Background

As mentioned earlier, titanium alloys have poor frictional and wear characteristics[100]. Therefore, the use of uncoated titanium alloys is restricted to non-tribological applications. To realize the full benefit of titanium alloys in friction and wear applications, surface modifications or treatments are required to effectively increase near surface strength, thereby reducing the coefficient of friction and lowering the tendency for material transfer and adhesive wear.

Unfortunately, titanium alloys are not effectively lubricated by conventional liquid lubricants, greases, or solid lubricants. Extensive containment measures are required to prevent the migration and contamination of critical surfaces in the case of liquid and grease lubrication[101]. Also, the tribological characteristics of liquid lubricants are dependent on surface speed, load, and temperature. Plasma-sprayed Cu-Ni-In coatings have been used to prevent fretting of the Ti-6Al-4V alloy dovetails in gas turbine engines[102]. But delamination was observed at the exposed surfaces because of the defects in the coating and surface embrittlement due to oxidation.

Therefore, coatings for Ti-6Al-4V should be dense, have good adhesion, oxidation resistance, and a low coefficient of friction. Furthermore, the coatings should consist of a hard primary phase to provide wear resistance and load-bearing capability and a lubricating secondary phase to reduce friction between the two contacting components if wear debris form[102].

2.6.2 Diamond-like Coatings (DLC)

Diamond-like coatings (DLC) and molybdenum disulfide (MoS_2) films partly satisfy the above requirements. Diamond is naturally very hard and its friction is determined primarily by the elastic deformation of the contact region. It has a very low coefficient of friction. On the other hand, MoS_2 has a lamellar crystal structure which consists of a layer of molybdenum atoms arranged in a hexagonal array with each molybdenum atom surrounded at equal distance by six sulfur atoms placed at the corners of a triangular prism[103]. The attraction between the layers is weak, so interfacial shear strength is low, giving a low coefficient of friction. However, the bonds between Mo and S atoms are covalent and strong, providing excellent load capacity. DLC coatings on Ti-6Al-4V have been studied by various groups, with and without surface treatments. Surface treatments like- ion implantation, nitrogen diffusion, etc. have been tried to improve the adhesion between the DLC film and the substrate[104-106]. In another study, DLC coatings were deposited using a planar-coil r.f. ICPECVD system, without any surface treatment[1]. DLC coatings are starting to find application in some mechanical component applications, but their application is quite low considering the

length of time that has elapsed since the first DLC coatings were reported[107]. The very

hard DLC coatings tend to be brittle, have poor adhesion, and are unsuitable for highly

loaded applications.

2.6.3 Molybdenum disulphide (MoS_2) based coatings

MoS_2 is very effective as a solid lubricant and it has been studied as a lubricating

coating on Ti-6Al-4V[3, 108, 109]. According to the crystal structure of MoS_2 as

discussed in the section above, the weak bonding between the MoS_2 layers results in low

shear strength, and hence low friction in the sliding direction. This implies that the basal

plane of the crystals in polycrystalline films lies parallel to the sliding direction for good

lubrication. Earlier studies have concluded that rubbing produces the parallel orientation

in the MoS_2 coating[110, 111]. Two parameters related to the crystal structure of MoS_2

are thought to be of particular importance for solid lubrication: the adhesion of the film to

the substrate surface, and the crystallographic orientation of the platelets in the film[112].

In previous studies, ion implantation and bond layers were necessary to modify

the Ti-6Al-4V substrate prior to MoS_2 sputtered coating in order to increase the adhesion

strength and increase the endurance lifetime[3]. Multi-layer coatings and various kinds of

pretreatments complicate coating procedures, increase costs, and invite process

variability. Mechanical polishing to remove nascent oxides and improve surface finish of

titanium alloy parts is time consuming[108, 109]. In order to overcome these difficulties,

various studies have been done in the development of MoS_2/Ti composite coatings[1,

113-116]. In these coatings MoS_2 provides the lubrication. The existence of Ti in the

coating is thought to improve the adhesion of the film to the substrate. These coatings have been deposited by different sputtering processes and have a range of applications such as bearings, punches, dies, hobs, cutters. The presence of oxygen in the sputtering chamber has a major effect on the crystalline orientation, morphology, friction coefficient, and wear life of MoS_2 films. Results have shown that very pure thin films of MoS_2 grown under ultra-high vacuum conditions have yielded friction coefficients approximately one order of magnitude smaller than those obtained with conventional high-vacuum films[110, 117, 118]. Most of these coatings were suitable only in vacuum and at 0% humidity. Addition of various metals such as Au[119], Ni[119, 120], Pb[121], Ti[116, 121, 122], Ta[119], Cr[123], mixed metal[124], and ceramics, such as TiN or TiB_2[122, 125]. Most of the studies were still performed using RF sputtering processes.

2.6.4 Hexagonal Boron Nitride (hBN) - a potential solid lubricant

Hexagonal Boron nitride (hBN) is a binary chemical compound, consisting of equal amount of boron and nitrogen. Structurally, it is isoelectronic to carbon and takes on similar physical forms: hexagonal boron nitride (h-BN) and cubic boron nitride (c-BN). Most of the research has been done in h-BN as a solid lubricant additive except one which mentions c-BN with better lubricating properties[126]. These unexpected results were observed because of premature debonding of h-BN during sliding and the subsequent discharge of their flakes out of the nip between the substrate and the ball indenter, owing to their lower adhesion to the substrate.

Hexagonal boron nitride (h-BN) has a lamellar crystalline structure in which the bonding between molecules within each layer is covalent, while binding between layers is almost entirely by means of weak van der Waals forces. This structure is similar to MoS_2 and graphite. In many instances, h-BN exceeds performance levels of these conventional solid lubricant characteristics, particularly adherence and thermochemical stability[127]. It is stable up to about $3000^{\circ}C$ in a nitrogen environment.

The lubrication uses of h-BN include h-BN filled resin shapes in bearings, sleeves, rings, seals, and other sliding components[128]; ceramic composites containing h-BN[129]; electrodeposition of fine particles of h-BN (combined with other constituents) for self-lubricating, high-wear-resistance, metal ceramic coatings for metal substrates in engine parts[130]; and finally, plasma spray coatings for abradable seals and similar high-wear surface[131]. These applications though gave h-BN an important place in the lubrication industry, but still not enough attention was paid to study more applications. This is partly because h-BN was reported to have a high friction coefficient and was assumed as inferior to other lamellar structures, such as graphite and molybdenum disulfide (MoS_2)[128, 132]. An improvement in anti-wear performance was reported lately by integrating h-BN with TiB_2 or c-BN[133]. The lamellar nature of h-BN makes it possible to annihilate the common severe compressive stress, decrease friction, and as a result of property tailoring, improve the overall tribological performance.

2.7 Composite Coatings

The development of composite coatings by various thermal spray processes has been carried out since the 1980's, when WC-Co was thermally sprayed for wear resistance applications[134-136]. The WC-Co powder experiences a combination of decarburization, oxidation, and reduction by reaction with the hydrogen, and dissolution/reaction between the WC and Co during thermal spray. This results in formation of phases, such as, W_2C, W, $Co_xW_yC_z$ and WO_3, which are hard and brittle in nature[137]. Cold spray presents an advantage here, as there is minimal particle melting and no phase transformation. Therefore, decarburization, oxidation and any decomposition in general are avoided in the cold spray process. Recent studies in cold spray deposition of WC-Co show that there is no detrimental phase transformation and/or decarburization of WC[38, 54, 55, 138]. It is also possible to deposit nano-structured WC-Co coatings with low porosity and very high hardness by cold spray deposition. Cold spray has also been used to deposit tungsten/copper composite powder for electronic package applications[139]. No copper oxidation was observed in the cold-sprayed deposit. The low temperature characteristic of the cold spray process has made it possible to deposit temperature sensitive composite materials, such as Fe-Si without any significant change in the microstructure of the feedstock[140]. TiO_2-Zn composite coatings have been produced by spraying Zn-Fe composite powder and anatase TiO_2 nanopowder[141]. The Zn-Fe composite powder used had a hard core of Fe surrounded by a layer of Zn.

In most works regarding cold spray, ductile materials are sprayed on relatively soft, deformable substrates. Cold spray coatings of brittle ceramic materials have not been successful so far due to the absence of flattening and or mechanical bonding among particles and substrate. However, cold spray processing of hard materials such as SiC and Al_2O_3 has been successfully performed by incorporation of soft materials (Al)[142]. In these composite coatings, Al acts as a binder, and is mixed with the ceramic (Al_2O_3, SiC) in various proportions in order to successfully spray[143]. In recent work, composite coatings of Zn + Al, Zn + Al + Si and Zn + (Al-Si) were developed and characterized for surface morphology and microstructure[144].

Chapter 3

Experimental Procedures

The general aim of this research was to investigate cold spray process for developing self-lubricating coatings on the titanium alloy, Ti-6Al-4V. The candidate powders- nickel (Ni), molybdenum disulfide (MoS_2), hexagonal boron nitride (hBN), and nickel coated boron nitride were characterized on the basis of size, density, and internal microstructure. The powders with favorable characteristics were mixed in appropriate proportions and cold sprayed on Ti-6Al-4V substrate. The coatings were evaluated on the basis of microstructure, percentage of lubricant, and adhesive strength. This chapter will report on each type of test performed in terms of equipment description, operating principles, calibration, and test procedures.

3.1 Powder Characterization

For this research, three different nickel powders and two of each boron nitride, molybdenum disulphide, and nickel coated boron nitride were used. Table **3.1** gives the characteristics of the powders provided by the manufacturer.

3.1.1 Particle size distribution

The particle size and its distribution was determined using a laser scattering analyzer (model: LA-920; supplier: Horiba Instruments Incorporated, Irvine, CA). This equipment measures the scattered light intensity by particles in the moving fluid and calculates the particle size using photo diode detectors.

Table **3.1**: Candidate powders

Powder	D_{50} (µm)	Vendor
Nickel, Ni-12	12	Novamet
Nickel, Ni-30	30	Praxair Surface Technologies
Nickel, Ni-75	75	Atlantic Equipment Engineers
MoS_2, MS-1	3	Atlantic Equipment Engineers
MoS_2, MS-30	30	Rosemill Co.
hBN	3	FJ Broadmann and Company
Ni coated hBN (90 wt% Ni), Ni Coat hBN-90	75	Federal Technology Group
Ni coated hBN (80 wt% Ni), Ni Coat hBN-80	103	Federal Technologies Group

According to the Mie-theory, the intensity with which light scatters at an angle is inversely proportional to the particle size. Larger particles (> 3µm) scatter light forward,

in the direction of the light's original path. This forward scattered light is focused through a condenser lens, resulting in the pattern of concentric rings often described as Fraunhofer dispersion. Smaller particles scatter light to the sides, and back toward the light source. A ring-shaped array of photo diodes measures forward scattered light, side and rear detectors sense light dispersed at higher angles.

This equipment is checked monthly for drift in results by measuring two reference sets of powder: an iron carbonyl powder with a median diameter of 4μm and a larger stainless steel powder, median diameter of 97μm. These periodic readings must be within 2% of the baseline values to verify calibration.

For this testing, approximately one gram of each powder was mixed with 2 ml of isopropyl alcohol (IPA) and one drop of soap to create a suspension fluid. Several drops of this fluid were then added to approximately 200 ml of IPA circulating through the system. Three measurements were taken for each powder with and without using an in-system ultrasonic horn, used to reduce the agglomeration.

3.1.2 Pycnometer density

The pycnometer density gives the theoretical density of loose powder and is the measure of internal porosity. This density was measured using a pycnometer (model: Accupyc 1330; supplier: Micrometrics, Norcross, GA). The equipment has two chambers of known volume: a reference chamber (V_e) and a chamber containing the sample (V_s). There is a valve between these two chambers which is sealed. The sample chamber is pressurized to a pressure P_1 with helium, and the reference chamber is evacuated. The

valve between the chambers is then opened, and a second pressure (P_2) is measured. Applying ideal gas law, the only unknown, volume of powder (V_p) may be derived as Equation **3.1**.

$$P_1 (V_s - V_p) = P_2 (V_s - V_p + V_e) \qquad (3.1)$$

The mass of the powder divided by the volume yields the pycnometer density. This density is then compared with the theoretical density of the material. Calibration of the pycnometer is verified monthly using reference spheres. The spheres are of known volume, and measured values must fall within +/-0.05% to validate the system calibration.

For this test, the powder was again weighed using Mettler AE 200 balance with a measurement precision of 10^{-4} g. Three measurements of each powder were made.

3.1.3 Scanning electron microscope observation

Micrographs of as-received powder were taken using scanning electron microscope (model: XL30 ESEM; supplier: Philips). This equipment can work in two modes, secondary and backscatter. The secondary electron mode is normally used for general viewing; it has higher resolution and can go to higher magnifications than backscatter. Backscatter emphasizes the difference between elements of different atomic masses.

For this research, inspections were made in both secondary and backscatter electron mode. These micrographs are a qualitative measure of particle size, size distribution, and shape of the powder particles.

3.1.4 Micro-hardness measurement

Micro-hardness was measured using a hardness tester (supplier: Leco Corp., St. Joseph, MI). The powders were mounted in epoxy and polished on the Rotopol, auto-polisher. Hardness measurements were conducted by using a vickers diamond pyramid indenter. A load of 10 g was applied for a dwelling time of 10 seconds during the measurement of micro-hardness. A Leco video line micrometer VL-101 was used for measuring the length of the indentation on diagonals. The Vickers hardness number was calculated based on Equation **3.2,** where *HV* is the Vickers hardness number, *P* is the force in grams, and *d* is the mean of the two diagonals in micrometers, by dividing the applied load in kilograms force by the measured projecting area of the resulting indentation.

$$HV = \frac{1854.4P}{d^2}$$

(**3.2**)

The projected area from the indentation was computed from the mean of the measured diagonals of indentation.

3.2 Mixing and Drying

Mixing the powders played an important role in this research. The appropriate amounts of powders were weighed using a balance (model: PJ6000; supplier: Mettler-Toledo, Inc., Columbus, OH). The weighed powders were dry-mixed in a turbula mixer (model: Type2C; supplier: Bachofen AG, Switzerland) for 2 hours.

The mixed powders were baked in conventional oven (model: 70DM, supplier: Precision Scientific) for 12 hours at 100°C. Baking was done in order to remove any moisture in the powder mixture before cold spray.

3.3 Cold Spray

The process (see schematic in Figure 3.1) is named "cold spray" because of the relatively low temperatures (0 to 700°C) of the expanded gas and particle stream that emanates from the nozzle. The cold spray equipment installed at Kuchera Defense Systems, Johnstown, PA was used for the experiments. The basic equipment (supplier: Ktech Corp., Albuquerque, NM) consists of pre-chamber and nozzle; powder feeder and balance scale; gas heater; gas control module; and computer control and data acquisition.
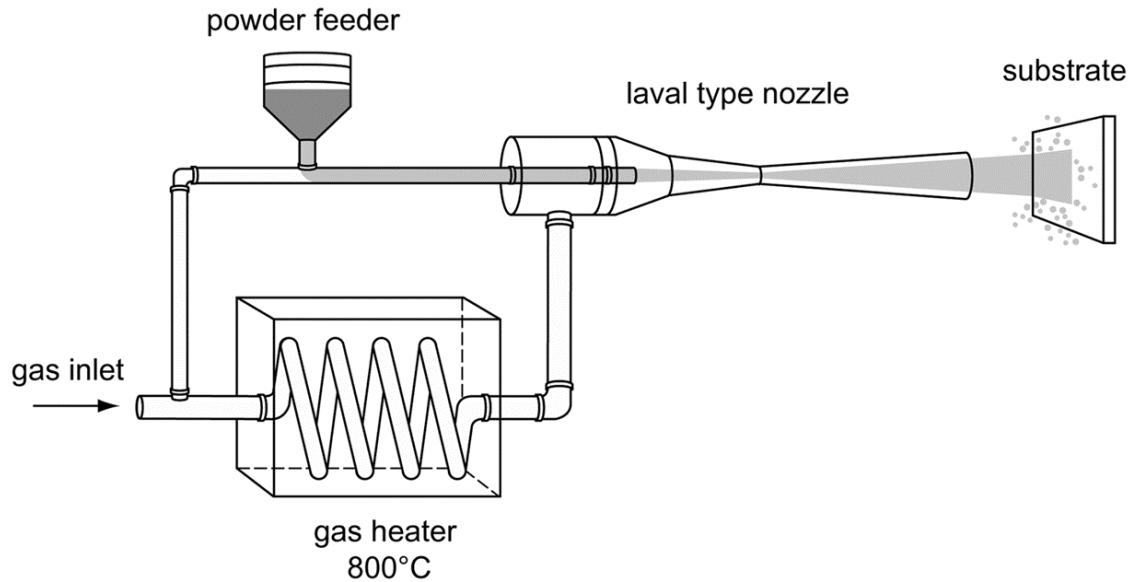
Figure **3.1**: Schematic of Cold Spray Process

3.3.1 Nozzle and pre-chamber

The Ktech cold spray system uses a lightweight pre-chamber/nozzle gun

configuration with a supersonic nozzle for spraying through either rectangular or circular

exit geometry. The connection of the nozzle to the pre-chamber is by a conical flange,

using a single large nut. The rectangular nozzle is fitted with alignment pins so that the

nozzle fits on the pre-chamber with the length of the aperture facing vertically or

horizontally. The throat diameter of the nozzle was 2 mm . The nozzle was made of

tungsten carbide. Ktech has optimized the construction of the flow from the nozzle

aperture to maximize the velocity of the powder at the exit aperture. The effective spray pattern was achieved by positioning the nozzle aperture approximately 25 mm from the target.

The purpose of the pre-chamber is to mix the powder with a gas for acceleration into and through the supersonic nozzle. The pre-chamber contains the inputs for cold spray mixing as well as ports for monitoring the temperature and pressure with in the chamber. By measuring temperature and pressure inputs, it is possible to calculate the flow rate of the output from the nozzle. Powder is fed to the top of the pre-chamber by a stainless steel tube. The powder enters the pre-chamber and is mixed with the acceleration gas at the nozzle aperture entrance. The temperature is measured at the chamber for feedback to the gas control module for regulation of temperature and flow rate. The pressure and temperature combination gives a particular flow rate. The software makes automatic adjustments in flow rate for different main (propulsion) and carrier (powder feed) gases. The pre-chamber is where the gas-fed powder and accelerating gas are mixed. Carrier gas feeds the powder from the hopper and via high pressure flexible braided stainless steel transport lines to the top of the mixing chamber through a 1/8" stainless steel tube. A ½" high-pressure flexible braided stainless steel line is used to transport the main gas into the mixing chamber.

3.3.2 Gas heater

The gas heater is mounted on a robot arm and connected to the pre-chamber/nozzle assembly via high-temperature flex braided stainless steel hose. The

heater is of a bolted clamshell design and heats the main gas to operating temperature. It operates a 40 KW heating coil element constructed of RA330 stainless steel powered by a 480 V, 3 Phase 63 Amp electrical current. Current is supplied to the heating coils via #000 cables routed from the electric power supply and is controlled by software in the data acquisition and control system.

3.3.3 Powder feeder and balance scale

The high-pressure powder feeder and balance scale (model: 1264HPHV, supplier: Praxair Surface Technologies, Concord, NH) was used in conjunction with the above parts of cold spray system. The powder feeder canisters are ASME-certified pressure vessel capable feeding powder processes requiring up to 500 psi (3450 kPa) back pressure. The feeder operates on volumetric feed principle. Slots or holes in rotating powder wheels at the canisters' bases fill the powder and the wheels' rotation transfers powder to exit ports. Varying powder wheel speed controls the feed rate. Inert gas transports the powder through a hose to the process. This proven technology ensures consistent, pulse-free feeding for a wide variety of materials and particle sizes over a wide range of features.

3.3.4 Computer control and data acquisition

Experimental control consisted of a 2.2-GHz Pentium processor, 17-inch flat screen monitor, control and communication hardware, Labview source code, and required programming for controlling the powder hopper, gas heater, gas control module, and data logging. The processor is housed in a NEMA 12 enclosure for use in industrial environments.

3.3.5 Robot

To automate the process and achieve consistency in the spray pattern, automation for handling the cold spray nozzle was facilitated by a robot (model: IRB 2400; supplier: ABB). The movement of the robot was accurately controlled by optimizing the acceleration and retardation. The programs can be built and saved for position and movement of the nozzle. The entire heater, pre-chamber, and nozzle assembly is mounted on the robot arm for spraying the powder on the substrate. Table 3.2

Table **3.2**: Process Parameters for Cold Spray

Carrier gas	Nitrogen or Helium
Gas temperature	500°C
Gas pressure	2.4 MPa for nitrogen 3.45 MPa for helium
Spray distance	12.5 mm
Spray gun velocity	20 mm/s

3.4 Coating Characterization

The cold spray coatings were characterized based on surface morphology, microstructure, and distribution of lubricant. The coatings with the most homogeneous lubricant distribution were analyzed using X ray diffraction and micro-hardness testing. The bond strength of the coatings were measured using adhesion strength testing.

3.4.1 Microstructural analysis

Coating coupons were sectioned perpendicular to the coating surface, mounted, and polished using the standard procedures. Polished samples were in turn analyzed on the Nikon Epiphot 300 optical microscope. A Philips XL30 scanning electron

microscope set in secondary electron mode was used to obtain the micrographs for microstructural analysis. In order to reveal the lubricant distribution in the coatings, various magnification levels were used. The presence of lubricant in coatings was verified by the energy dispersive x-ray analysis.

3.4.2 Micro-hardness testing

Micro-hardness measurements were performed on mounted samples using a conventional Vickers micro-hardness tester with a 300 g load. The measurements were made at increasing distances from the interface of the coating and substrate on the coating cross section.

3.4.3 Adhesion testing

Adhesion testing was conducted as per ASTM standard C633-01 for adhesion and cohesion strength of thermal spray coatings. The test specimen comprised of an assembly of a coated substrate fixture and a loading fixture. These were cylindrical in shape (height = 3.8 cm and diameter = 2.5 cm), with coating applied at one end. A rough grinding treatment was performed on the coating so as to decrease the thickness variation across the surface to below 0.025 mm. The coating thickness was determined with a micrometer by measuring the total length of the coating fixture before the coating was applied and after the coating was ground. The clean loading fixtures were attached to the coated

substrate fixtures by using about 0.1 cc of epoxy, E-214HP HYSOL. In addition, a set of uncoated fixtures were prepared for measuring the adhesion strength of the bonding agent. The bonded fixtures were air cured for 20 minutes, after which the bonded fixtures were cured at 150°C for two hours.

The prepared samples were tested by using the Instron IX automated testing machine. An increasing load was applied to each test specimen at a constant rate of cross head travel equal to 0.013 mm/s. The degree of adhesion strength was calculated as per Equation **3.3**

$$S_t = \frac{P_{max}}{A} \tag{3.3}$$

where S_t is the adhesion or cohesion strength, P_{max} is the maximum load applied, and A is the cross-sectional area details the coatings which were tested for adhesion. Table **3.3** details the coatings which were tested for adhesion.

Table **3.3**: Coatings for Adhesion Testing

Sr. No.	Sample	As-sprayed coating thickness (mm)	Coating thickness after grinding (mm)
1	Epoxy E-214HP HYSOL	-	-
2	Ni-75	0.95	0.70
3	Ni-12 + 20wt%Ni Coat hBN-90	0.88	0.63
4	Ni-12 + 20wt%Ni Coat hBN-80	1.10	0.57
5	Ni-12 + 25wt%Ni Coat hBN-80	1.23	0.90
6	Ni-12 + 30wt%Ni Coat hBN-90	1.99	1.54
7	Ni-12 + 30wt%Ni Coat hBN-80	2.19	1.56

Chapter 4

Experimental Results

The results of the experiments described in Chapter 3 are presented in this chapter. In addition to the experimental results, this chapter details the various feedstock preparation techniques used in the current research.

4.1 Powder Characterization

4.1.1 Morphology & Internal Microstructure

The scanning electron micrographs of the as-received powders are shown in Figure 4.1-4.3. Nickel powder is formed by a carbonyl decomposition process and is spherical and spiky in shape. Lubricant powders are primarily manufactured by the milling process and have a platelet structure.
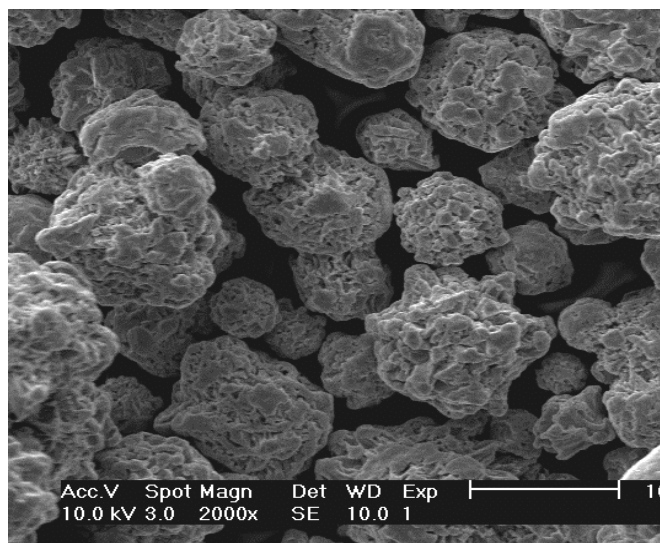
Figure **4.1**: Scanning electron micrograph of as-received nickel
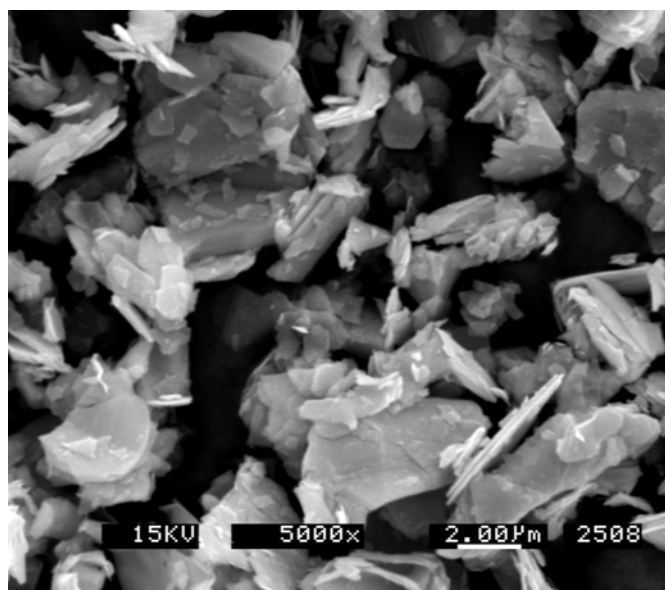
Figure **4.2**: Scanning electron micrograph of as-received molybdenum disulphide (MoS$_2$)
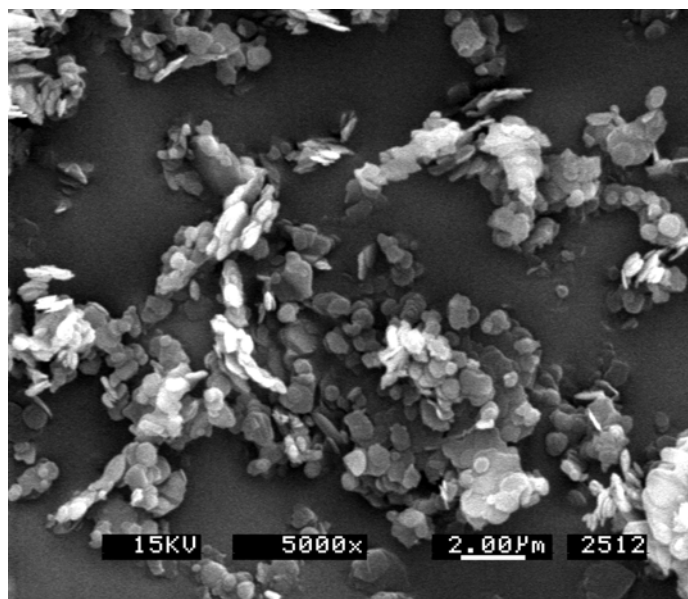
Figure **4.3**: Scanning electron micrograph of as-received hexagonal boron nitride (hBN)

Figure **4.4** show the micrographs of the as-received Ni coated hBN powder. As shown by

the figure, the powders are irregular in shape.
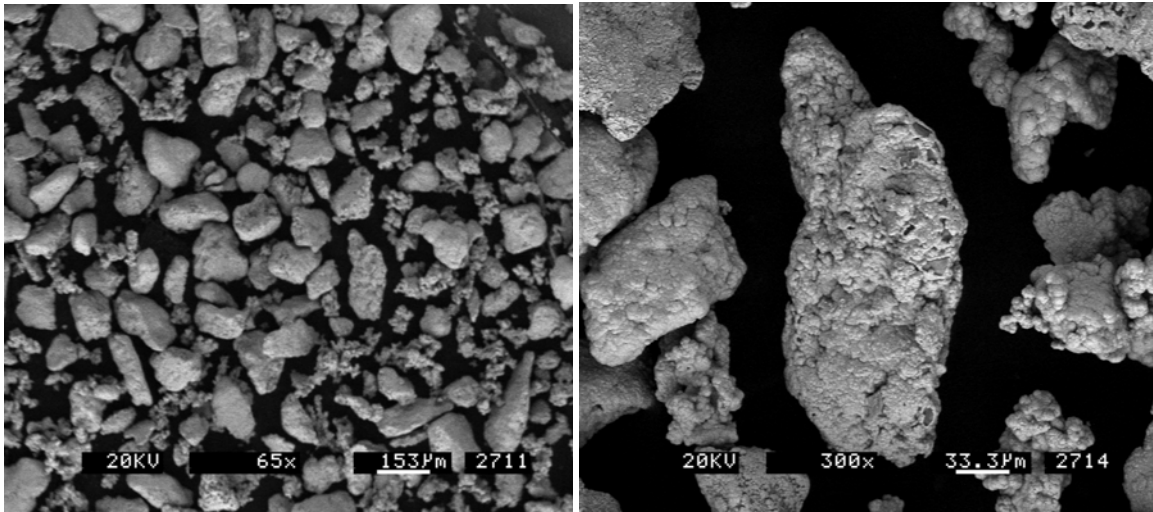
Figure **4.4**: Scanning electron micrographs of as-received Ni coated hBN powder

The internal microstructure of the Ni coated hBN was observed under an optical microscope. Initially, the powder sample was mounted in epoxy and polished to reveal the internal microstructure as seen in Figure **4.5**. The internal microstructure reveals three phases in a single coated particle. The interior consists hBN that is covered by a thin
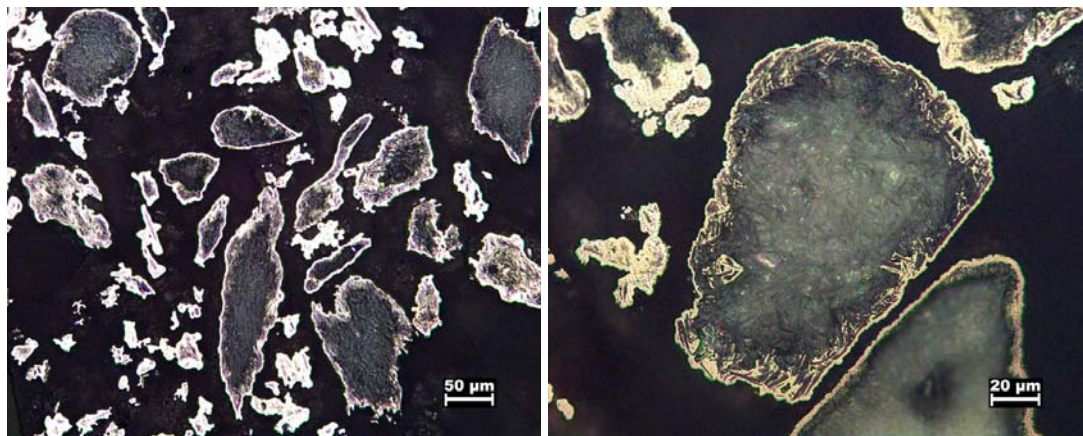

Figure **4.5**: Optical image of internal microstructure of Ni coated hBN

layer of Ni coating. However, in most of the particles, there is an intermediate layer between Ni and hBN, which has a lamellar structure.

4.1.2 Pycnometer Density

The pycnometer density measured on a pycnometer for as-received powders is given in Table 4.1

Table **4.1**: Pycnometer density of as-received powders

Powder	Pycnometer density (g/cm³)	Standard deviation (g/cm³)
MoS_2	5.065	0.013
hBN	2.32	0.013
Ni Coat hBN-80	4.345	0.003
Ni Coat hBN-90	5.651	0.003

4.1.3 Microhardness

The cold spray process is based on the adhesion of powder particles after they undergo mechanical deformation. As such, microhardness plays an important role in determining the extent of deformation experienced by powder particles upon impact.

Therefore, microhardness measurement is important in the cold spray process. Table **4.2**

summarizes the microhardness results for pure Ni and Ni coated hBN powders. As

mentioned earlier, three different hardness regions are present in Ni coated hBN particle.

The pure hBN core has the minimum hardness, while the outer Ni coating has the

maximum hardness. The transition layer between the Ni and hBN phases has an

intermediate hardness values.

Table **4.2**: Micro-hardness results for pure-Ni and Ni coated BN powders

Powder	Powder Size (μm)	Powder Structure	Average Hardness (HV$_{10}$)
Nickel	12	Angular	176.8
Ni coated hBN	103	Pure BN core	10.76
		Bright white phase at particle boundary	316.3
		Interface with platelets structure	57.5

4.2 Feedstock Preparation

Feedstock preparation can be divided into three categories- admixed un-coated

powders, milled un-coated powders, and admixed pure Ni and Ni coated hBN. While

admixed un-coated powders are easy and economical to prepare, the milled & coated

powders provide the advantage of embedding lubricant in the nickel matrix prior to spraying.

4.2.1 Admixed un-coated powders

Table **4.3** gives the details of the feedstock prepared from the un-coated powders.

Table **4.3**: Experiments with Ad-mixed un-coated powders

Sr. No.	Mixture Composition	Size of Ni (μm)	Size of lube (μm)	Carrier Gas
1	Ni + 2wt% MoS_2	12	30	N_2
2	Ni + 3wt% MoS_2	12	30	N_2
3	Ni + 4wt% MoS_2	12	30	N_2
4	Ni + 2wt% MoS_2	12	3	N_2
5	Ni + 3wt% MoS_2	12	30	He
6	Ni + 4wt% MoS_2	12	30	He
7	Ni + 7wt% MoS_2	12	30	He
8	Ni + 7wt% MoS_2	32	30	He
9	Ni + 1wt%hBN	12	10	N_2
10	Ni + 2wt%hBN	12	10	N_2
11	Ni + 4wt%hBN	12	10	He
12	Ni + 4wt%hBN	32	10	He
13	Ni + 4wt%hBN	75	10	He
14	Ni + 5wt%hBN	12	10	He
15	Ni + 1wt%hBN	75	10	He

Figures **4.6** and **4.7** show the morphology of the admixed Ni (12 μm)+3wt%

MoS_2 (30 μm) and Ni (12 μm)+2wt%hBN (10 μm), respectively.
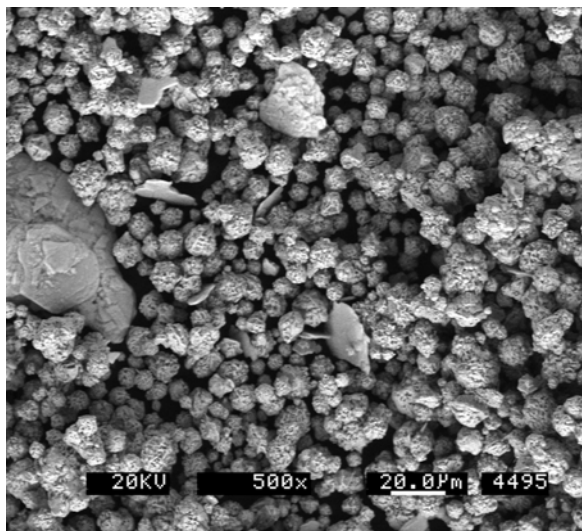
Figure **4.6**: Scanning electron micrograph of admixed Ni (12 μm)+3wt% MoS$_2$ (30 μm)
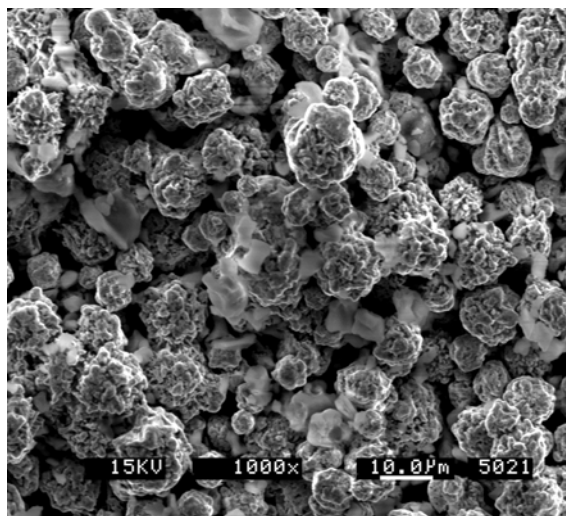
Figure **4.7**: Scanning electron micrograph of admixed Ni (12 μm)+2wt% hBN (10 μm)

The microstructures of cold sprayed admixed Ni + MoS$_2$ with nitrogen as a carrier gas is shown in Figure **4.8**. The substrate and the coating can be distinguished from each other by the interface. Figure **4.8** also show an entrapped MoS$_2$ particle in the Ni matrix. Figure **4.9** shows the energy dispersion spectrograph of the microstructure shown in Figure **4.8**.
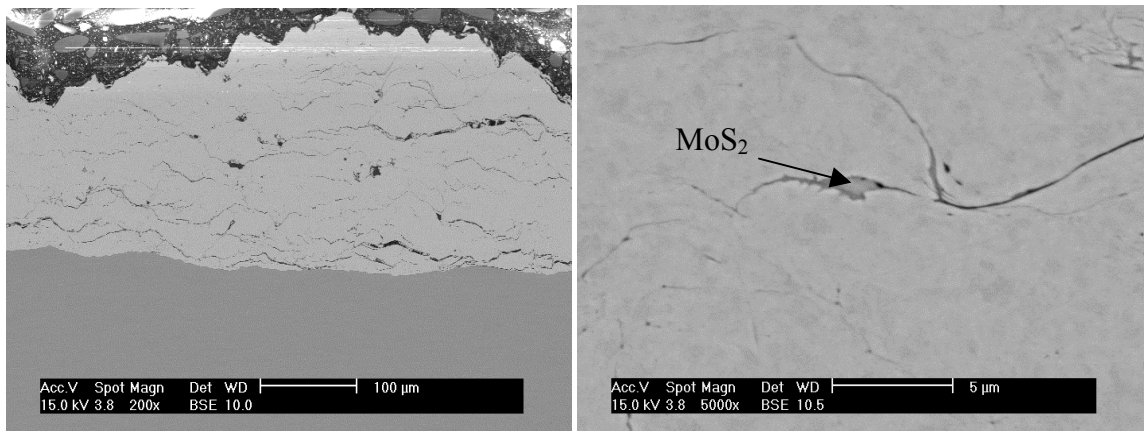
Figure **4.8**: SEM images of as-sprayed Ni+MoS$_2$ coatings using admixed powders with nitrogen
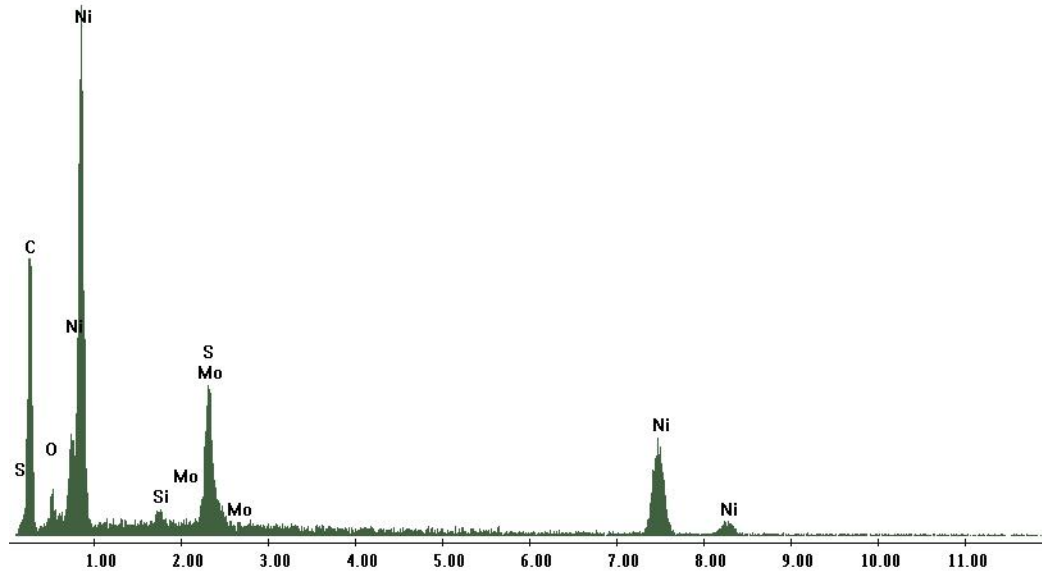
Figure **4.9**: Energy dispersive spectrograph of the SEM in Figure **4.8**

Figure **4.10** shows a comparison of the coating thickness in mils achieved by spraying admixed Ni + MoS_2 with various wt% of MoS_2. The x-axis shows the number of passes/overlaps.
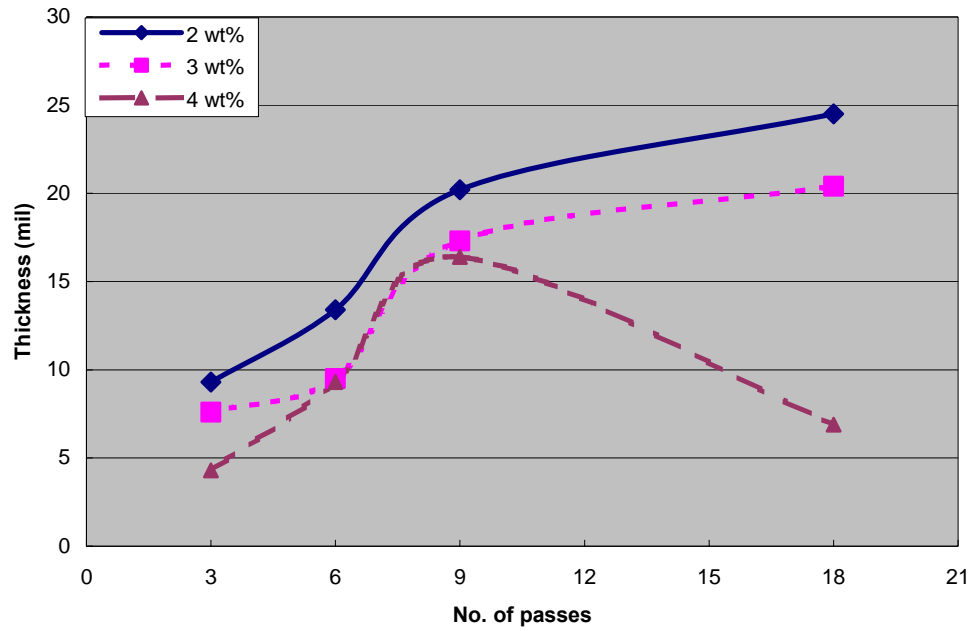
Figure **4.10**: Coating thickness versus No. of passes at different wt% of MoS_2 with nitrogen

Figure **4.11** shows an SEM image of a coating produced by admixed Ni+hBN. Based on the SEM and EDS analysis, it was determined that there was no hBN present in the coating. In addition, during the spray hBN powder was collected on the vice holding the Ti-6Al-4V substrate.
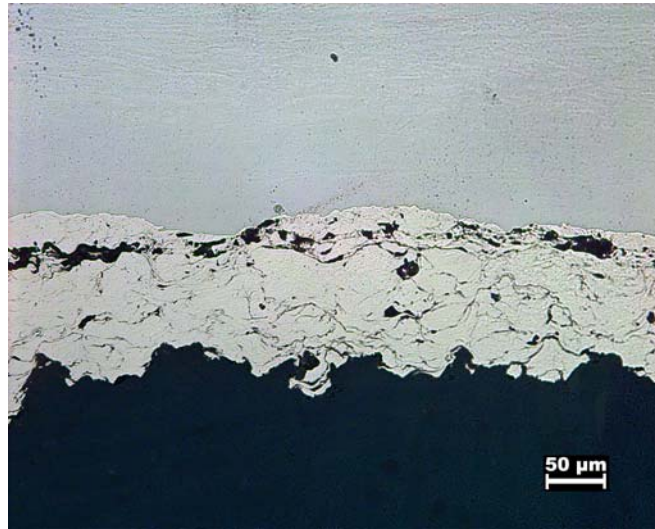
Figure **4.11**: SEM image of as-sprayed Ni-hBN coatings using admixed powders and nitrogen

As seen from Table **4.3**, using nitrogen as carrier gas, a maximum of 3 wt% MoS_2 and almost no hBN could be deposited on the Ti-6Al-4V substrate. Therefore, to increase the wt% of lubricant in the coating, helium was used as a carrier gas. Figure **4.12** show the cross-section of the un-polished coating cross-section produced from admixed Ni+MoS_2 using helium as a carrier gas. Figure **4.13** shows the polished cross-section of the same.
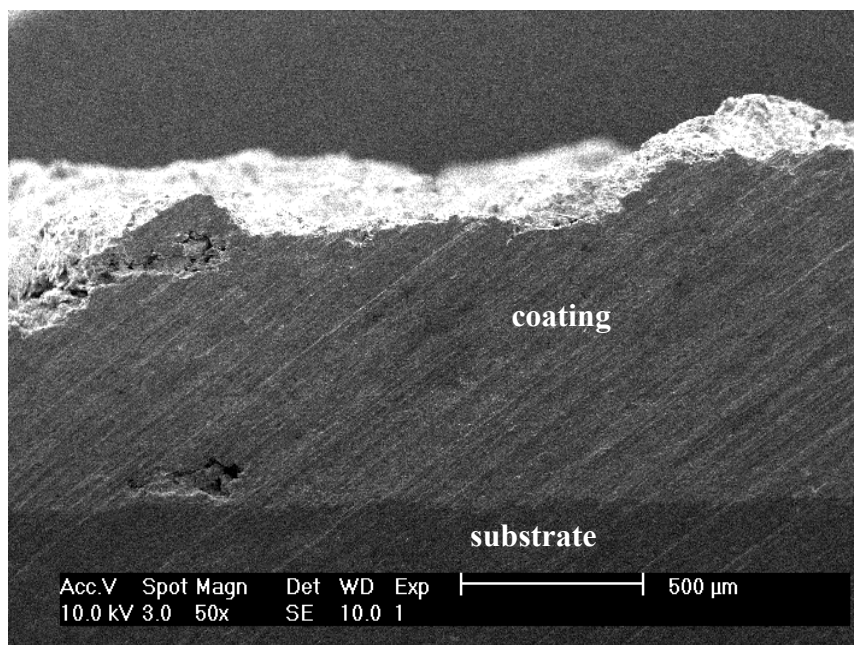
Figure **4.12**: SEM of un-polished coating cross-section of admixed Ni+MoS$_2$ using helium
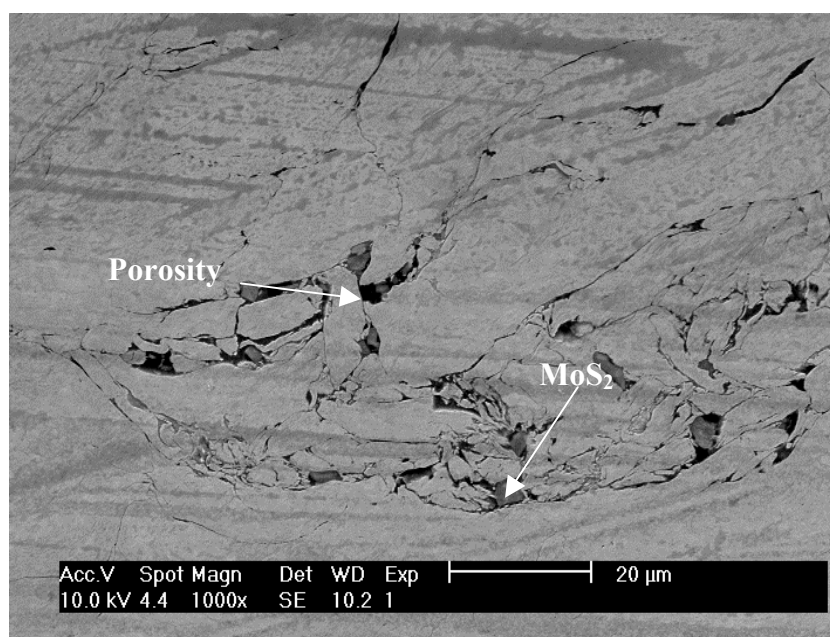
Figure **4.13**: SEM of polished coating cross-section of admixed Ni+MoS$_2$ using helium

Figure **4.14** shows the micrographs of coatings produced from admixed Ni+hBN powders using helium as a carrier gas.
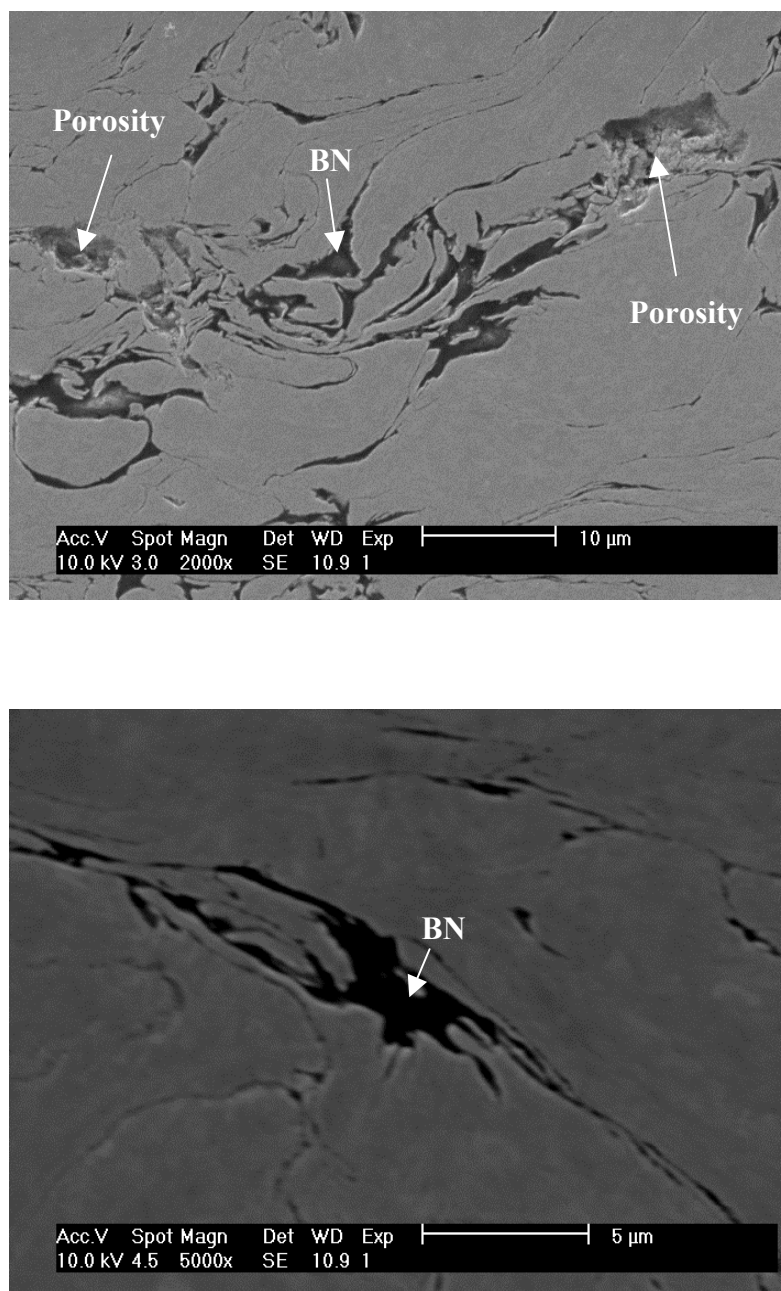
Figure **4.14**: SEM image of coating cross-section produced from admixed Ni+hBN powders using helium

4.2.2 Milled Powders

In order to produce composite powders, the admixed powders were mechanically milled at different times. Table **4.4** summarizes the details of the different feedstock powders produced by this technique.

Table **4.4**: Details of milled Ni-MoS$_2$ and Ni-hBN feedstock powders

Sr. No.	Mixture Composition	Initial Size of Ni powder (µm)	Initial Size of lubricant powder (µm)	Milling Time (hours)
1	Ni-3 wt. % MoS$_2$	12	30	.33
2	Ni-3 wt. % MoS$_2$	12	3	.33
3	Ni-3 wt. % MoS$_2$	12	3	.66
4	Ni-3 wt.% MoS$_2$	12	3	1
5	Ni-3 wt.% MoS$_2$	12	3	1.5
6	Ni-9 wt.% MoS$_2$	12	3	4
7	Ni-2 wt.% hBN	12	10	.33
8	Ni-2 wt.% hBN	12	10	.66
9	Ni-2 wt.%h BN	12	10	1
10	Ni-2 wt.% hBN	12	10	1.5
11	Ni-2 wt.% hBN	12	10	2
12	Ni-2 wt.% hBN	12	10	6
13	Ni-2 wt.% hBN	12	10	12
14	Ni-2 wt.% hBN	12	10	18
15	Ni-2 wt.% hBN	12	10	32

Figure **4.15** illustrate the morphology of the milled Ni+MoS$_2$ powders. The Ni+MoS$_2$

powders were mixed or as long as 4 hours without seeing any significant change in the

morphologies. Figure **4.16** show the morphology of the Ni+hBN powders milled for 20

minutes. Ni+hBN powders were milled for the maximum of 32 hours.
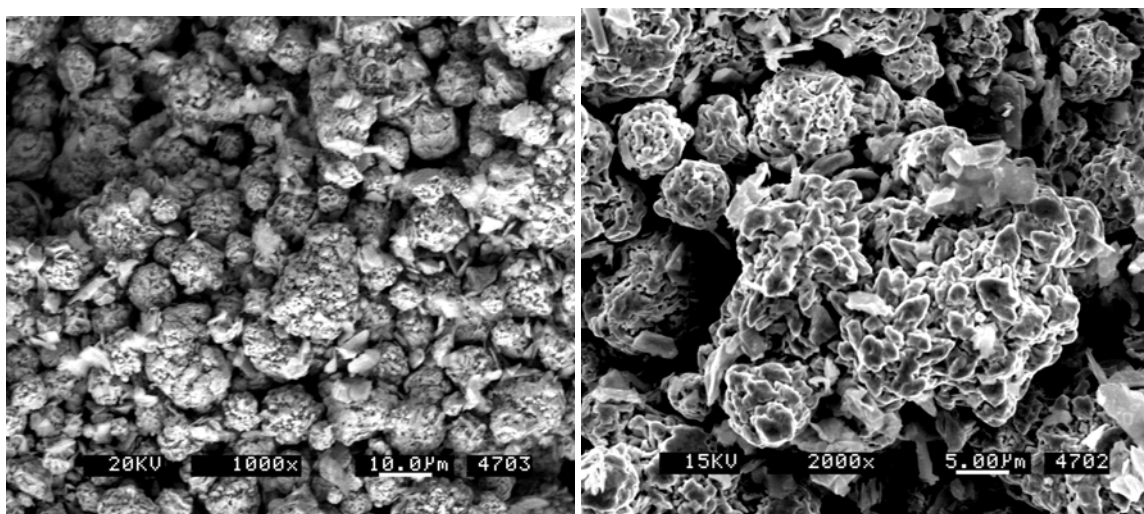
Figure **4.15**: SEM images of Ni (12 μm)+2wt%MoS$_2$ (3μm) milled for 20 minutes
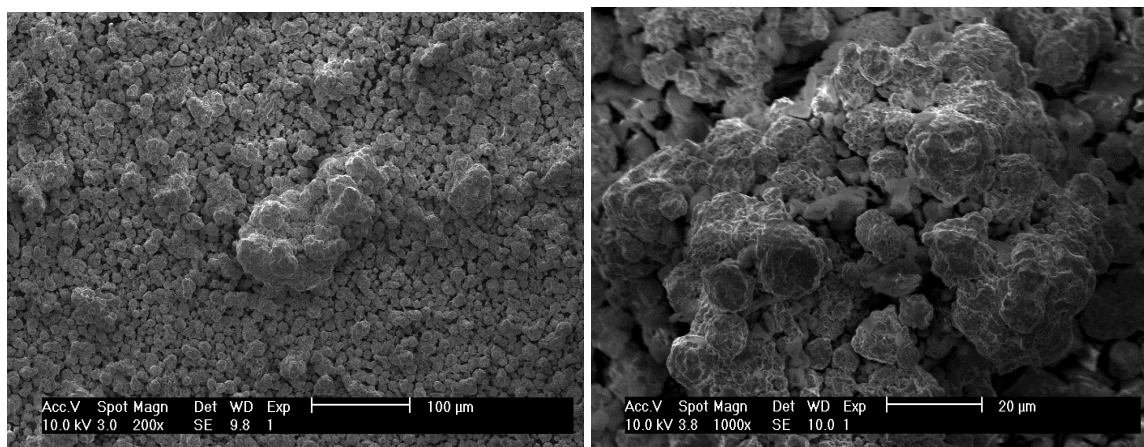
Figure **4.16**: SEM images of Ni (12 μm)+2wt%BN (10μm) milled for 20 minutes

4.2.3 Admixed Ni and Nickel Coated hBN Powders

Table **4.5** lists the composition of feedstock powders made from admixing pure Ni and Ni coated HBN powders.

Table **4.5**: Feedstocks with admixed pure Ni & Ni coated HBN powders

Sr. No.	Mixture Composition	Amount of hBN (wt.%)	Size of Ni powder (µm)	Size of lubricant powder (µm)
1	Ni-5 wt. % Ni coated hBN	0.5	12	75
2	Ni-15 wt. % Ni coated hBN	1.5	12	75
3	Ni-20 wt. % Ni coated hBN	2.0	12	75
4	Ni-30 wt. % Ni coated hBN	3.0	12	75
5	Ni-30 wt. % Ni coated hBN	3.0	75	75
6	Ni-5 wt. % Ni coated hBN	1.0	12	103
7	Ni-15 wt. % Ni coated hBN	3.0	12	103
8	Ni-20 wt. % Ni coated hBN	4.0	12	103
9	Ni-25 wt. % Ni coated hBN	5.0	12	103
10	Ni-30 wt. % Ni coated hBN	6.0	12	103

Figure **4.17** shows the coating thickness in (mm) achieved at different weight % of hBN in feedstock powders. It also shows the affect of the number of overlaps on the coating thickness. Figure **4.18** shows a SEM of the coating cross-section. To analyze and find the presence of hBN in the coatings, top surface SEM images were taken (Figure **4.19**). Figure **4.20** shows the high magnification image of coating with an energy dispersive spectrograph (Figure **4.21**).
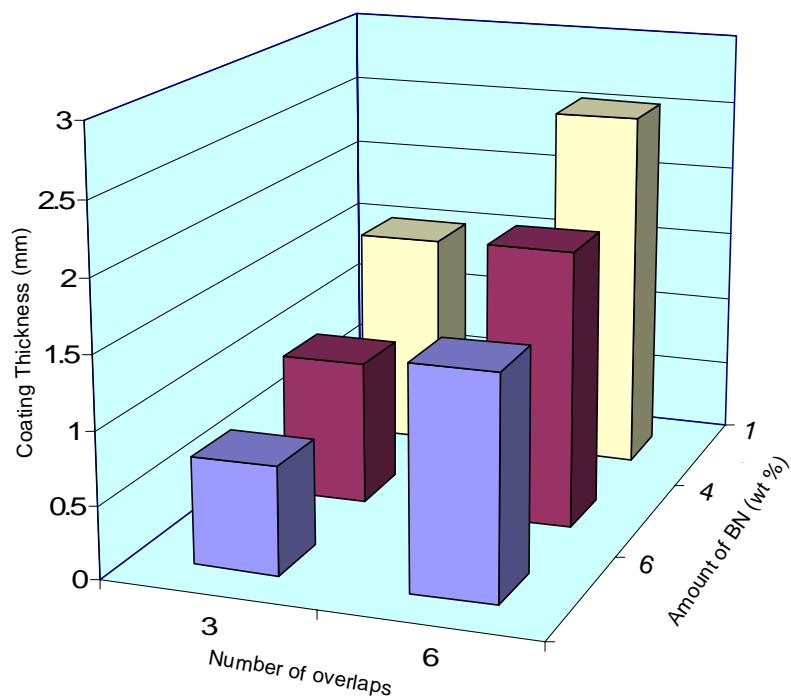
Figure **4.17**: Coating thickness (mm) at various weight % of hBN in the feedstock [145]
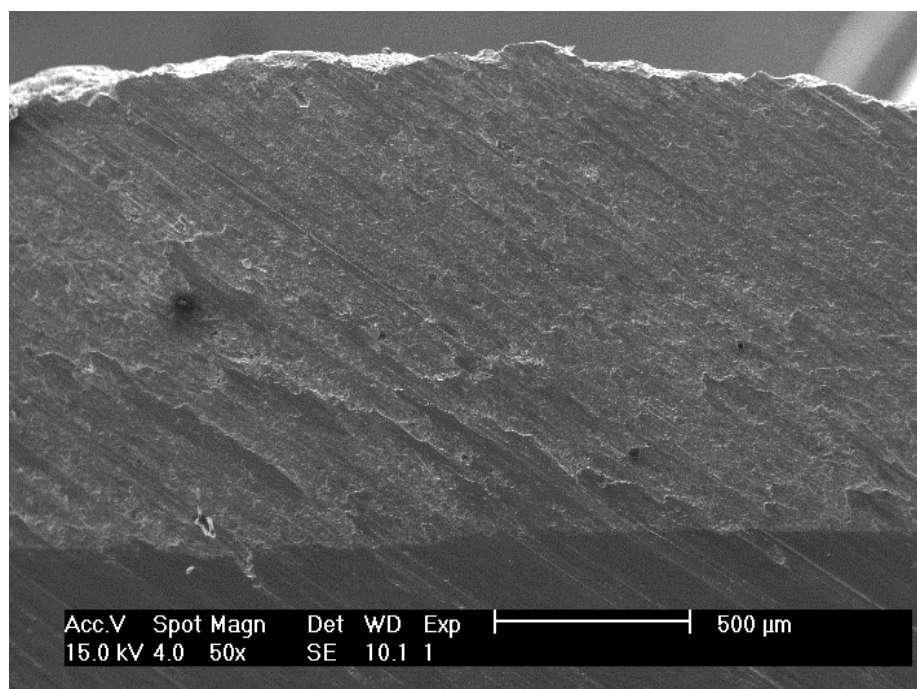
Figure **4.18**: SEM of Ni+Ni-Coat-hBN cross section
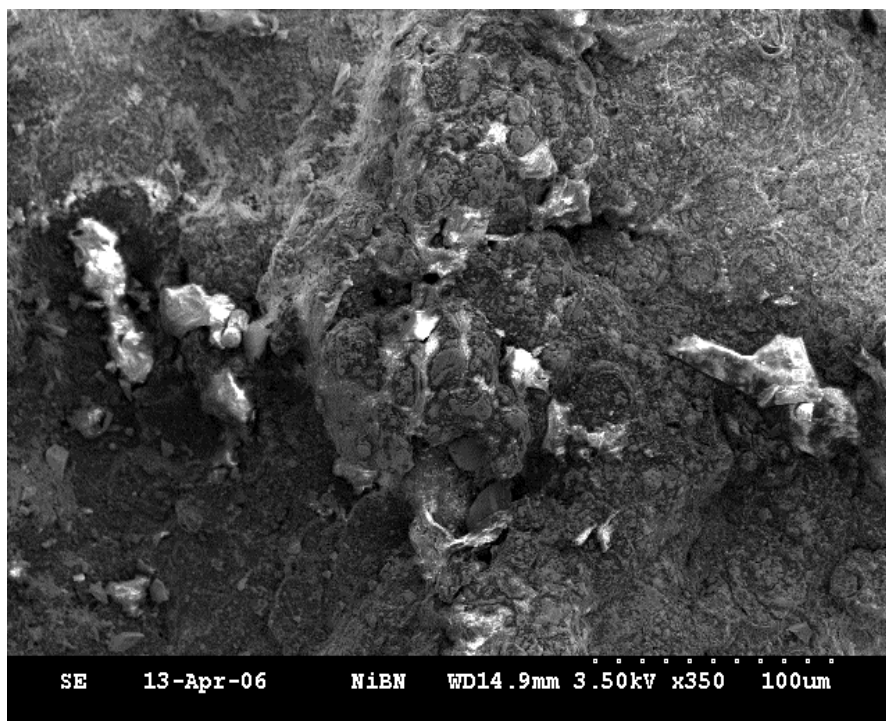
Figure **4.19**: SEM of Ni+Ni-Coat hBN coating topology
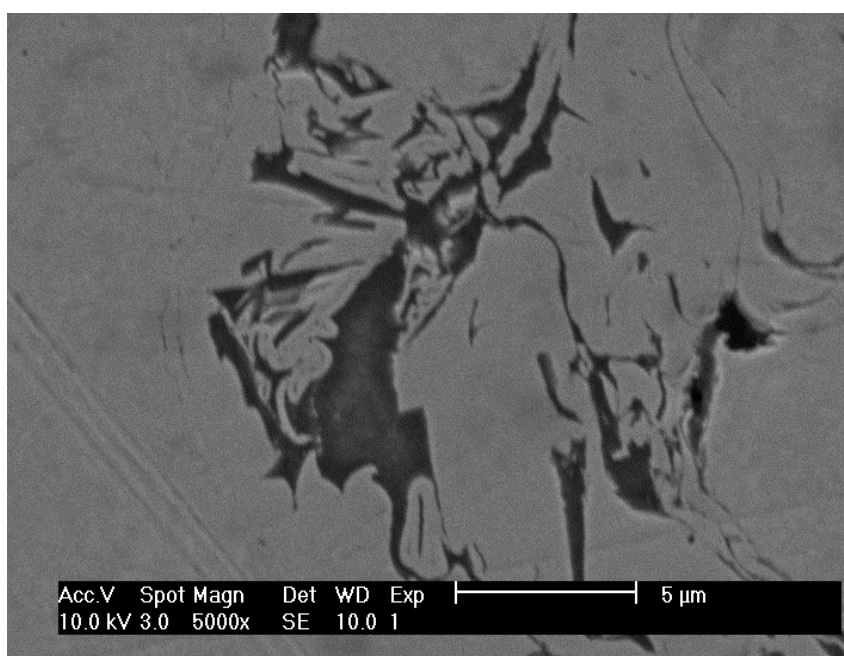
Figure **4.20**: High magnification SEM of Ni+Ni-CoathBN coating
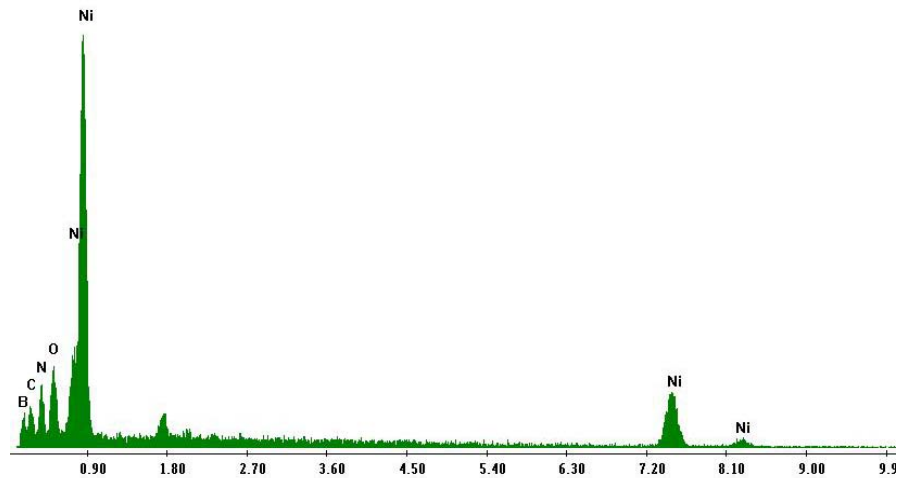
Figure **4.21**: Energy dispersive spectrograph for Ni+Ni Coat hBN coating

4.3 Mechanical Testing of Coatings

Apart from microscopy (optical + electron) coatings were tested for hardness and adhesion strength. The mechanical properties were measured on the coatings that were confirmed with the presence of lubricant.

4.3.1 Micro-hardness Testing

The Vicker's micro-hardness measurements were made at the increasing distances from the interface of the coating and substrate, as shown in Figure **4.22**. Figure **4.23** shows the hardness profile of the Ni+6wt%hBN coating and it's comparison to pure Ni coating.
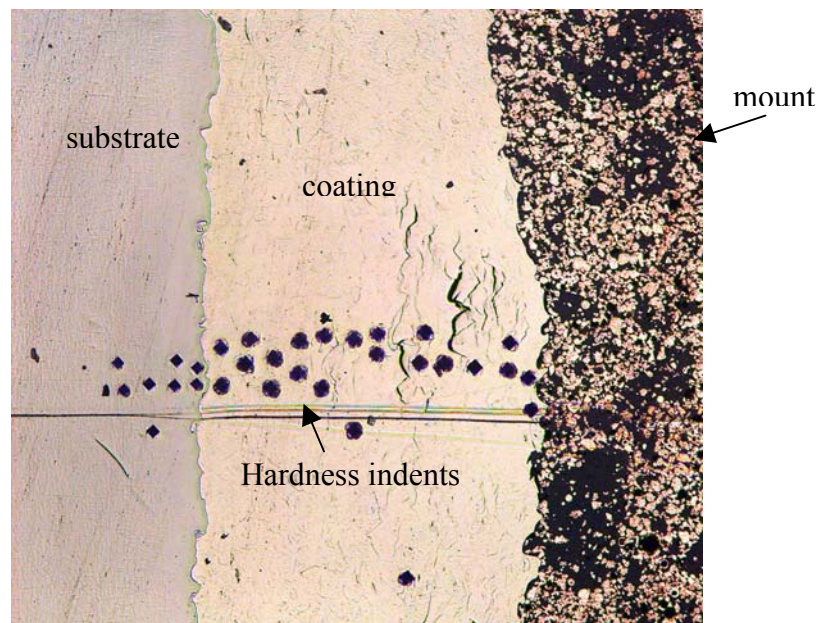
Figure **4.22**: Micro-hardness study pattern
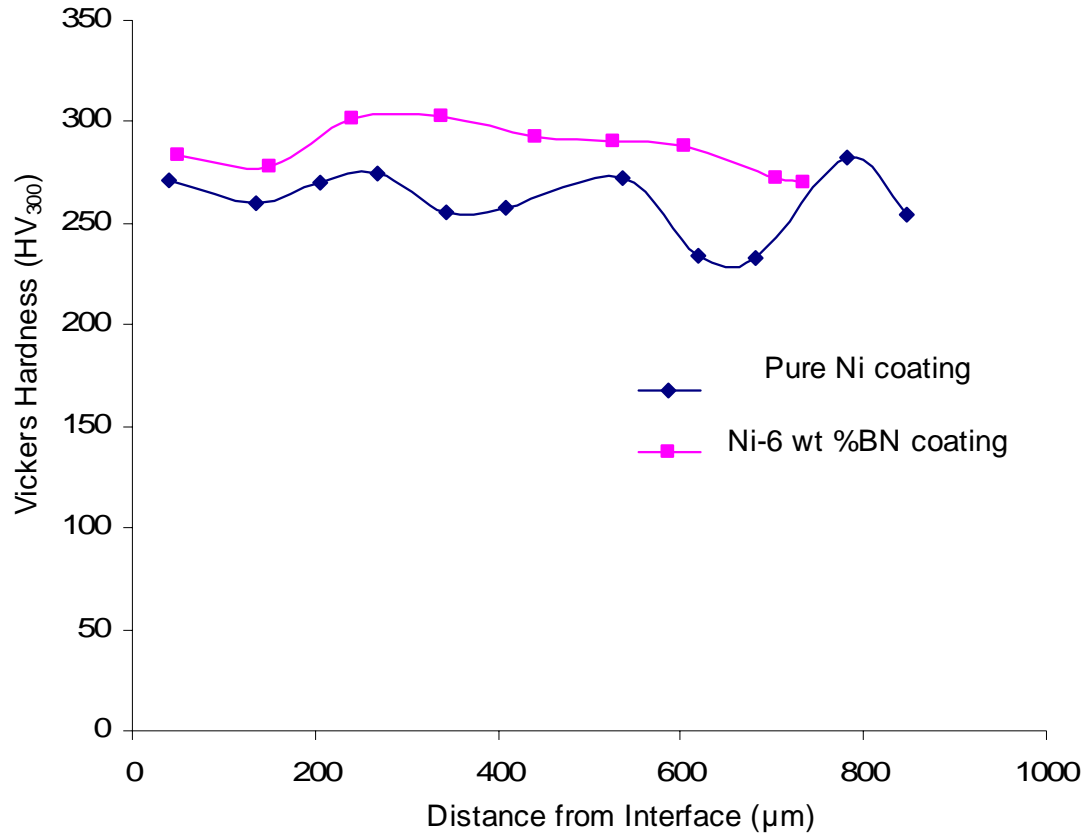
Figure **4.23**: Vickers hardness profiles for Ni+6wt%hBN and pure Ni coatings [145]

4.3.2 Adhesion Testing

As shown in Table **3.3** adhesion testing was performed on five composite coatings and pure Ni coating. The tests were performed to determine the degree of adhesion of the coatings to the Ti-6Al-4V substrate. Figure **4.24** shows the load-displacement curves of

the coatings tested under tensile load. Table **4.6** gives the bond strengths with the type of failure for various coatings.
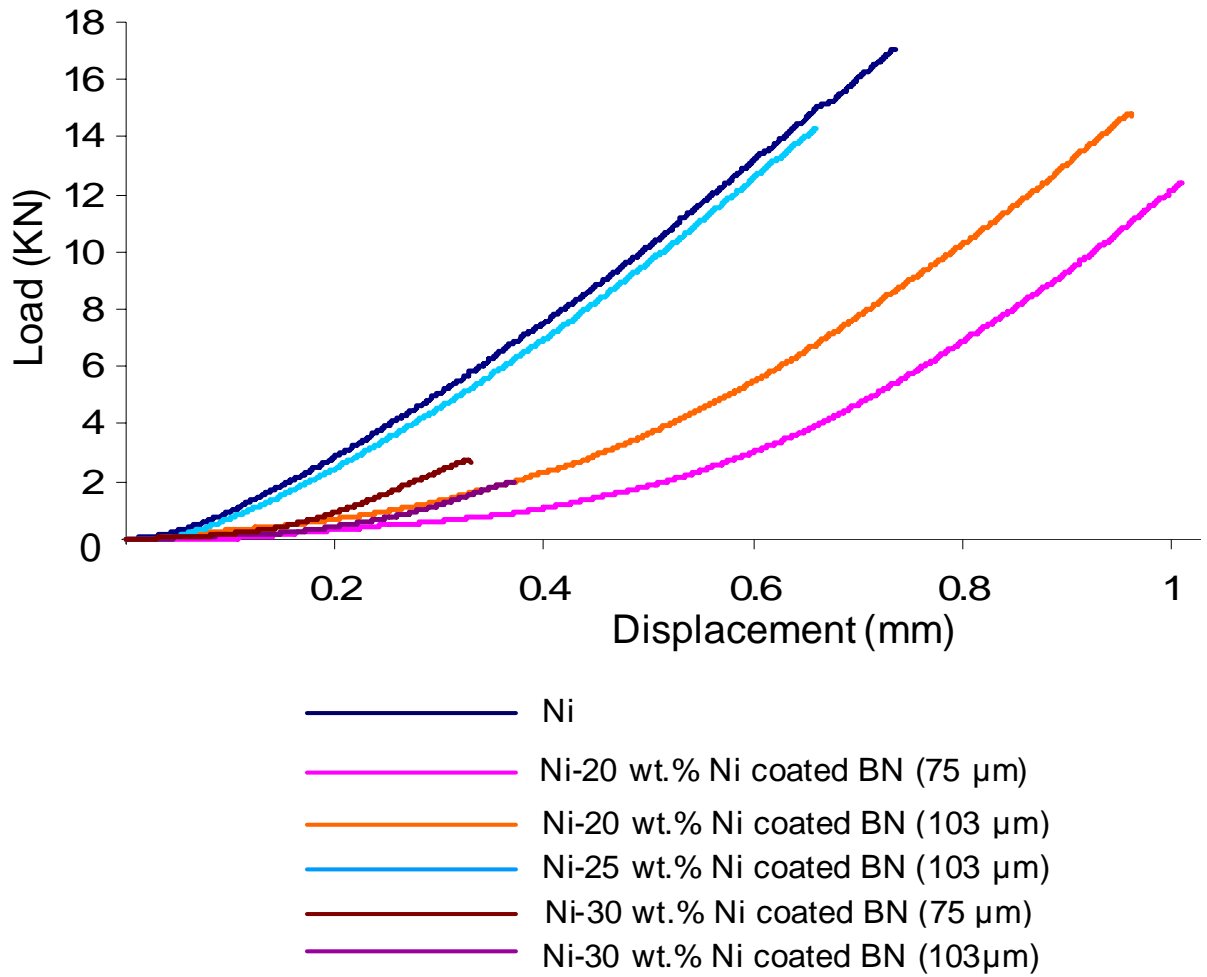
Figure **4.24**: Load-displacement curves from adhesion tests [145]

Table **4.6**: Bond strengths with type of failure after adhesion testing

Sr. No.	Mixture Composition	Size of Ni powder (μm)	Size of coated powder (μm)	Amount of hBN (wt.%)	Type of Failure	Bond Stregth (MPa)
1	Epoxy E-214HP HYSOL	--	--	--	At epoxy	53
2	Pure Ni	68	--	0	At epoxy	33.7
3	Ni–20 wt. % Ni coated hBN	12	75	2	Cohesive	25
4	Ni–20 wt. % Ni coated hBN	12	103	4	Cohesive	29
5	Ni–25 wt. % Ni coated hBN	12	103	5	Cohesive	28
6	Ni–30 wt. % Ni coated hBN	12	75	3	Adhesive	3.9
	N–30 wt. % Ni coated hBN	12	103	6	Adhesive	5.4

Chapter 5

Modeling

As mentioned previously in Chapter 2, cold spray processing techniques do not allow a precise description of each impact. Moreover, the impact velocity corresponding to individual crater is also not available. Nevertheless, the use of modeling can provide the definition of each impacting event and allow variation of any parameter to obtain trends. Given this potential, Chapter 5 discusses the development of finite-element model in ANSYS to study the particle impact in cold spray process. The chapter begins with a description of model geometry and elements, followed by an overview of the material model. The material model covers the governing equations used in bilinear kinematic hardening model and the properties of materials used. The next section describes the type of loading used during modeling and conversion of particle velocity to force experienced by an individual particle. In the latter part of the chapter, modeling cases dealt in present work are described, followed by the assumptions are restrictions used in modeling.

5.1 Model Geometry and Elements

Figure **5.1** shows the schematic of the basic model geometry and boundary conditions. The particle is modeled as a semi-circle and substrate as a rectangle, both

consisting of axisymmetric elements. The use of an axisymmetric model greatly reduces

the modeling and analysis time compared to that of an equivalent 3-D model. As seen

from the figure, the substrate is constrained in all degrees of freedom at the bottom, but

can slide in the vertical direction at the lateral edges (axisymmetric edge). The particle is

constraint on the axisymmetric edge in X-direction.
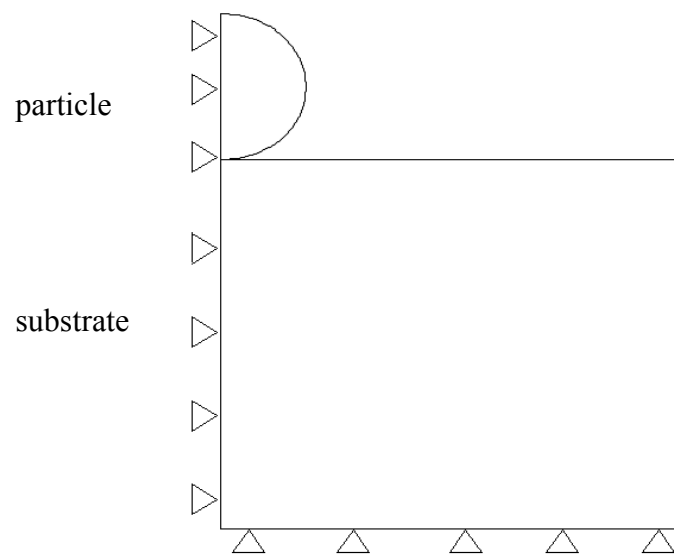
Figure **5.1**: Schematic of basic model geometry & boundary conditions

A four-noded 2-D structural solid element (PLANE182) was used to model both

particle & the substrate. This element has two degrees of freedom at each node

corresponding to translations in nodal x and y directions. The element is capable of

handling plasticity, hyperelasticity, stress stiffening, large deflection, and large strains.

The axisymmetric option was turned on by defining the element behavior (KEYOPT(3) =

1). Classical pure displacement element formulation is used which only takes

displacements or velocities as primary unknown variables. All other quantities such as

strains, stresses and state variables in the history dependent material models are derived from displacements. It is most widely used formulation and is able to handle most nonlinear deformation problems.

The interface between the particle and the substrate was modeled using contact elements. As both particle and substrate are deformable in nature, the contact problem was treated as flexible-to-flexible contact. Surface-to-surface contact elements were used to form a contact pair. TARGE169 was used as "target surface" elements on the surface of the substrate. CONTA171 was used as "contact surface" elements to model the surface of the particle. CONTA171 is a 2-D, 2-node, lower-order line element that can be located on the surfaces of 2-D solid, shell, or beam elements. Both contact and target elements were laid on the surface of 2-D structural solid elements. To reduce the initial penetration caused by numerical round-off due to mesh generation, KEYOPT(5) of CONTA171 element was set equal to two. The normal stiffness was updated at every substep based on the mean stress of the underlying 2-D PLANE182 elements from the previous substep and the allowable penetration, except in the first substep of the first load step.

To create a contact pair, the same real constants were assigned to both the target and contact elements. Figure 5.2 shows the target and contact elements used in the model to create a surface-to-surface contact.
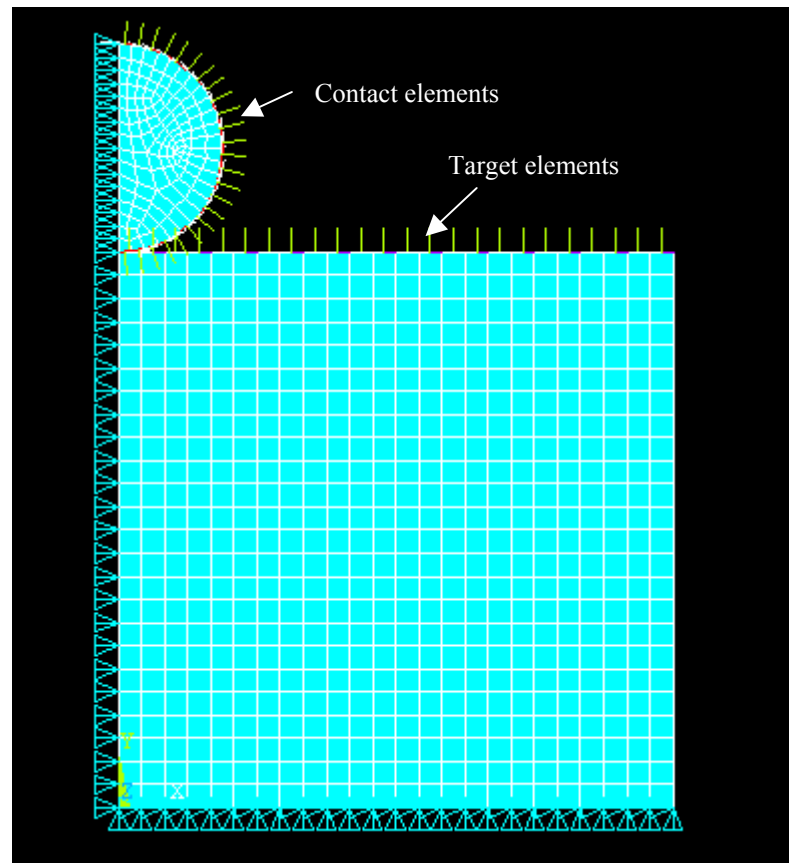
Figure **5.2**: Model geometry showing surface-to-surface contact

The surface-to-surface contact elements have several advantages over node-to-node

elements. These elements:

- Support lower and higher order elements on the contact and target

  surfaces.

- Provide better contact results needed for typical engineering purposes,

  such as normal pressure and friction stress contour plots.

- Have no restrictions on the shape of the target surface. Surface discontinuities can be physical or due to mesh discretization.

5.2 Material Model

5.2.1 Bilinear Kinematic Hardening

The bilinear kinematic hardening (BKIN) assumes that the total stress range is equal to twice the yield stress, so that the Bauschinger effect is included. The Bauschinger effect refers to the property of materials where the material's stress-strain characteristics change as a result of the microscopic stress distribution of the material. It is normally associated with conditions where the yield strength of a metal decreases when the direction of strain is changed. BKIN may be used for materials that obey von Mises yield criteria and are rate independent. The material behavior is described by a bilinear total stress-total strain curve starting at the origin and positive stress and strain value (Figure 5.3). The initial slope of the curve is taken as the elastic modulus of the material. At the specified yield stress (C1), the curve continues along the second slope defined by the tangent modulus, C2 (having the same units as the elastic modulus). The tangent modulus cannot be less than zero or greater than elastic modulus.
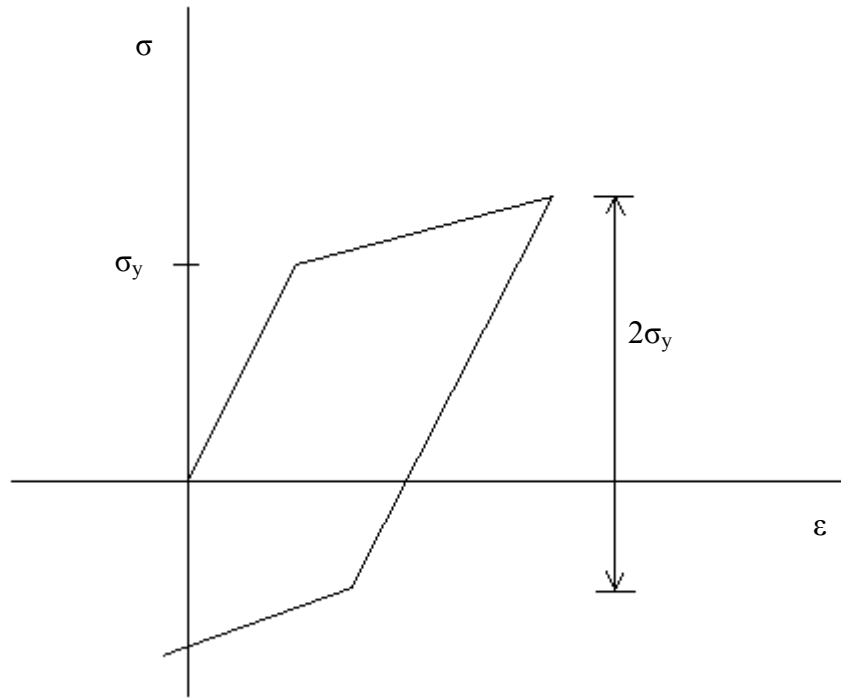
Figure **5.3**: Bilinear kinematic hardening stress-strain behavior

There are three ingredients in the rate-independent plasticity theory: the yield criteria, flow rule and the hardening rule. The bilinear kinematic hardening uses the von Mises yield criteria, the equivalent stress is therefore given by Equation **5.1**

$$\sigma_e = \left[\frac{3}{2} (\{s\} - \{\alpha\})^T [M](\{s\} - \{\alpha\}) \right]^{\frac{1}{2}} \tag{5.1}$$

where:

$\{s\}$ = *deviatoric stress vector*

$$\{s\} = \{\sigma\} - \sigma_m |1 \quad 1 \quad 1 \quad 0 \quad 0 \quad 0|^T$$

where:

$$\sigma_m = \textit{mean or hydrostatic stress} = \frac{1}{3}\sigma_x + \sigma_y + \sigma_z$$

$\{\alpha\}$ = *yield surface translation vector given by* Equation **5.2**

$$\{\alpha\} = \int C\{d\varepsilon^{pl}\} \tag{5.2}$$

where:

C = material parameter

$\{\alpha\}$ = back stress (location of the center of the yield surface)

Note that since Equation **5.1** is dependent on the deviatoric stress, yielding is independent of the hydrostatic stress state. When the equivalent stress is equal to the uniaxial yield stress, the material is assumed to yield. The yield criteria is therefore, Equation **5.3**

$$F = \left[\frac{3}{2}(\{s\} - \{\alpha\})^T [M](\{s\} - \{\alpha\})\right]^{\frac{1}{2}} \tag{5.3}$$

The bilinear kinematic hardening uses an associative flow rule, where the plastic strains occur in a direction normal to the yield surface. It yields, Equation **5.4**

$$\left\{\frac{\partial Q}{\partial \sigma}\right\} = \left\{\frac{\partial F}{\partial \sigma}\right\} = \frac{3}{2\sigma_e}(\{s\} - \{\alpha\}) \tag{5.4}$$

The associated flow rule with a von Mises yield criterion is known as the Prandtl-Reuss flow equation. BKIN follows kinematic hardening as a hardening rule and assumes that the yield surface remains constant in size and the surface translates in stress space with progressive yielding as shown in Figure **5.4**
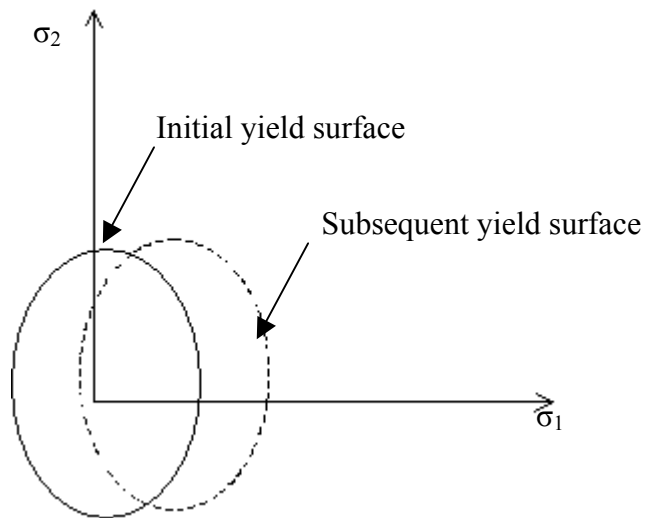
Figure **5.4**: Kinematic hardening rule

5.2.2 Material Properties

The present finite element analysis of the cold spray deposition process was performed using three materials: Ti-6Al-4V (substrate), nickel (particle coating), and graphite (core of the particle). Nickel is used as a wear resistant material and graphite as a

lube to develop self-lubricating coatings. Table **5.1** shows the material properties used in the modeling.

Table **5.1**: Material data for Ti-6Al-4V, nickel and graphite

Properties	Ti-6Al-4V	Nickel	Graphite
Density (kg/m^3)	4510	8908	1810
Elastic Modulus (GPa)	116	170	9.5
Poisson's Ratio	0.32	0.31	0.18
Yield Strength (MPa)	830	35	42
Tangent Modulus (GPa)	62	138	0.5

Based on the above material data, bilinear kinematic stress-strain curves were plotted for each material. Figure **5.5** shows the stress-strain curve for Ti-6Al-4V and nickel. Figure **5.6** shows the stress-strain curve for graphite. It should be noted that graphite was used due to the availability of its material properties. It is believed that the simulation results from graphite properties would be similar to hBN.
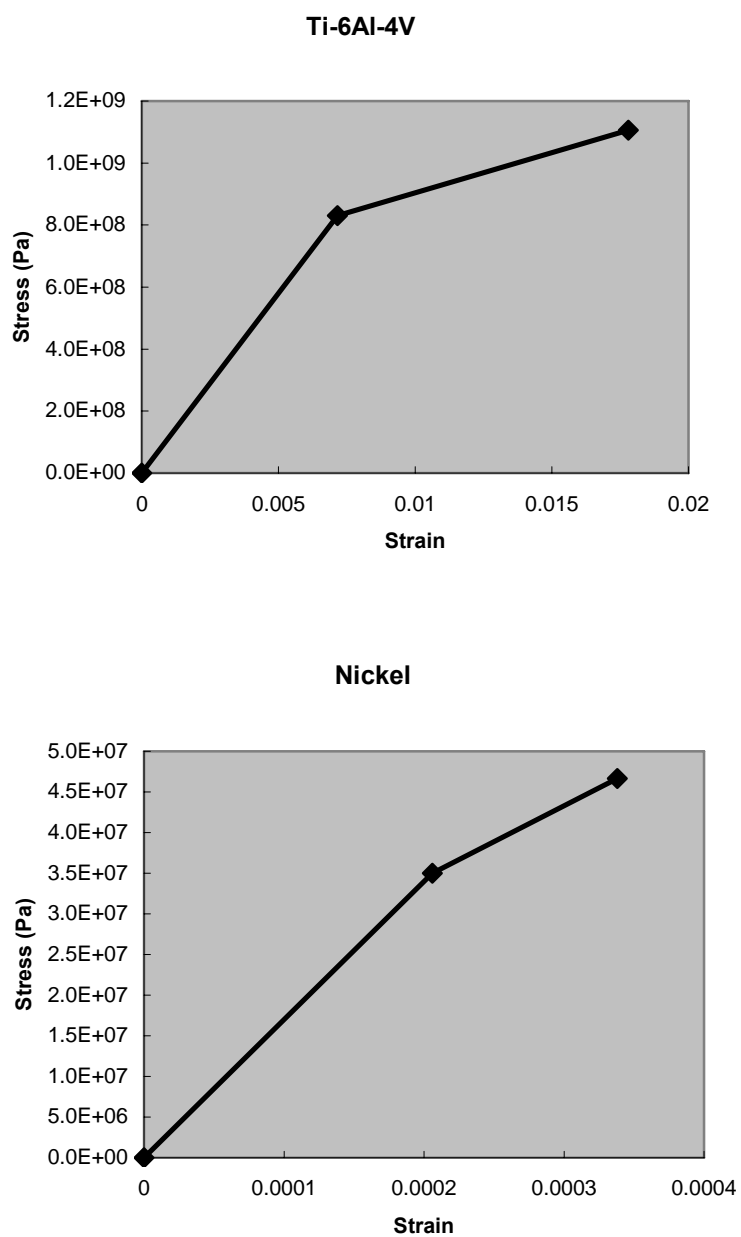
Ti-6Al-4V

Nickel

Figure **5.5**: Stress-strain curve for Ti-6Al-4V (top) and Nickel (bottom)
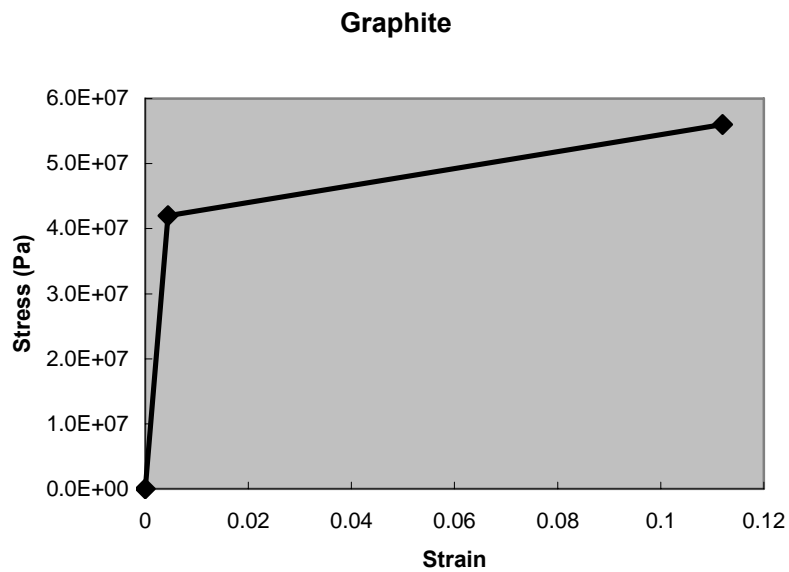
Figure **5.6**: Stress-strain curve for Graphite

5.3 Loading

5.3.1 Newton's Second Law

Newton's second law of motion pertains to the behavior of the objects for which all the existing forces are not balanced. The second law states that the acceleration of an object is dependent upon two variables: the net force acting upon the object and the mass of the object. In terms of an equation (Equation **5.5**), the net force is equated to the product of the mass times acceleration.

$$F_{net} = m * a \qquad\qquad (5.5)$$

5.3.2 Force Input

Newton's second law was used to convert the initial impact velocity experienced by the particle, into the force. This conversion encompasses the size (radius) and the density of the particle. Table **5.2** shows the conversion of velocity to force (velocity = 200 m/s) for a 20 µm graphite particle. Each mass was calculated from the volume and the density of the particle. Afterwards, the force was computed from the product of mass and acceleration (velocity/time).

Table **5.2**: Conversion of velocity to force (20 µm graphite particle at 200 m/s)

Velocity (m/s)	Diameter (m)	Density (kg/m^3)	Time (s)	Force (N)
200	2.0 E-05	1.81 E+03	1.0 E-06	1.52 E-03

In the composite particle, the input force was calculated for three regions: the lube particle, the nickel coating and the interface between the two. Figure **5.7** shows a schematic of composite particle and the regions of force application.
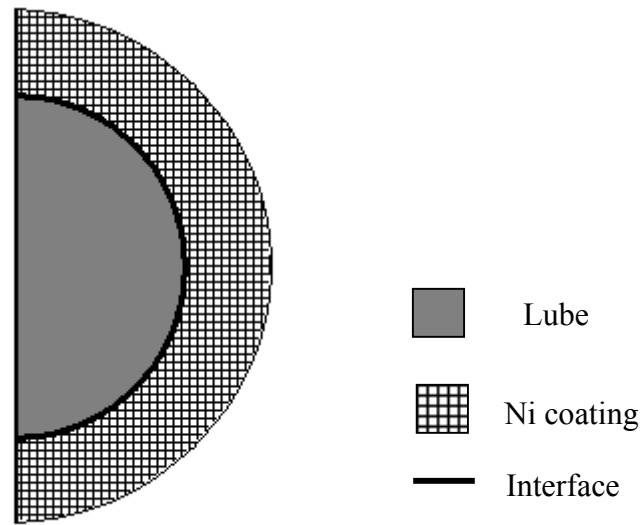
Figure **5.7**: Schematic of the composite particle

The calculated force was applied transiently in one load-step. The load step was divided into maximum of 3000 substeps to satisfy the transient time integration rules (which usually dictate a minimum integration time step for an accurate solution). For convergence purposes, the equilibrium iterations were set to 70. Figure **5.8** shows a schematic of the type of loading used in the present analysis.
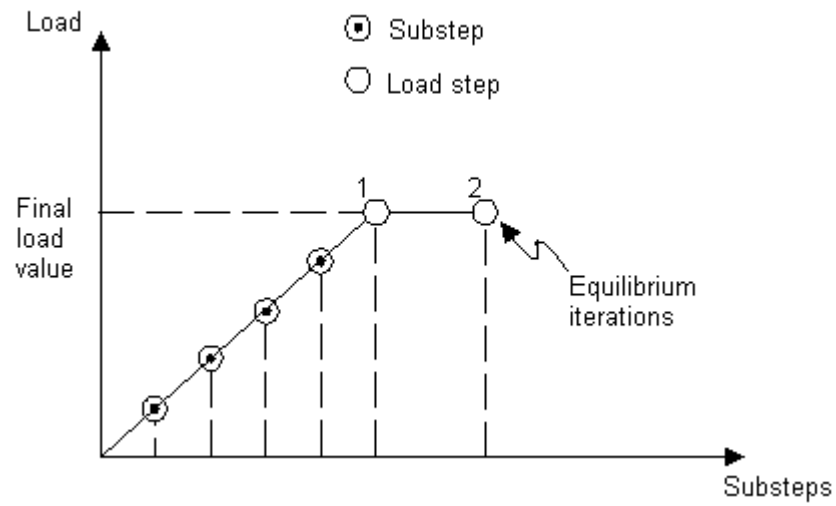
Figure **5.8**: Type of loading used present analysis
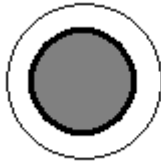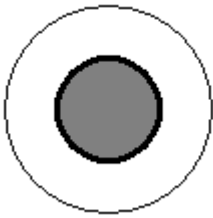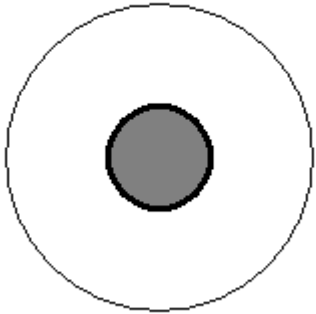
5.4 Modeling Cases

Three main cases of modeling were dealt in the present work to study the composite particle impact during cold spray process.

- CPT5: Diameter Lube = 20 μm and Ni coating thickness = 5 μm

- CPT10: Diameter Lube = 20 μm and Ni coating thickness = 10 μm

- CPT20: Diameter Lube = 20 μm and Ni coating thickness = 20 μm

Table **5.3** gives the number of elements and force applied for all the three cases.

Table **5.3**: Modeling cases

	CPT5	CPT10	CPT20
Schematic			
Total particle size, μm	30	40	60
# of elements	773	811	839
Force$_{lube}$(500 m/s), N	0.002	0.002	0.002
Force$_{Ni\ coat}$ (500 m/s), N	0.02	0.07	0.2
Force$_{interface}$(500 m/s), N	0.01	0.03	0.12

5.5 Assumptions and Restrictions

The assumptions and restrictions inherent in the model just described carry much importance due to the simplistic nature of modeling in this research. Prior simulations of the cold spray process has been done mainly based on ballistic modeling techniques and assumptions. As a result, most of the information is classified and hard to find in open literature. Moreover, complex codes/models were used to solve the above problems on cluster of servers. Therefore, this section of thesis lists the important assumptions in the present work.

1. The particle is assumed to impact the substrate in the direction normal to the substrate surface. This assumption makes the problem at hand axisymmetric, eliminating the need for a computationally intensive three-dimensional analysis.

2. The net force experienced by the particle is assumed to be the force due to the mass and acceleration of the particle. The gravity effects are neglected.

3. Ramped loading is considered, its value increases gradually at each substep, with the full value occurring at the end of the loadstep.

4. Lube particles are assumed to be a perfect sphere.

5. Both lube and Ni coating surrounding it is considered to be uniform and smooth.

6. All the analyses are done for first layer of particles depositing the cold spray process.

7. The lube particles are assumed to follow elastoplastic material response. This assumption avoids compatibility issues in material models.

8. Once contact is established in the analysis, model assumes a bonded condition between particle and the substrate.

9. Due to the axisymmetric nature, modeling is done in +X quadrant.

10. All the elements used have non-zero area.

11. The graphite core is assumed to behave similarly to hBN and molydag; this was necessary because properties are not available for hBN and molydag.

Chapter 6

Discussion

The objective of this chapter is to assess the results presented in Chapter 4, the

model discussed in Chapter 5, and determine whether they support the hypothesis of this

thesis. The chapter is divided into two broad categories that include a discussion of both

experimental and modeling results. The experimental results discussion is based on the

strategies used to formulate the feedstock (ST1 to ST4). The modeling results are being

discussed in light of equivalent von Mises stress and strain developed at varying impact

velocities. Three main cases of composite particle impact are considered based on the

thickness of nickel coating around the lubricant particle. Finally, a condition of bonding

is derived for the composite particle on a Ti-6Al-4V substrate.

6.1 Discussion of Experimental Results

The powders as described in Table **3.1** were used in formulating the feedstock for

cold spray deposition by employing different techniques or strategies. All the feedstock

formulation techniques weren't successful in development of self-lubricating coatings.

This section discusses the results of each strategy followed by the reason behind its

failure or success. It was found that each of the previous strategy laid the foundation for the next until an optimum feedstock formulation technique.

6.1.1 Admixed Feedstock (ST1)

As already discussed, Table 4.3 shows the list of cold spray experiments performed with un-coated admixed powders. Although, the list consists of experiments done with both nitrogen and helium as a carrier gas, this strategy only discusses the experiments performed with nitrogen.

During the experiments, the Ti-6Al-4V substrates were sprayed in two sets: 3 – 3 – 6 and 9 – 9 – 18 passes (Figure 6.1).
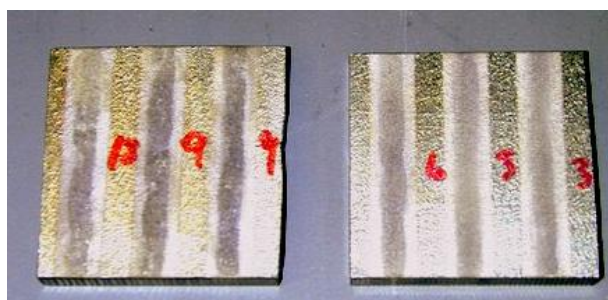
Figure 6.1: Ni+MoS$_2$ coating pattern on Ti-6Al-4V substrates

During the subsequent examinations and physical handling, it was observed that the coatings were relatively robust and without significant porosity. Due to the difficulty in identifying MoS$_2$, energy dispersive spectroscopy (EDS) was used on the coating cross-sections. EDS revealed 1 wt% MoS$_2$ embedded particles in the coating formed from Ni+2%MoS$_2$ feedstock (Figure 6.2).
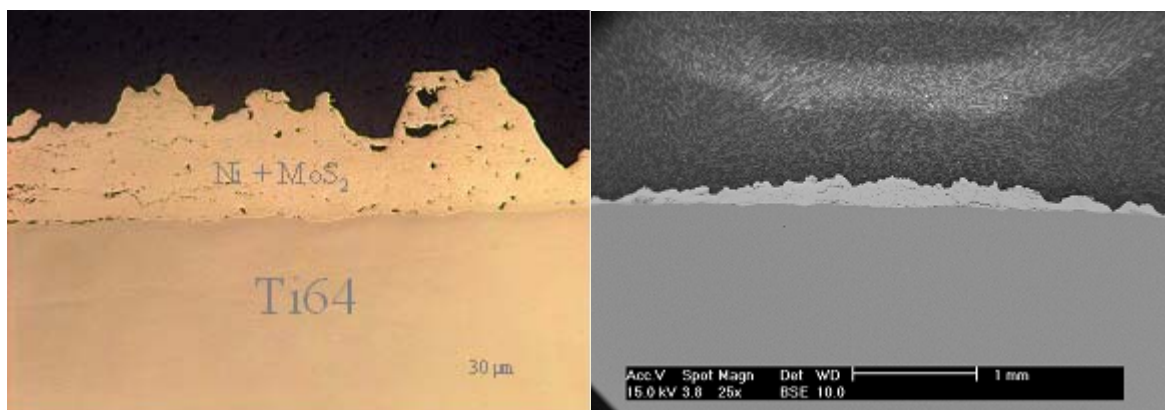
Figure **6.2**: Optical and SEM image of coating cross-section

In order to increase the amount of MoS_2 in the coating, feedstock's with 3 and 4 wt%

MoS_2 were sprayed on the Ti-6Al-4V substrates. Interestingly, it was observed that the

coating thickness decreased with the increase in weight percent of MoS_2 (Figure **4.10**). At

4wt% MoS_2, the coating thickness not only decreased as compared to lower weight

fractions (2 & 3 wt% MoS_2), but also experienced a sharp dip at 18 passes. This confirms

the lack of ability of particles to build on themselves at higher percentages of MoS_2.

Therefore, it can be concluded that MoS_2 prevents build-up of coating both on the

substrate and itself. As such, the next challenge was to incorporate higher weight

fractions of MoS_2 in the coating with a simultaneous build-up of the coating thickness.

The next set of cold spray runs were done with Ni + 2 wt% MoS_2 (3 μm)

feedstock. The idea was to incorporate smaller size MoS_2 particles in the nickel matrix.

Surprisingly, there was no-coating build up with both set of passes (3 – 3 – 6 and 9 – 9 –

18). Based on this finding, it can be reasoned that the particle size and shape of the solid-

lube plays an important role in the coating build-up. MoS_2 has a lower density (5.06 g/cc)

and flake-like structure as compared to the more spherical nickel (8.48 g/cc) and therefore, requires a greater volume for acceleration. In addition, the likely (and assumed) absence of plasticity of the lubricant would also hinder adhesion to either the Ti substrate or Ni matrix.

There was no coating build-up with admixed Ni+hBN feedstock. Again, density differential between hBN and Ni plays a role in preventing adhesion. Therefore, there was a need to identify a technique to process feedstock with lube particles embedded in the nickel matrix.

6.1.2 Sintered Feedstock (ST2)

Sintering is a powder metallurgical technique where powders are heated (below melting point) until they adhere to each other. Sintering is usually the final processing step in manufacturing via powder metallurgy. The feedstock powders ($Ni + MoS_2$) were sintered at three different temperatures (600, 715 and 800°C) in order create sinter-bond between nickel particles resulting in entrapment of lube particles. Figure **6.3** shows the micrographs of Ni+MoS$_2$ feedstock's sintered at different temperatures.

600ºC

715ºC
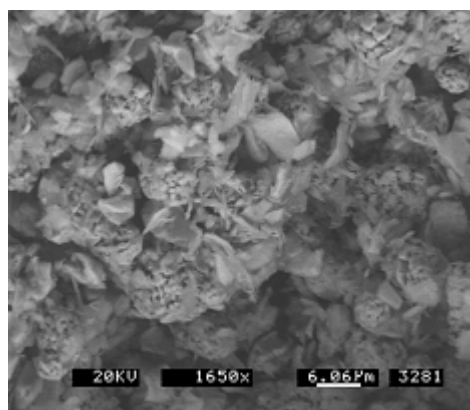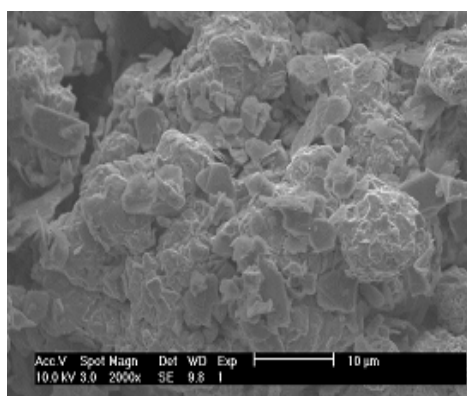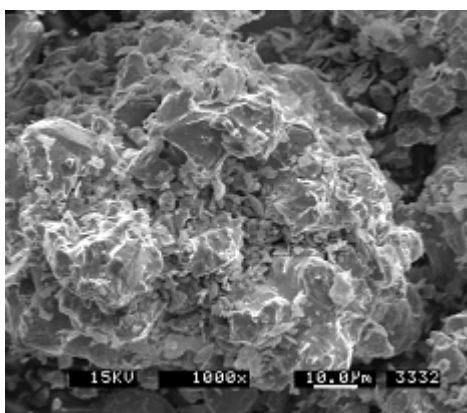
800ºC

Figure **6.3**: Micrographs of Ni + MoS₂ sintered feedstock's

Neither of the above sintered feedstock was successful in a coating build-up (using nitrogen as carrier gas). This can be attributed to the sintering temperature. At low temperatures (<600ºC), the sintering forces weren't sufficient to create sinter-bonds

between the particles and sintering at higher temperatures ($>600^{o}$C) resulted in hardened agglomerates, which did not deform plastically upon impact.

6.1.3 Milled Feedstock (ST3)

In order to avoid the segregation of admixed feedstock powders during spraying, the as-received powders were milled together so as to create metallurgical bonding between Ni and lubricant powders. During spraying of these mechanically milled powders, the feedstock powder aggregates of a relatively large size were destroyed upon the impact on the substrate, resulting in highly irregular surface. Figure **6.4** shows that particle bombardment onto the first layer of the coating actually eroded the previously deposited coating layers. When the milling time was increased, the powders experienced cold working and strain-hardening. As a result, the milled powders were unable to deform on impacting the substrate. It appears that most of the MoS_2 in the agglomerates was lost while fracturing.

Figure **6.4**: Top view of an as-sprayed Ni-7wt%MoS$_2$ coating using milled feedstock

Figure **6.5** shows the coatings produced by milled Ni+2wt%hBN feedstock. The agglomerates formed during milling disintegrated in-flight during cold spray process.
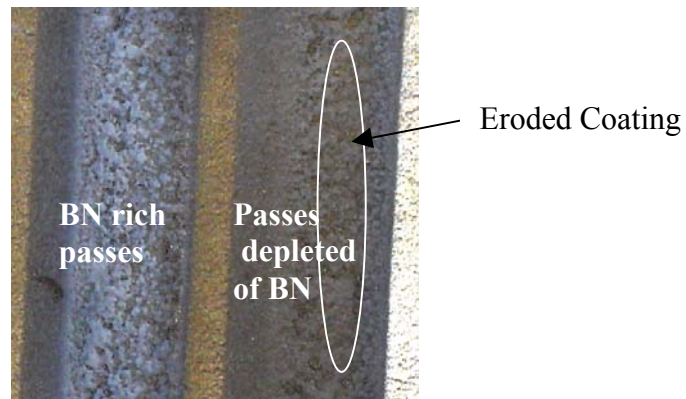
Figure **6.5**: Ni + 2wt% hBN coating using milled feedstock

6.1.4 Nickel coated hBN

From the previously discussed techniques, it became imperative to trap lubricant particles in the nickel matrix prior to cold spray deposition. As mentioned in earlier chapters, commercially available Ni coated hBN composite powder was used to fulfill the above requirement. When sprayed, pure Ni coated hBN (Ni Coat hBN) disintegrated in-flight resulting in minimal coating build-up. To alleviate this problem, pure Ni Coat hBN was admixed with pure Ni. Table **4.5** shows the different feedstock with admixed pure Ni and Ni Coat hBN. Figure **4.19** shows high magnification SEM image of the coatings. The coating has a rough surface morphology, with many humps on the surface formed through the stacking of the deformed powder particles. Detailed examination clearly confirms the presence of hBN particles on the surface of the coatings. Since the hBN is non conductive, it appears as bright white spots on the SEM image. Figure **6.6** shows the elemental map of the top surface of the coating. The figure shows the presence of hBN but could not be quantified with confidence due to the large difference in atomic number of Ni and hBN.
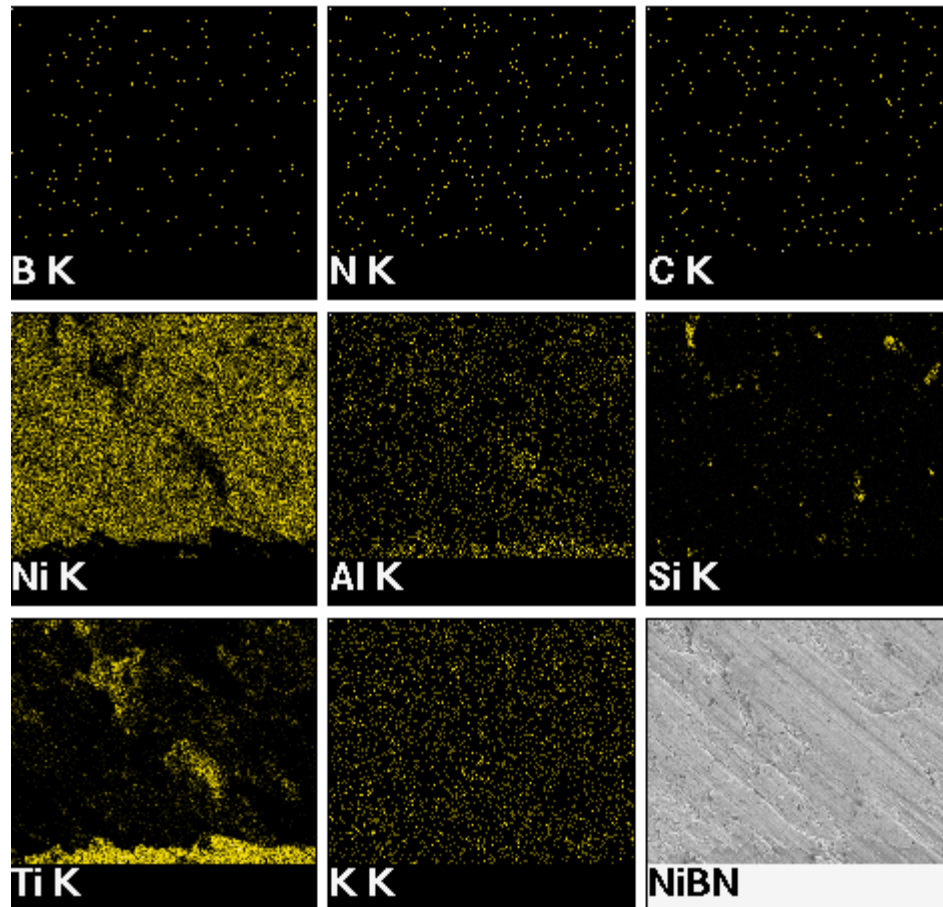
Figure **6.6**: Elemental map of Ni+Ni Coat hBN coating top surface

Figure **6.7** shows high magnification SEM images of the Ni+Ni Coat hBN

coatings. From the size of hBN embedded in the coatings, it is obvious that the large Ni

coated hBN powders have fractured upon impact. As expected, the smaller Ni powder

deformed extensively and adhered to the surface. The large particles not only provided a

tamping effect for improved adhesion, but some of the fragments of the fractured powder

were trapped into the coating because of the surrounding and incoming Ni particles.

Consequently, a relatively dense and coherent coating with hBN particles embedded in the Ni matrix was formed.
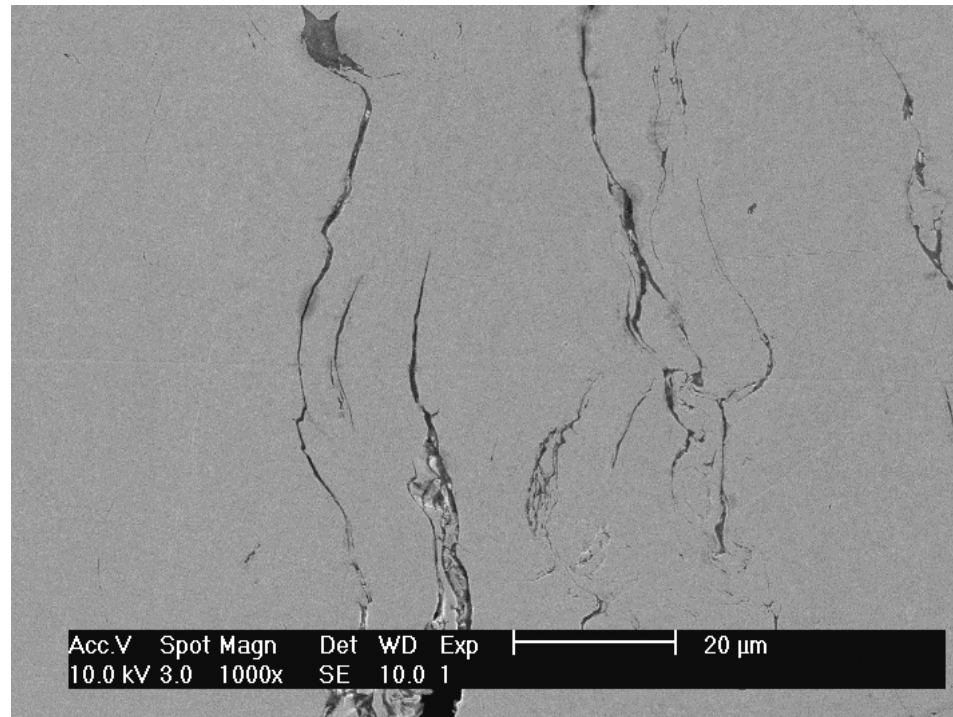
Figure **6.7**: SEM image of Ni + NiCoathBN coating

6.2 Modeling Discussion

Several research groups have carried out experimental and numerical studies to establish the effect of various process parameters such as: type of carrier gas, the average particle velocity, the gas pre-heat temperature, particle impact angle, etc. on the

efficiency of cold spray process. The effect of these parameters can be considered as being well established and rationalized. However, all these studies have mainly considered pure-element powder deposition. In the present research, finite-element modeling has been attempted to study the aspects of composite particle impact. This section discusses the modeling results in order to help elucidate and eventually optimized the bonding condition for the composite particles in cold spray process.

6.2.1 General Aspects of Particle Impact

Figure **6.8** shows the development of equivalent von Mises stresses in the composite particles with different nickel coating thickness and the Ti-6Al-4Vsubstrate during the impact, for three velocities of 300, 600 and 900 m/s.
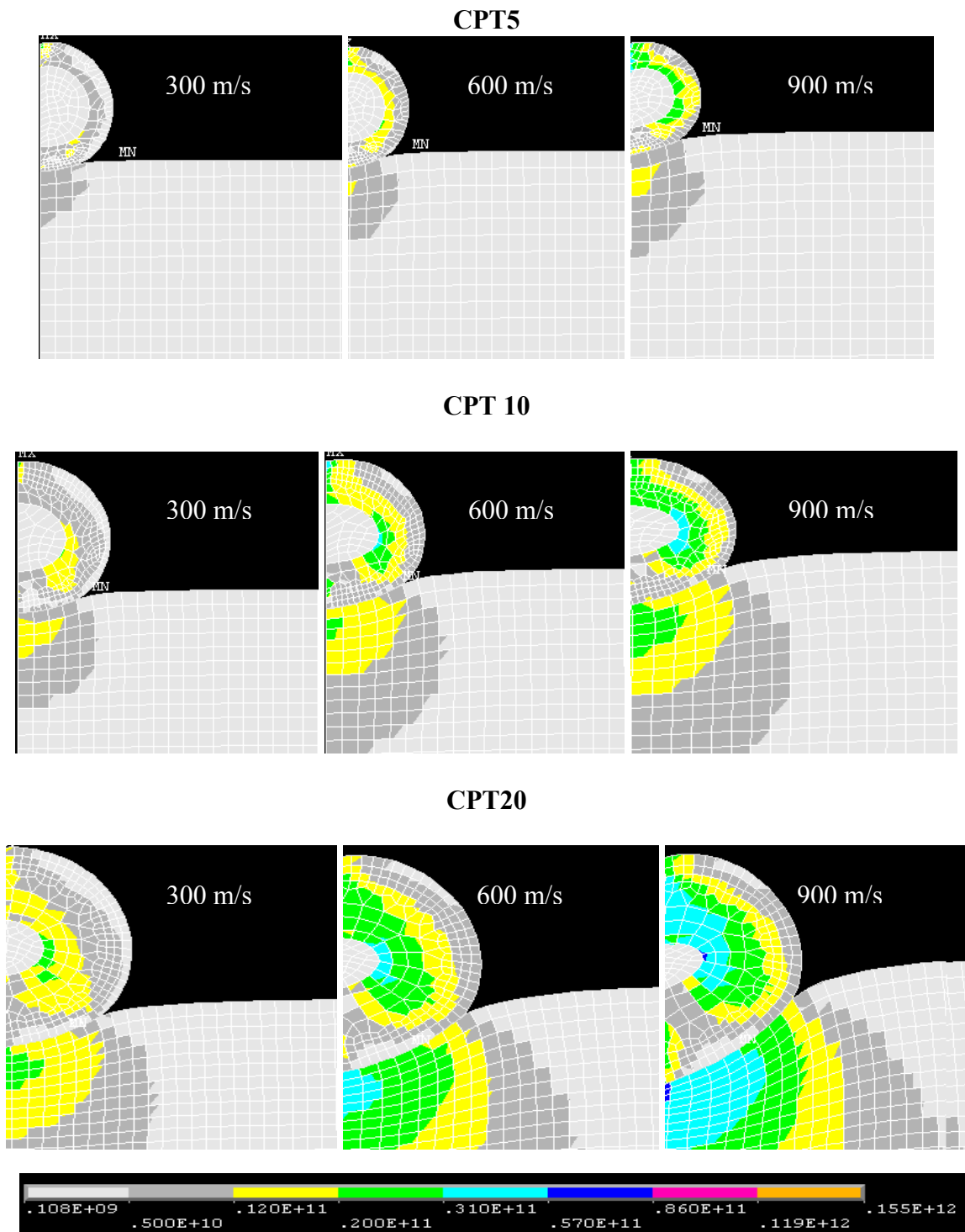
CPT5

CPT 10

CPT20

Figure **6.8**: Contour plots of von Mises stress in Pascal (t = 1 μs)

The contours indicate the equivalent von mises stresses for each of the three cases (CPT5, CPT10 and CPT20) at three different velocities. The figure shows the stress development starting from the axisymmetric edge of both the particle and the substrate and moving to the interior of the geometry. The stress development is more severe for the higher velocity impact in a respective case. At the same velocity, particles with thicker nickel coatings exert higher stress on the substrate compared to a particle having thin nickel coating (Figure **6.9**).
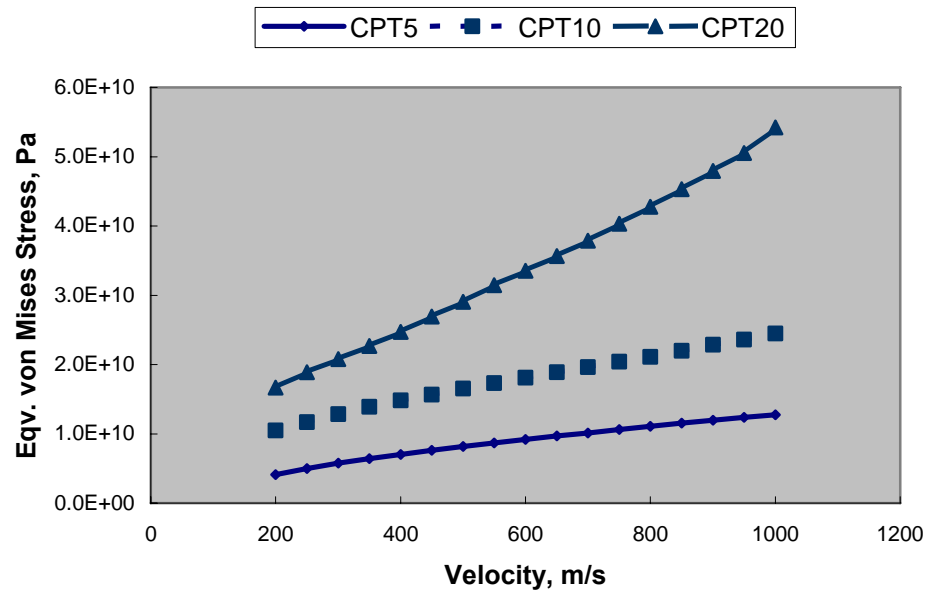
Figure **6.9**: Substrate stresses at different velocities for t = 1μs

The trend in substrate stresses can be attributed to two factors- the total particle size and the thickness of nickel coating. As the total particle size increases from 30 μm (CPT5) to 60 μm (CPT20), the mass of the particle increases, which subsequently increases the force experienced by the particle and hence its stresses. It should be noted that the

composite particles consist of two materials: graphite and nickel; graphite has a lower density (1.81 g/cm^3) as compared to the nickel (8.908 g/cm^3). At the same velocity, the graphite particle will experience less force than the nickel particle (assuming same particle size for both). Therefore it can be concluded that, the composite particle is composed of a low density and a high-density region, with high-density areas experiencing higher forces than a low-density area. Hence, particles with thicker nickel coatings have larger high-density regions compared to particles having thin nickel coatings, resulting in higher stresses. Similar behavior is observed in von mises strains (Figure **6.10**).
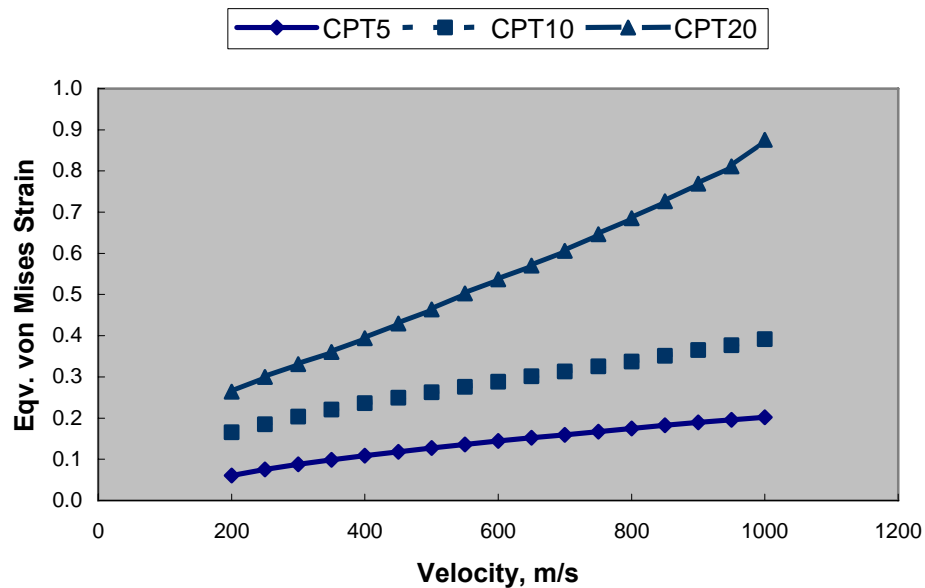
Figure **6.10**: Strains in substrate at different velocities at t = 1 μs

The development of stresses (equivalent von Mises) in the particle is shown in Figure **6.11**. The figure shows the variation of stress with impact velocity at a node in the

nickel coating for all the three composite particle cases. In all the cases, a similar trend is observed. There is a monotonic decrease in stress up to a particular velocity and beyond that the stress increases. The velocity at which the stress is minimum can be termed as the velocity at inflexion (V_{inf}). It can be seen from the figure that the velocity at inflexion depends on the thickness of the nickel coating around the graphite particle. With an increase in thickness of the nickel coating, V_{inf} decreases. For a 5 μm thick coating, V_{inf} equals 700 m/s and 500 m/s for a 20 μm thick coating, respectively. At this point, V_{inf} can be related to the critical particle velocity (V_{crit}), below which particles leads to only abrasion and densification of the substrate with no coating build-up. For a composite particle with 20 μm thick nickel coating (CPT20), there is sharp increase in the stresses beyond the velocity of inflexion. This is a result of the large particle size compared to CPT5 and CPT10.
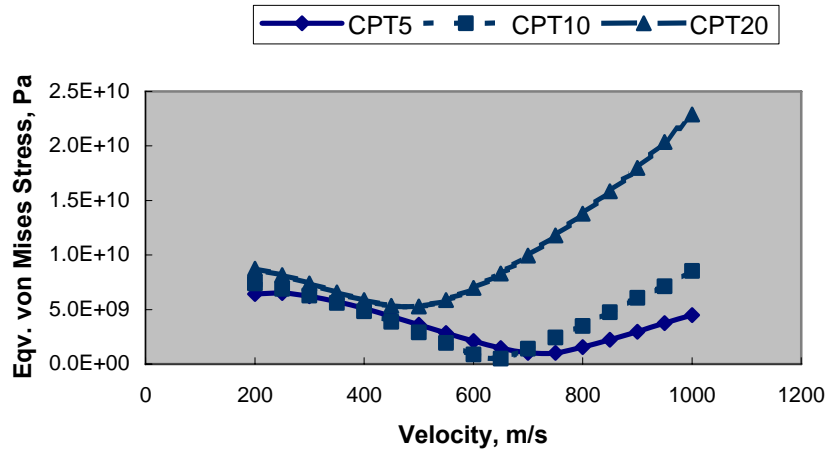
Figure **6.11**: Stresses in the particle (Ni coating) at different velocities

A similar trend is observed in equivalent strains at a same node, though the effect is not as prominent as seen in stresses (Figure **6.12**).
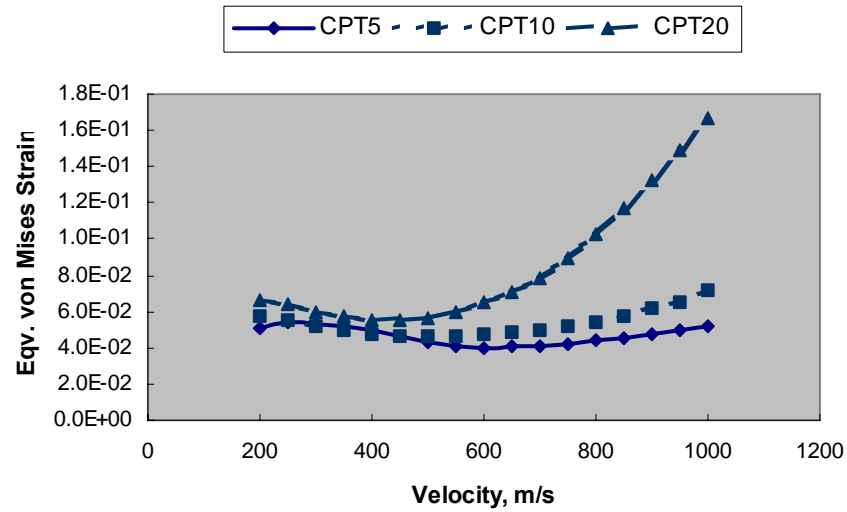
Figure **6.12**: Strains in the particle (Ni coating) at different velocities

6.2.2 Condition for Bonding

The interpretation of the results of modeling has so far been based on the development of stresses and strains at a selected node separately for both particle and the substrate. In order to obtain a better insight to the condition of bonding in the composite particle impact, the particle-substrate stress and strain development was considered in conjunction with each other. This can be illustrated by plotting equivalent von Mises stress against impact velocity for each of the respective cases. Figure **6.13** shows the stresses developed at the interface for a CPT5 composite particle.
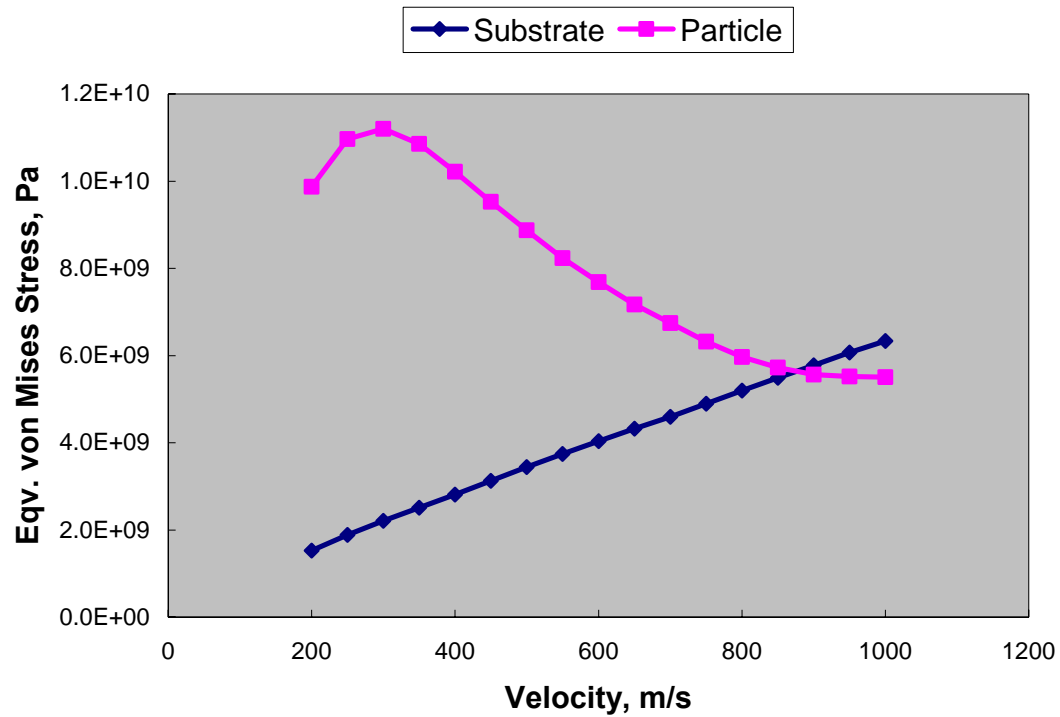
Figure **6.13**: Particle and substrate stresses at different impact velocities for CPT5

It can be seen from the above figure, the stresses in the particle decreases and in the substrate increases with an increase in the impact velocity. The higher the impact velocity, the larger is the interfacial contact area between particle and the substrate (as shown in Figure **6.14**).
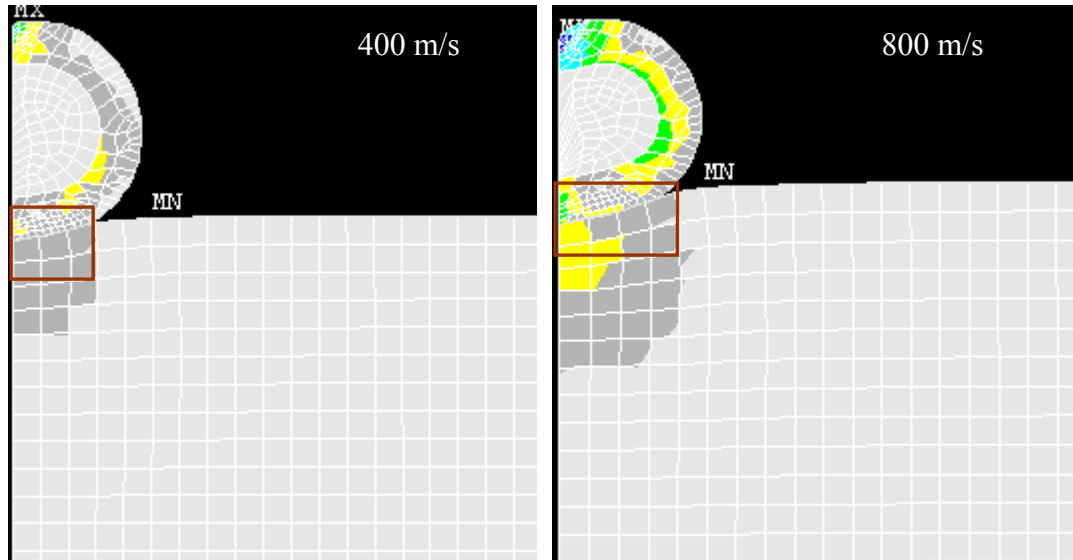
Figure **6.14**: Contact area for CPT5 at two impact velocities

The increase in contact area results in stress reduction in the particle resulting in lower stresses at higher impact velocities. As the particle comes in contact greater with the substrate, the more force it exerts, resulting in higher stresses in the substrate. As seen from Figure **6.13** the particle stresses are almost equal to the substrate stresses at an impact velocity of 850 m/s, and beyond that particle stresses are lower than the substrate. This velocity can be termed as velocity at intersection (V_{int}), which can be related to the critical velocity (V_{cr}), above which bonding takes place in cold gas spraying. V_{int} calculated from stresses developed in the particle and the substrate can play an important role in determination of critical velocity or the condition of bonding.

When the nickel coating thickness around the lubricant particle is increased from 5 μm (CPT5) to 10 μm (CPT10), the stresses in the particle and the substrate takes the form as shown in Figure **6.15**. The stresses in the substrate increase at a constant rate with

the increase in velocity. The particle stresses drop with an increase in impact velocity, before it reaches minimum at 750 m/s as a impact velocity. The velocity at intersection (V_{int}) for this case is somewhere between 350 and 400 m/s. Beyond this velocity, the particle stresses are lower than the substrate stresses, therefore, can be considered as a condition of bonding.
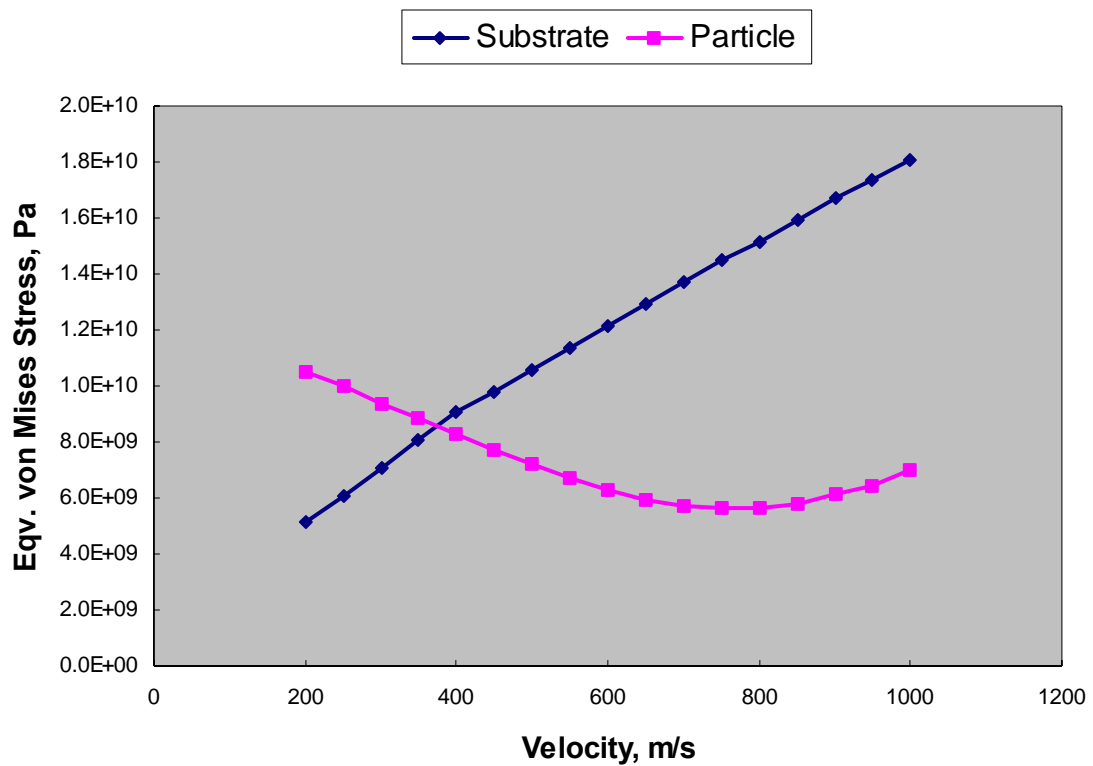
Figure **6.15**: Particle and substrate stresses at different impact velocities for CPT10

For a coating thickness of 20 μm (CPT20), the particle stresses are lower than the substrate stresses for the entire range of velocity (200 to 1000 m/s). As shown in Figure **6.16**, there is no evident velocity at intersection (V_{int}) for the range of velocities studied. However the trend for both the particle and the substrate stresses is similar to the

ones observed in CPT5 and CPT10. The maximum stress of 45 GPa is observed at a

impact velocity of 1000 m/s, which is 2X than the maximum stress obtained in CPT10 at

the same velocity. This can be attributed to the larger size particle in CPT20 as compared

to CPT10.
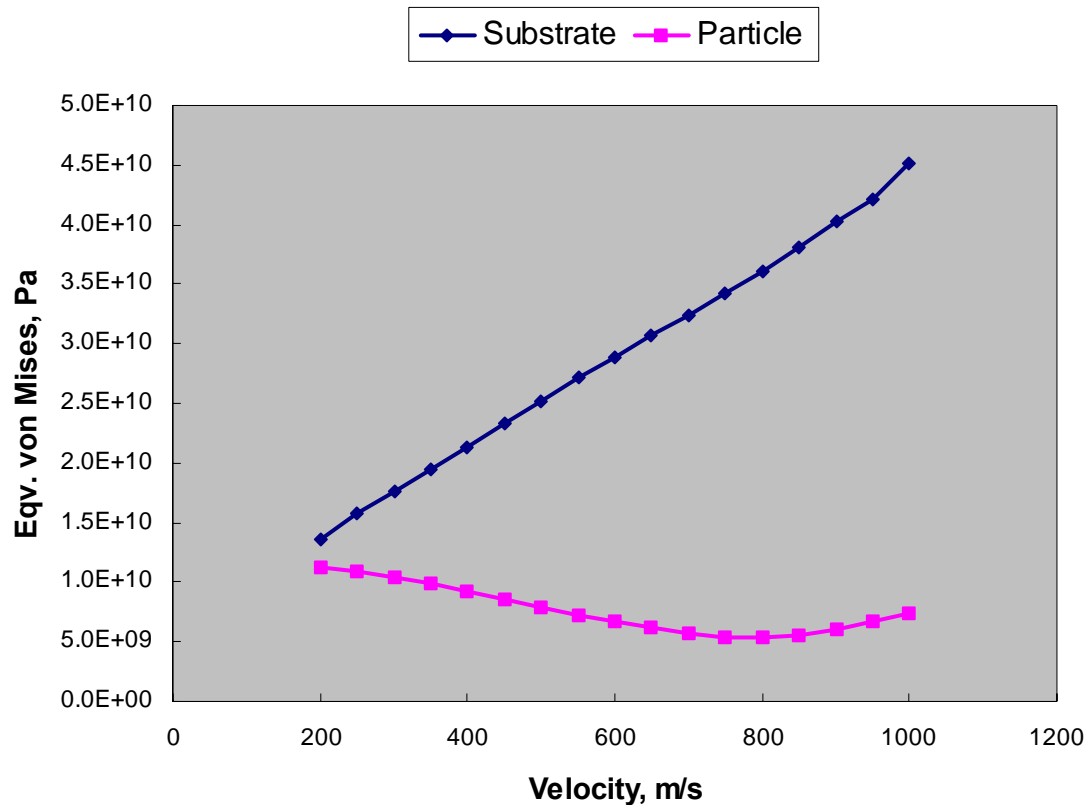
Figure **6.16**: Particle and substrate stresses at different impact velocities for CPT10

It is important to note that the particle size has a higher effect on the stresses

produced in the substrate than the stresses produced in the particle. When the particle

stresses in CPT10 and CPT20 are compared, as shown in Figure **6.17**, they follow a

similar trend and are almost equal in magnitude. From this discussion, the particle

stresses individually carries less importance in determination of the critical velocity. It is the stresses in the substrate and the particle, observed in conjunction with each other, which helps determining the velocity at intersection (V_{int}), which can than be related to the critical velocity.
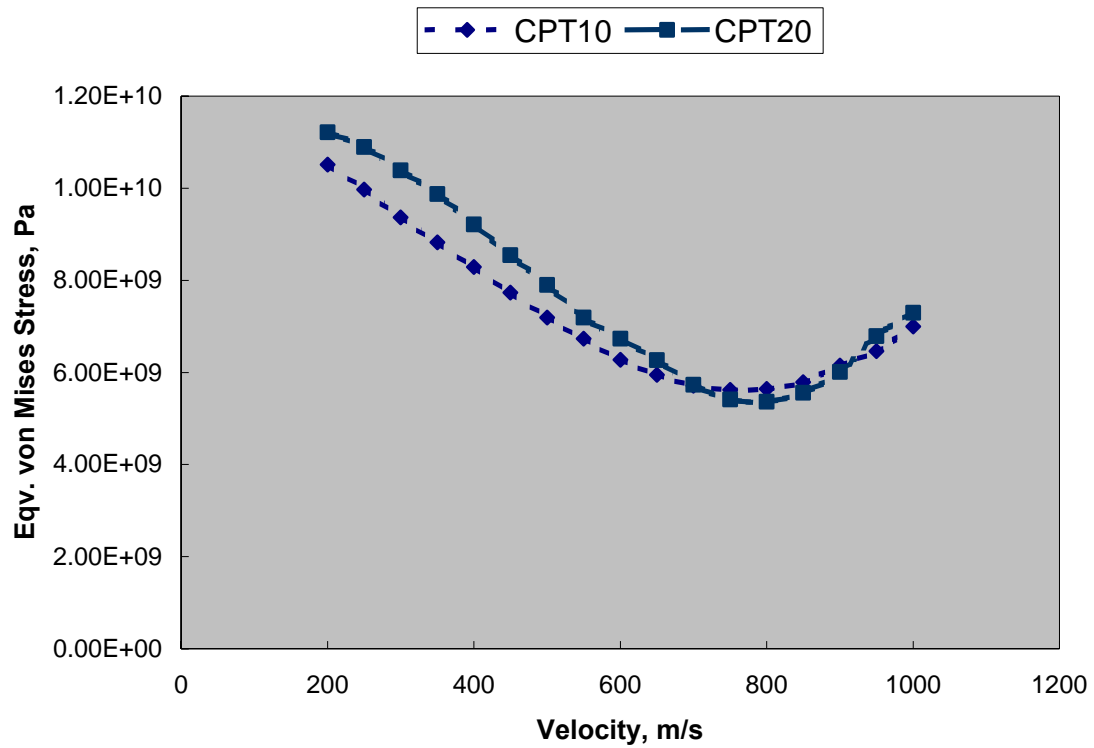
Figure **6.17**: Particle stresses in CPT10 and CPT20

6.2.3 Comparison to single-element particle

In order to verify the modeling approach, it was imperative to model single-element particle impact in the cold spray process. The idea behind this effort was to

compare and contrast it to the composite particle impact. It is important to note that the results presented in this section could not be compared to the earlier studies performed with pure nickel due to the assumptions and restrictions mentioned in Chapter 5.

A pure nickel particle (SPT20, radius = 20 μm) was analyzed using axisymmetric model and compared to the composite particle of the same size (CPT10). Both the single-element particle and the composite particle were 40 μm in diameter. Figure **6.18** shows the development of stresses in the substrate and the single-element (SPT20) particle with the particle impact velocity.
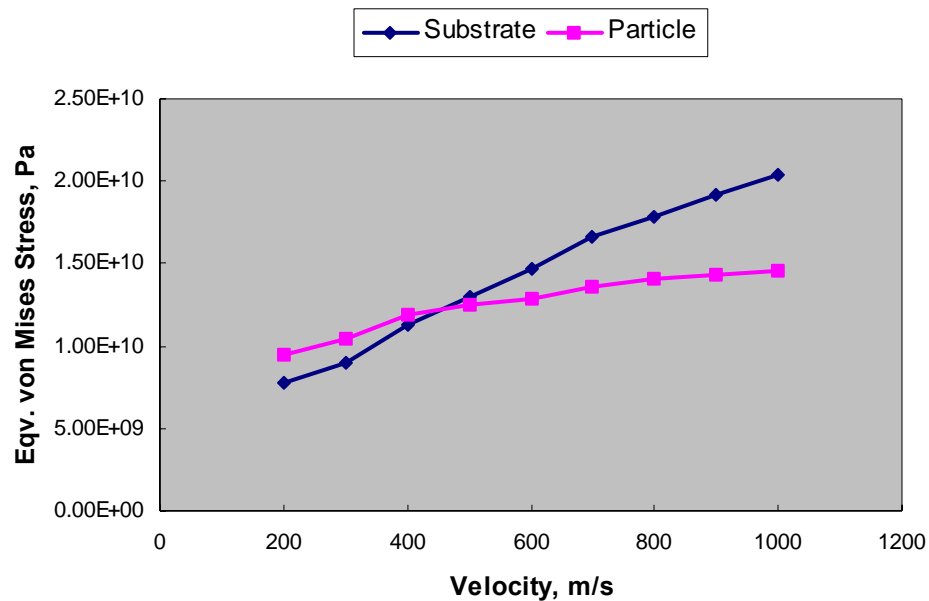
Figure **6.18**: Particle and substrate stresses at different impact velocities for SPT10

The velocity at intersection is observed in the above figure, beyond which, the particle stresses are lower than the substrate stresses. In order to compare the single-element particle to the composite particle, Figure **6.16** and Figure **6.18** are overlaid on each other

(Figure **6.19**). The stresses in the substrate follow similar trend both in SPT20 and CPT10 cases, and are higher in SPT20 due to the absence of lower density lubricant in the single-element particle. The single-element particle exerts greater force on the substrate than the composite particle having a lubricant core. The stresses in the particle follow a different trend in the SPT20 compared to the CPT10. In both the cases, the stresses produced in the particle at almost equal at the lower impact velocities. As the impact velocity increases, the particle stresses in SPT20 increases, whereas the composite particle stresses (CPT10) decreases with velocity. The composite particle consists of lower density core material (graphite), which acts as a stress absorber, resulting in lower stresses. The stresses in pure nickel particle increases as a result of work hardening. The difference in stresses can also be interpreted because of the difference in elastic modulus of graphite and nickel. The pure nickel particle is stiffer than the composite particle, resulting in higher stresses.
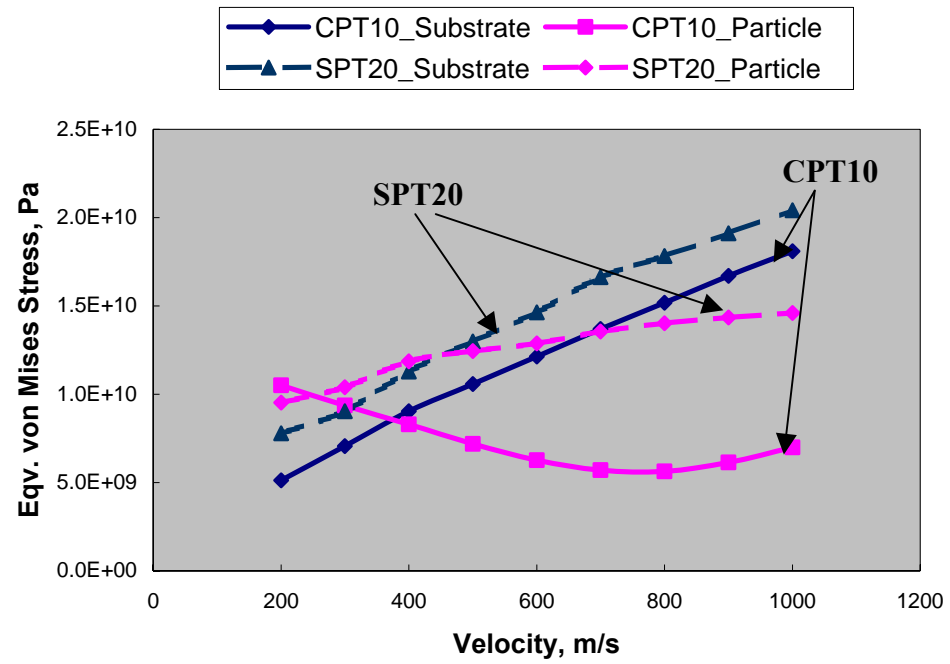
Figure **6.19**: Overlay of Figure **6.15** and Figure **6.18**

Chapter 7

Conclusions and Recommendations

The present work demonstrates that the cold spray process can be used to deposit self-lubricating coatings for the Ti-6Al-4V alloy. Feedstock formulation is an important step in the development of composite coatings via the cold spray processing. A feedstock with coated lubricant particles provides an advantage over admixed powders for achieving higher a weight percent of the lubricant in the final coating. Helium as a carrier gas provides sufficient particle velocity, which is imperative for the development of composite coatings. A transient finite-element analysis has been used to study the interaction between composite particles and the substrate during cold spray processing. The results of modeling provided stress and strain distributions, which can be used to find the conditions required for bonding. The interaction between the particle and substrate stresses plays an important role in determining the critical particle velocity for deposition. This chapter explains these conclusions along with the suggestions for future work.

7.1 Summary and Conclusions

The cold spray process uses high velocity rather than high temperature to produce coatings, thereby avoiding/minimizing many deleterious high temperature reactions,

which are characteristics of the thermal sprayed coatings. The particles are in solid-state as they hit the substrate and both the gas and particle temperature remain below the melting point of the spray material. Therefore, formation of coatings mainly occurs due to the kinetic energy of the particles. More importantly, the method allows the introduction of lower temperature lubricants directly into the coating with all the anticipated benefits for reducing friction and related wear damage. For the first time, the cold spray process was used to deposit Ni-MoS$_2$ and Ni-hBN self-lubricating coatings.

By virtue of its high ductility, nickel particles undergo high plastic deformation and adhere well to a Ti-6Al-4V substrate during cold spraying. However, the likely absence of plasticity of the lubricant powders inhibits the formation of a good bond with the substrate as well as building up itself. Therefore, feedstock formulation is an important part to develop self-lubricating coatings via cold spraying.

It was possible to coat up to 7 wt% MoS$_2$ in the nickel matrix using the admixed feedstock with helium as a carrier gas. However, the admixed Ni-hBN feedstock resulted in poor coating build-up. This can be attributed to the difference in densities of nickel and hBN, with the less dense lubricant powders being accelerated to higher velocities than the nickel. As a result, higher amounts of lube were incorporated in initial passes whereas subsequent passes were depleted of lube. To alleviate this problem, a composite powder (Ni coated hBN) was used as feedstock. Ni coated hBN has a thin nickel coating which breaks upon impact. Therefore, the composite powder was admixed with pure nickel powder, to build the coatings. This helped incorporating BN particles in the coatings. The highest percentage of hBN (6 wt%) was obtained using Ni + 30 wt% Ni coated hBN feedstock.

Helium with its slightly larger ratio of specific heat and substantially lower molecular weight than nitrogen, was expected to provide higher gas velocities, and consequently, higher particle velocities. Given these advantages, all the other feedstock required helium as the carrier gas except the Ni-MoS$_2$ feedstock. Even in case of admixed Ni-MoS$_2$ feedstock, it was possible to double the amount of lube entrapped in the coatings by spraying with helium instead of nitrogen.

In cold spraying, processing techniques do not allow a precise description of each impact. The impact velocity corresponding to an individual crater is also not available. However, the use of modeling can provide the definition of each impacting event and allow the study of the variation of any parameter(s) to obtain trends. For the first time, finite-element modeling has been applied to study the composite particle impact in the cold spray process. A finite-element model based on elastic-plastic materials behaviors when subjected to mechanical load was used to predict the critical particle velocity for producing self-lubricating coatings.

Three different cases based on the thickness of nickel coating on each particle were modeled. During the development of equivalent von Mises stresses in the particle with varying impact velocity, a monotonic decrease in stress was observed up to a particular velocity and beyond that the stress increased. The velocity at which the stress is minimum can be termed as the velocity at inflexion (V_{inf}). With an increase in thickness of the nickel coating, V_{inf} decreases. For a 5 μm thick coating, V_{inf} equals 700 m/s and 500 m/s for a 20 μm thick coating, respectively. V_{inf} can be related to the critical particle velocity (V_{crit}), below which particles cause only abrasion and densification of the substrate with no coating build-up.

When both the particle and the substrate stresses were observed at a distance from the interface, the particle stresses decreased and the substrate stresses increased with an increase in velocity. The decrease in particle stresses can be explained due to the increase in the interfacial area between the particle and the substrate at higher velocities. A point of stress intersection was observed at a particular velocity, where the particle stresses were equal to the substrate stresses. This velocity can be termed as velocity at intersection (V_{int}). The stresses in the particle were lower than the substrate stresses beyond the velocity at intersection (V_{int}). Therefore, V_{int} can be related to the critical velocity (V_{cr}), below which the particles would rebound back and above which bonding takes place in cold gas spraying. It was observed that V_{int} decreases with an increase in the nickel coating thickness in the coated particle.

The present investigation predicts the critical particle velocity whose value most significantly depends on the mechanical properties of the powder particles and the substrate materials. It also depends on the conversion of the particle impact velocity to the mechanical force experienced by the particle. The prediction of a critical velocity in the cold spray process helps in choosing the carrier gas and the size of the composite particle (i.e., thickness of the particle coating). Figure **7.1** shows a schematic to summarize the contribution of this research. It shows the critical velocity with varying thickness of the nickel coating in the composite particle. It also depicts the respective regimes of nitrogen and helium as a carrier gas.

This work also provides an inexpensive gateway to the otherwise complex and computationally expensive impact-contact modeling. The model is validated in both the single and the composite particle impact. However, due to its pure mechanical nature, the

current analyses under-predicts the critical particle velocity. To precisely predict the

critical impact velocity for composite particles, the analysis can be extended to other

materials behaviors such as- strain-rate, thermal softening, and heating due to frictional,

plastic and viscous dissipation. Overall, this research provides a foundation for composite

particle deposition via cold spray processing.
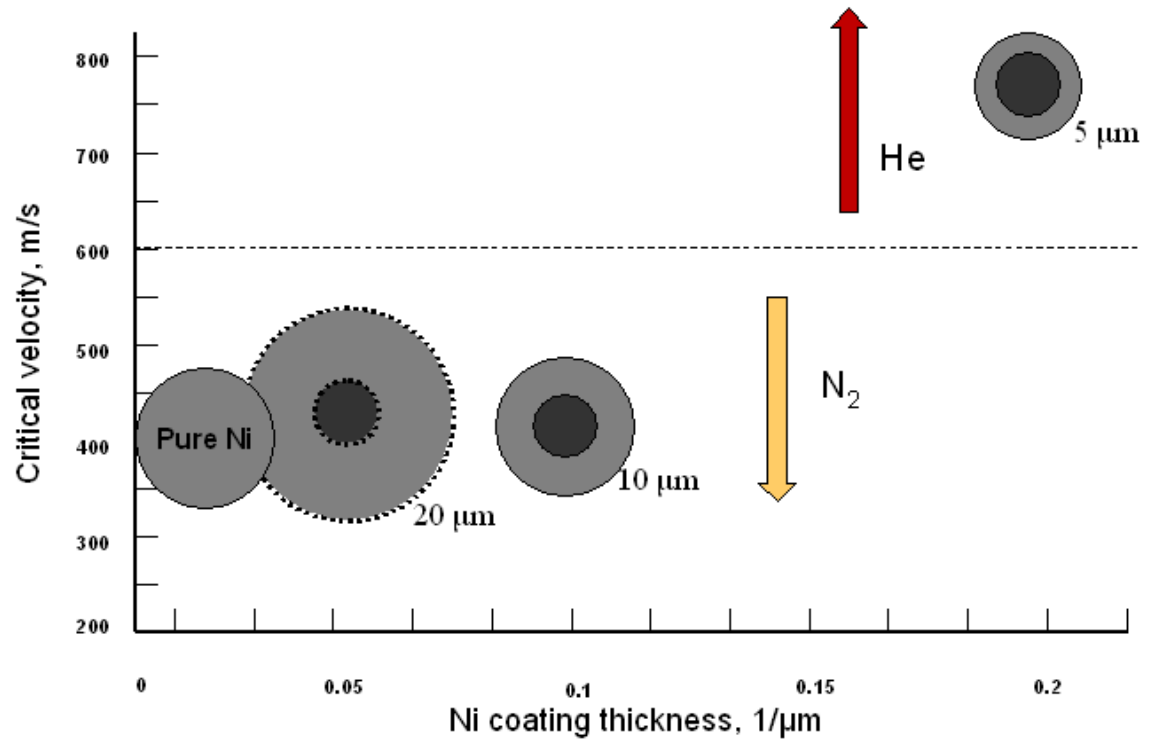
Figure **7.1**: Schematic showing the critical velocity based on modeling

7.2 Future Recommendations

Coated powder as a feedstock in the cold spray process was shown to be an appropriate choice for composite coatings. However, it needs to be admixed with pure nickel in order to better entrap the lubricant in the final coatings. This in-turn limits the maximum weight percentage of the lubricant in the coatings. To alleviate such problems, an optimum coated powder needs to be designed. From the modeling results, it is recommended to use a 20 μm lube particle with a 20 μm thick nickel coating. Based on the simulations, it is predicted that such a configuration would result in lowering the critical impact velocity and increase the percentage of lube in the coatings.

Admixing the coated powder with pure nickel also results in microstructural inhomogeneity, namely, the lubricant particles are not uniformly distributed in the coatings. Simultaneous injection of the composite and pure nickel powder at the throat of the nozzle is recommended as an alternative to the pre-mixed powders, which should lead to a better lubricant distribution in the coatings.

In the axisymmetric model, nodal forces have been applied for each corresponding velocity. Nevertheless, for large particle sizes (>60 μm) and high particle impact velocities, this resulted in unrealistic shape along the symmetry axis after deformation. In order to prevent this, a three-dimensional analysis is suggested.

The material properties used for the current analysis have been based on the data reported for bulk materials, and an assumption was made regarding the plasticity of lubricant material (hBN, graphite). More experiments are recommended in order to identify the properties of the feedstock powder, which may deviate substantially from

those of the assumed bulk materials. In addition, the present work does not take into account any phase changes in the material. A phase change could in particular influence the results of modeling for systems with allotropic transformations, such as iron.

The analysis in the present research is based on a first layer deposition and does not consider the subsequent layers. Further modeling is suggested on the deposition behavior the subsequent layers and their effect on the first layer adhesion.

Bibliography

1. Wu, L., et al., *Analysis of diamond-like carbon and Ti MoS$_2$ coatings on Ti-6Al-4V substrates for applicability to turbine engine applications.* Surface and Coatings Technology, 2000. **130**(2-3): p. 207-217.

2. Antoniou, R.A. and T.C. Radtke, *Mechanisms of fretting-fatigue of titanium alloys.* Materials Science & Engineering A, 1997. **237**: p. 229-240.

3. Buchholtz, B.W. and F.M. Kustas, *Effects of surface pretreatment of Ti-6Al-4V on the adhesion and wear lifetimes of sputtered MoS2 coatings.* TribologyTransactions, 1996. **39**(2): p. 330-337.

4. Blau, P.J., *Friction, Lubrication and Wear Technology, ASM Handbook.* Vol. 18. 1992. p. 9.

5. Taylor, D.W. and V. Chandrasekaran, *Fretting Fatigue: Advances in Basic Understanding and Applications.* Fretting Fatigue: Advances in Basic Understanding and Applications, ed. Y. Mutoh, S.E. Kinyon, and D.W. Hoeppner. 2003, West Conshohocken, PA: ASTM International.

6. Vincent, L., *Fretting Fatigue ESIS 18*, ed. R.B. Waterhouse and T.C. Lindley. 1994, London: Mechanical Engineering Publications. p. 323-337.

7. Eden, E.M., W.N. Rose, and F.L. Cunningham. in *Proceedings of Institute of Mechanical Engineers*. 1911.

8. Alic, J.A., A.L. Hawley, and J.M. Urey, *Formation of fretting fatigue cracks in 7075-T7351 aluminium alloy.* Wear, 1979. **56**(2): p. 351-361.

9. Gaul, D.J. 1978, MS Thesis, Rensselaer Polytechnic Institute: Troy, NY.

10. Fenner, A.J. and J.E. Field. in *Proceedings of N.E. Coast Institute of Engineers and Shipbuilders*. 1960.

11. Hamdy, M.M. and R.B. Waterhouse, *FRETTING FATIGUE BEHAVIOUR OF Ti-6Al-4V AT TEMPERATURES UP TO 600°C.* Wear, 1979. **56**: p. 1-8.

12. Fayeulle, S., P. Blanchard, and L. Vincent, *Fretting behavior of titanium alloys.* Tribological Transaction, 1993. **36**: p. 267-275.

13. Reeves, R.K. and D.W. Hoeppner, *The effect of fretting on fatigue.* Wear, 1976. **40**: p. 395-397.

14. Nishioka, K. and K. Hirawakawa, Journal of Society of Mechanical Engineers, 1969. **12**(51): p. 397-407.

15. Waterhouse, R.B. and D.E. Taylor, *The Initiation of Fatigue Cracks in a 0.7% Carbon Steel by Fretting.* Wear, 1979. **17**(2): p. 139-147.

16. Hoeppner, D.W. and G.L. Goss. *Corrosion Fatigue: Chemistry, mechanics and microstructure*. in *NACE-2, National Association of Corrosion Engineers*. 1972. Houston, TX.

17. Doboromirski, J. and I.O. Smith, *Metallographic Aspects of Surface Damage, Surface Temperature and Crack Initiation in Fretting Fatigue.* Wear, 1987. **117**: p. 347-357.

18. Endo, K. and H. Gota, *Initiation and Propagation of Fretting Fatigue Cracks.* Wear, 1976. **38**: p. 311-324.

19. Wharton, M.H., D.E. Taylor, and R.B. Waterhouse, *METALLURGICAL FACTORS IN THE FRETTING-FATIGUE BEHAVIOUR OF 70/30 BRASS AND 0. 7% CARBON STEEL.* Wear, 1973. **23**: p. 251-260.

20. Alic, J.A. and A.L. Hawley, *On the Early Growth of Fretting Fatigue Cracks.* Wear, 1979. **56**: p. 377-389.

21.   Adibnazari, S. and D.W. Hoeppner, *Characteristics of the fretting fatigue damage threshold.* Wear, 1992. **159**: p. 43-46.

22.   Adibnazari, S. and D.W. Hoeppner, *Fretting fatigue normal pressure threshold concept.* Wear, 1993. **160**: p. 33-35.

23.   Waterhouse, R.B., *Fretting Corrosion*. 1972, Oxford: Pergamon Press.

24.   Betts, K., *Wear resistant coatings for titanium alloys: Fretting fatigue of uncoated Ti-6Al-4V*. 1971: AFML-TR-71-212, Wright-Patterson Air Force Base, Ohio.

25.   Waterhouse, R.B., *Fretting Fatigue*. 1981, London: Applied Science Publishers.

26.   Hermanek, F.J., *Thermal spray terminology and company origins*. 2001, Materials Park, Oh: ASM International. 73.

27.   Alkhimov, A.P., V.F. Kosarev, and A.N. Papyrin, *A Method of Cold-Gas Dynamic Compaction.* Sov. Phys. Dokl., 1991. **35**(12): p. 1047-1049.

28.   Alkhimov, A.P., et al., *Gas-dynamic spraying method for applying a coating*. 1994, Papyrin, Anatoly Nikiforovich: United States. p. 1-13.

29.   Alkhimov, A.P., et al., *Method and Device for Coating*. 1995: European. p. 1-18.

30.   McCune, R.C., et al. *Characterization of Copper and Steel Coatings Made by the Cold Gas-Dynamic Spray Method.* in *Thermal Spray: Practical Solutions for Engineering Problems.* 1996.

31.   Vlcek, J., et al., *A systematic approach to material eligibility for the cold-spray process.* Journal of Thermal Spray Technology, 2005. **14**(1): p. 125-133.

32.   Ya, L.W. and L.C. Jiu. *Optimization of spray conditions in cold spraying based on numerical analysis of particle velocity.* in *Transactions of the Nonferrous Metals Society of China.* 2004. Shenzhen, China: Editorial Office of Transactions of Nonferrous Metals Soc.

33.   Papyrin, A.N., et al. *Experimental Study of Interaction of Supersonic Gas Jet with a Substrate Under Cold Spray Process.* in *Thermal Spray 2001 New Surfaces for a New Millennium: Proceedings of the International Thremal Spray Conferences.* 2001. Singapore, Singapore: ASM International.

34.   Stoltenhoff, T., et al. *Optimization of Cold Spray Process.* in *Thermal Spray 2001: New Surfaces for a New Millennium.* 2001. San Franciso, CA, USA: Mater. Res. Soc.

35. Smith, M.F., et al. *Cold spray direct fabrication - high rate, solid state, material consolidation*. in *MRS Fall Meeting - Symposium V, 'Solid Freeform and Additive Fabrication'*. 1998. Boston, MA: Materials Research Society.

36. Kreye, H. and T. Stoltenhoff. *Cold Spraying- A Study of Process and Coating Characteristics*. in *International Thermal Spray Conference*. 2000.

37. Karthikeyan, J., et al. *Cold Spray Processing of Titanium Powder*. in *International Thermal Spray Conference*. 2000.

38. Karthikeyan, J., et al. *Cold Sprayed Nanostructured WC-Co*. in *International Thermal Spray Conference*. 2001.

39. Vlcek, J., et al. *Kinetic Powder Compaction Applying the Cold Spray Process- A Study on Parameters*. in *International Thermal Spray Conference*. 2001.

40. Decker, M.K., et al. *Microstructure and Properties of Cold Spray Nickel*. in *Proceedings of the International Thermal Spray Conference*. 2001. Singapore, Singapore: ASM International.

41. Korobkina, N.N., S.V. Panin, and A.P. Alkhimov. *Investigation of plastic deformation development at mesoscale level in composition with cold-sprayed coatings*. in *Proceedings of the 7th International Scientific and Practical*

Conference of Students, Post-graduates and Young Scientists. Modern Techniques and Technology. MTT'2001. 2001. Tomsk, Russia: IEEE.

42. Raletz, F., et al. *Characterization of cold-sprayed nickel-base coatings*. in *Proceedings of the International Thermal Spray Conference*. 2004. Osaka, Japan: ASM International, 9639 Kinsman Road, OH 44073-0002, United States.

43. Cheng, O. *Equipment engineering and process control for cold spraying*. in *Proceedings of the International Thermal Spray Conference*. 2004. Osaka, Japan: ASM International, 9639 Kinsman Road, OH 44073-0002, United States.

44. Shipway, P.H., et al. *Improved titanium coatings for biomedical applications using cold gas spraying*. in *Transactions - 7th World Biomaterials Congress*. 2004. Sydney, Australia: Biomaterials 2004 Congress Managers, Sydney, NSW 2001, Australia.

45. Jen, T.-C., et al., *Numerical Investigations on Cold Gas Dynamic Spray Process with Nano- and Microsize Particles.* International Journal of Heat and Mass Transfer, 2005. **48**: p. 4384-4396.

46. Barradas, S., et al., *Application of laser shock adhesion testing to the study of the interlamellar strength and coating-substrate adhesion in cold-sprayed copper coating of aluminum.* Surface and Coatings Technology, 2005. **197**(1): p. 18-27.

47. Lee, H.Y., et al., *Thin film coatings of WO3 by cold gas dynamic spray: A technical note.* Journal of Thermal Spray Technology, 2005. **14**(2): p. 183-186.

48. Li, C.-J., W.-Y. Li, and Y.-Y. Wang, *Formation of metastable phases in cold-sprayed soft metallic deposit.* Surface and Coatings Technology, 2005. **198**(1-3): p. 469-473.

49. Villafuerte, J., *Cold spray: A new technology.* Welding Journal (Miami, Fla), 2005. **84**(5): p. 24-29.

50. Ajdelsztajn, L., et al., *Cold spray deposition of nanocrystalline aluminum alloys.* Metallurgical and Materials Transactions A: Physical Metallurgy and Materials Science, 2005. **36**(3): p. 657-666.

51. Wang, H.-D., et al., *Microstructures and tribological properties on the composite MoS 2 films prepared by a novel two-step method.* Materials Chemistry and Physics, 2005. **91**(2-3): p. 494-499.

52. Balani, K., et al., *Effect of carrier gases on microstructural and electrochemical behavior of cold-sprayed 1100 aluminum coating.* Surface and Coatings Technology, 2005. **195**(2-3): p. 272-279.

53.   Zhang, D., P.H. Shipway, and D.G. McCartney, *Cold gas dynamic spraying of aluminum: The role of substrate characteristics in deposit formation.* Journal of Thermal Spray Technology, 2005. **14**(1): p. 109-116.

54.   Kim, H.-J., C.-H. Lee, and S.-Y. Hwang, *Fabrication of WC-Co coatings by cold spray deposition.* Surface and Coatings Technology, 2005. **191**(2-3): p. 335-340.

55.   Kim, H.-J., C.-H. Lee, and S.-Y. Hwang, *Superhard nano WC-12%Co coating by cold spray deposition.* Materials Science and Engineering A, 2005. **391**(1-2): p. 243-248.

56.   Alkhimov, A.P., *Gas-Dynamic Spraying. A Study of a Plane Supersonic Two-Phase Jet.* Journal of Applied Mechanics and Technical Physics, 1997. **38**(2): p. 324-330.

57.   McCune, R.C., et al. *An exploration of the cold gas-dynamic spray method for several material systems*. in *Proceedings of the 8th National Thermal Spray Conference*. 1995. Houston, TX: ASM International.

58.   Bishop, C.V. and G.W. Loar, *Practical pollution abatement method for metal finishing.* Plat. Surf. Finish, 1993. **80**: p. 37.

59.   Dykhuizen, R.C. and M.F. Smith, *Gas dynamic principles of cold spray.* Journal of Thermal Spray Technology, 1998. **7**(2): p. 205-212.

60.   Alkhimov, A.P., et al., *Specific features of microparticle deformation upon impact on a rigid barrier.* Journal of Applied Mechanics and Technical Physics, 2000. **41**(1): p. 188-192.

61.   Heimann, R.B., *Plasma-spray coatings: principles and applications*. 1996: VCH. 339.

62.   Matejka, D. and B. Benko, *Plasma spraying of metallic and ceramic materials*. 1989: John Wiley and Sons Ltd. 280.

63.   Pawlowski, L., *The science and engineering of thermal spray coatings*. 1995: John Wiley and Sons. p. 414.

64.   Grujicic, M., et al., *Adiabatic shear instability based mechanism for particles/substrate bonding in the cold-gas dynamic-spray process.* Materials and Design, 2004. **25**(8): p. 681-688.

65.   Grujicic, M., et al., *Flow analysis and nozzle-shape optimization for the cold-gas dynamic-spray process.* Proceedings of the Institution of Mechanical Engineers, Part B:Journal of Engineering Manufacture, 2003. **217**(11): p. 1603-1613.

66.   Borchers, C., et al. *Deformation microstructure of cold gas sprayed coatings*. in *Dislocations and Deformation Mechanisms in Thin Films and Small Structures (Material Research Society Symposium)*. 2001. San Francisco, CA: Materials Research Society.

67.   Dykhuizen, R.C., et al., *Impact of high velocity cold spray particles.* Journal of Thermal Spray Technology, 1999. **8**(4): p. 559-564.

68.   Papyrin, A.N., et al. *On the interaction of high speed particles with a substrate under the cold spraying*. in *Proceedings of the International Thermal Spray Conference*. 2002. Dusseldorf, Germany: DVS-Verlag.

69.   Gartner, F., et al. *Numerical and Microstructural Investigations of the Bonding Mechanisms in Cold Spraying*. in *Thermal Spray 2003: Advancing the Science & Applying the Technology*. 2003. Orlando, FL: ASM International.

70.   Zhang, D., P.H. Shipway, and D.G. McCartney. *Particle-substrate interactions in cold-gas dynamic spraying*. in *International Conference of Thermal Spray*. 2003. Orlando, Fl.

71. Brasher, D.G. and D.J. Butler, *Explosive welding: principles and potentials.* Advanced Materials and Processes, 1995. **147**: p. 37-38.

72. Murr, L.E., *Shock waves for industrial applications*. 1988, New Jersey: Noyes Publications.

73. Crossland, B., *Explosive welding of metals and its applications*. 1982, Oxford: Claredon Press.

74. El-Sobky, H., *Mechanics of explosive welding*, in *Explosive welding*, T.Z. Blazynski, Editor. 1983, Applied Science Publishers: London.

75. Hammerschmidt, M. and H. Kreye, *Microstructure and bonding mechanism in explosive welding*, in *Shock waves and high strain rate phenomena in metals*, M.A. Meyers and L.E. Murr, Editors. 1981, Plenum Press: New York. p. 961-972.

76. Meyers, M.A., N.N. Thandhani, and L.-H. Yu, *Explosive shock wave consolidation of metal and ceramic powders*, in *Shock waves for industrial applications*, L.E. Murr, Editor. 1988, Noyes Publications: New Jersey. p. 265-334.

77. Nesterenko, V.F., *Dynamic loading of porous materials: potential and restrictions for novel material applications*, in *Metallurgical and Materials*

Application of Shock-Wave and High Strain-Rate Phenomenon, L.E. Murr, K.P. Staudhammer, and M.A. Meyers, Editors. 1995, Elsevier: Amsterdam. p. 3-13.

78.   Rosato, A.D., T. Vreeland, and F.B. Prinz, *Manufacture of Powder Compacts.* International Materials Reviews, 1991. **36**(2): p. 45-61.

79.   Raybould, D., *The properties of stainless steel compacted dynamically to produce cold interparticle welding.* Journal of Materials Science, 1981. **16**: p. 589-598.

80.   Schmidt, T., F. Gartner, and H. Kreye. *High strain rate deformation phenomena in explosive powder compaction and cold gas spraying*. in *International Thermal Spray Conference*. 2003. Orlando, FL: ASM International.

81.   Grujicic, M., G.B. Olson, and W.S. Owen, *Mobility of the $\beta_1-\gamma_1$ martensitic interface in Cu-Al-Ni. I. Experimental measurements.* Metallurgical Transactions, 1985. **16**: p. 1723.

82.   Grujicic, M., et al., *Computational analysis of the interfacial bonding between feed-powder particles and the substrate in the cold-gas dynamic-spray process.* Applied Surface Science, 2003. **219**(3-4): p. 211-227.

83.   Assadi, H., et al., *Bonding Mechanisms in Cold Gas Spray.* Acta Materialia, 2003. **51**: p. 4379-4394.

84.   Stoltenhoff, T., H. Kreye, and H.J. Richter, *An Analysis of the Cold Spray Process and its Coatings.* Journal of Thermal Spray Technology, 2002. **11**(4): p. 542-550.

85.   Tokarev, A.O., *Structure of Aluminium Powder Coatings Prepared by Cold Gas Dynamic Spraying.* Metal Science and Heat Treatment, 1996. **38**(3-4): p. 36-39.

86.   Gilmore, D.L., et al., *Particle velocity and deposition efficiency in the cold spray process.* Journal of Thermal Spray Technology, 1999. **8**(4): p. 576-582.

87.   Papyrin, A., *Cold Spray Technology.* Advanced Materials and Processes, 2001. **159**(9): p. 49-51.

88.   Hertel, E.S., et al., *Lance CTH: A Software Family for Multi-Dimensional Shock Physics Analysis, Shock Waves at Marseille,* ed. R. Brun and L.Z. Dumitrescu. 1995: Springer-Verlag. p. 377-382.

89.   Steinberg, D.J., S.G. Cochran, and M.W. Guinan, *A constitutive model for metals applicable at high-strain rate.* Journal of Applied Physics, 1980. **51**(3): p. 1498-1504.

90.   Steinberg, D.J. and C.M. Lund, *A constitutive model for strain rates from 10^{-4} to 106 s^{-1}.* Journal of Applied Physics, 1989. **65**(4): p. 1528-1533.

91.   Zerilli, F.J. and R.W. Armstrong, *Dislocation-mechanics-based constitutive relations for material dynamics calculations.* Journal of Applied Physics, 1987. **61**(5): p. 1816-1825.

92.   Walsh, J.M., R.G. Shreffler, and F.J. Willig, *Limiting Conditions for Jet Formation in High Velocity Collisions.* Journal of Applied Physics, 1953. **24**(3): p. 349-359.

93.   Vlcek, J., et al. *Melting upon particle impact in the cold spray process.* in *Materials Week 2002, International Congress on Advanced Materials, Their Processes and Applications.* 2002. Munich Germany.

94.   Papyrin, A.N., S.V. Klinkov, and V.F. Kosarev. *Modeling of Particle-Substrate Adhesive Interaction Under the Cold Spray Process.* in *International Conference of Thermal Spray.* 2003. Orlando, FL: ASM International.

95.   Olson, G.B., J.F. Mescall, and M. Azrin, *Adiabatic deformation and strain localization*, in *Shock waves and high-strain rate phenomenon in metals*, M.A. Meyers and L.E. Murr, Editors. 1981, Plenum Press: New York.

96.   Tzou, D.Y., *A unified field approach for heat conduction from macro-to micro-scales.* Journal of Heat Transfer, 1995. **117**: p. 8-16.

97.   *ABAQUS^{TM} 6.2-1, user manual*. 2001, Hibbitt, Karlsson & Soerensen, Pawtucket, RI: Pawtucket, RI.

98.   *ABAQUS^{TM} 6.3, user manual*. 2003, Hibbitt, Karlsson & Soerensen: Hibbitt, Karlsson & Soerensen, Pawtucket, RI.

99.   Johnson, G.R. and W.H. Cook. *A constitutive model and data for metals subjected to large strains, high strain rates, and high temperatures*. in *Proceedings of Seventh International Symposium on Ballistics*. 1983. The Netherlands: The Hague.

100.   Kustas, F.M. and M.S. Misra, *Friction and wear of titanium alloys*, in *ASM Handbook- Friction, lubrication and wear technology*. 1992, ASM International: Materials Park, OH. p. 778-784.

101.   Jones, W.R., et al., *The effects of metals and inhibitors on thermal oxidative degradation reactions of unbranched perfluoroalkyl ethers*. Industrial & Engineering Chemistry Product Research and Development, 1985. **24**: p. 417-420.

102.   *Fretting and Wear Resistance Coatings for Turbine Engine Applications*. 1998, Analytical Services and Materials, INC, Report No. AS&M-r74-98-01.

103. Winer, W.O., *Molybdenum Disilphide as a Lubricant: A Review of the Fundamental Knowledge.* Wear, 1967. **10**: p. 422-452.

104. Meletis, E.I., A. Erdemir, and G.R. Fenske, *Tribological characteristics of DLC films and duplex plasma nitriding/DLC coating treatments.* Surface and Coatings Technology, 1995. **73**(1-2): p. 39-45.

105. Liu, Y., A. Erdemir, and E.I. Meletis, *Study of the wear mechanism of diamond-like carbon films.* Surface and Coatings Technology, 1996. **82**(1-2): p. 48-56.

106. Kustas, F.M., et al., *Diamondlike carbon coatings on Ti-6Al-4V.* STLE Tribology Transactions, 1993. **36**(1): p. 113-119.

107. Aisenberg, S. and R. Chabot, *Ion- beam deposition of thin films of diamondlike carbon.* Journal of Applied Physics, 1971. **7**: p. 2953-2958.

108. Seitzman, L.E., R.N. Bolster, and I.L. Singer, *IBAD MoS$_2$ lubrication of titanium alloys.* Surface and Coatings Technology, 1996. **78**(1): p. 10-13.

109. Seitzman, L.E., R.N. Bolster, and I.L. Singer, *Effects of temperature and ion-to-atom ratio on the orientation of IBAD MoS2 coatings.* Thin Solid Films, 1995. **260**(2): p. 143-147.

110. Jayaram, G., et al., *Ultrahigh vacuum high resolution transmission electron microscopy of sputter-deposited MoS2 thin films.* Surface and Coatings Technology, 1994. **68-69**: p. 439-445.

111. Aubert, A., et al., *Preparation and properties of MoSx films grown by d.c. magnetron sputtering.* Surface and Coatings Technology, 1990. **41**(1): p. 127-134.

112. Didziulis, S.V. and P.D. Fleischauer, *Chemical and tribological studies of MoS$_2$ films on SiC substrates.* Surface and Coatings Technology, 1990. **43-44**(652-662).

113. Renevier, N.M., et al., *Advantages of using self-lubricating, hard, wear-resistant MoS$_2$-based coatings.* Surface and Coatings Technology, 2001. **142-144**: p. 67-77.

114. Renevier, N.M., et al., *Performance of MoS2/metal composite coatings used for dry machining and other industrial applications.* Surface and Coatings Technology, 2000. **123**: p. 84-91.

115. Renevier, N.M., et al., *Performance and limitations of MoS$_2$ /Ti composite coated inserts.* Surface and Coatings Technology, 2003. **172**: p. 13-23.

116. Fox, V., J. Hampshire, and D. Teer, *MoS$_2$/metal composite coatings deposited by closed-field unbalanced magnetron sputtering: tribological properties and industrial uses.* Surface and Coatings Technology, 1999. **112**(1-3): p. 118-122.

117. Fleischauer, P.D., *Fundamental aspects of the electronic structure, materials properties and lubrication performance of sputtered MoS2 films.* Thin Solid Films, 1987. **154**(1-2): p. 309-322.

118. Levy, F. and J. Moser, *High-resolution cross-sectional studies and properties of molybdenite coatings.* Surface and Coatings Technology, 1994. **68-69**: p. 433-438.

119. Lince, J.R. and M.R. Hilton, *Metal incorporation in sputter–deposited MoS2 films studied by extended x–ray adsorption fine structure.* Journal of Materials Research, 1995. **10**(8): p. 2091-2105.

120. Hilton, M.R., G. Jayaram, and L.D. Marks, *Microstructure of cosputter-deposited metal-and oxide-MoS$_2$ solid lubricant thin films.* Journal of Materials Research, 1998. **13**(4): p. 1022-1032.

121. Simmonds, M.C., et al., *Structural, morphological, chemical and tribological investigations of sputter deposited MoSx/metal multilayer coatings.* Surface and Coatings Technology, 1998. **108-109**(1-3): p. 340-344.

122. Jing, Y., J. Luo, and S. Pang, *Effect of Ti or TiN codeposition on the performance of MoS$_2$-based composite coatings.* Thin Solid Films, 2004. **461**: p. 288-293.

123. Weise, G., et al., *Influence of magnetron sputtering process parameters on wear properties of steel/Cr$_3$Si or Cr/MoS$_x$*. Surface and Coatings Technology, 1995. **76-77**: p. 382-392.

124. Jayaram, G., L.D. Marks, and M.R. Hilton, *Nanostructure of Au-20% Pd layers in MoS2 multilayer solid lubricant films*. Surface and Coatings Technology, 1995. **76-77**(2): p. 393-399.

125. Gilmore, R., et al., *Preparation and characterization of low-friction TiB2-based coatings by incorporation of C or MoS2*. Surface and Coatings Technology, 1998. **105**(1-2): p. 45-50.

126. Watanabe, S., S. Miyake, and M. Murakawa, *Tribological properties of cubic, amorphous and hexagonal boron nitride films*. Surface and Coatings Technology, 1991. **49**(1-3): p. 406-410.

127. Lelonis, D.A., J.W. Tereshko, and C.M. Anderson, *Boron nitride powder- A high performance alternative for solid lubrication*. GE Advanced Ceramics, Pub. No. 81506 (09/03), 2003.

128. Kimura, Y., et al., *Boron nitride as a lubricant additive*. Wear, 1999. **232**(2): p. 199-206.

129.   Westergard, R., et al., *Sliding wear and friction of Si3N4-SiC-based ceramic composites containing hexagonal boron nitride.* Proceedings of the Institution of Mechanical Engineers, Part J: Journal of Engineering Tribology, 1998. **212**(5): p. 381-387.

130.   Pushpavanam, M. and S.R. Natarajan, *Nickel-Boron Nitride Electrocomposites.* Metal Finishing, 1995: p. 97-99.

131.   Jarosinski, W. *High temeprature boron nitride abradable materials.* in *Thermal Spray Conference.* 1992: ASM International.

132.   Herr, W., et al., *Fundamental properties and wear resistance of r.f.-sputtered TiB2 and Ti(B,N) coatings.* Materials Science & Engineering A, 1991. **A140**(1-2): p. 616-624.

133.   He, J.L., et al., *Improved anti-wear performance of nanostructured titanium boron nitride coatings.* Wear, 2001. **249**(5-6): p. 498-502.

134.   Herrmann, E., *Revealing the Structure of Thermally Sprayed WC-Co 88/12 and NiCrBSi Coatings for Wear Resistance.* Praktische Metallographie, 1983. **20**(8): p. 371-387.

135. Kreye, H., G. Bechtloff, and H. Bick, *Study on the Thermal Deposition of WC-Co with a Hypersonic Spray System.* Metall, 1983. **37**(3): p. 237-239.

136. Sandt, A., *Wear Behavior of Thermally Sprayed Mo and WC/Co Layers under Sliding and Abrasive Wear Conditions.* Metall, 1984. **38**(10): p. 941-946.

137. de Villiers Lovelock, H.L., *Powder/processing/structure relationships in WC-Co thermal spray coatings: A review of the published literature.* Journal of Thermal Spray Technology, 1998. **7**(3): p. 357-373.

138. Lima, R.S., et al., *Microstructural Characteristics of Cold-Sprayed nanostrucred WC-Co Coatings.* Thin Solid Films, 2002. **416**: p. 129-135.

139. Kang, H.K. and S.B. Kang, *Tungsten/copper composite deposits produced by a cold spray.* Scripta Materialia, 2003. **49**(12): p. 1169-1174.

140. Li, C.-J., et al. *Characterization of microstructure of nanostructured Fe-Si coating deposited by cold spraying.* in *Proceedings of the International Thermal Spray Conference*. 2004. Osaka, Japan: ASM International.

141. Morimoto, J., et al., *Improvement of solid cold sprayed TiO2-Zn coating with direct diode laser.* Vacuum, 2004. **73**(3-4): p. 527-532.

142.   Lee, H.Y., et al., *Cold spray of SiC and Al2O3 with soft metal incorporation: A technical contribution.* Journal of Thermal Spray Technology, 2004. **13**(2): p. 184-189.

143.   Lee, H.H.Y., *Correlation between Al$_2$O$_3$ particles and interface of Al-Al$_2$O$_3$ coatings by cold spray.* Applied Surface Science, 2005. **252**(5): p. 1891-1898.

144.   Zhao, Z.B., B.A. Gillispie, and J.R. Smith, *Coating depostion by the kinetic spray process.* Surface and Coatings Technology, 2006.

145.   Walia, P., Development of Ni-based Self-Lubricating Composite Coatings for Ti-6Al-4V Dovetail Joints using the Cold Spray Process, M.S. Thesis, The Pennsylvania State University, 2006.

Appendix A

Raw Data

A.1 Force Calculations

Force calculation for graphite particle (diameter = 20 μm)

Radius (μm)	Radius (m)	Volume (m^3)	Density (Kg/m^3)	Mass (Kg)	Velocity (m/s)	Time (s)	Acceleration (m/s^2)	Force (N)
10	1.00E-05	4.19E-15	1.81E+03	8E-12	200	1.00E-06	2.00E+08	1.52E-03
10	1.00E-05	4.19E-15	1.81E+03	8E-12	250	1.00E-06	2.50E+08	1.89E-03
10	1.00E-05	4.19E-15	1.81E+03	8E-12	300	1.00E-06	3.00E+08	2.27E-03
10	1.00E-05	4.19E-15	1.81E+03	8E-12	350	1.00E-06	3.50E+08	2.65E-03
10	1.00E-05	4.19E-15	1.81E+03	8E-12	400	1.00E-06	4.00E+08	3.03E-03
10	1.00E-05	4.19E-15	1.81E+03	8E-12	450	1.00E-06	4.50E+08	3.41E-03
10	1.00E-05	4.19E-15	1.81E+03	8E-12	500	1.00E-06	5.00E+08	3.79E-03
10	1.00E-05	4.19E-15	1.81E+03	8E-12	550	1.00E-06	5.50E+08	4.17E-03
10	1.00E-05	4.19E-15	1.81E+03	8E-12	600	1.00E-06	6.00E+08	4.55E-03
10	1.00E-05	4.19E-15	1.81E+03	8E-12	650	1.00E-06	6.50E+08	4.93E-03
10	1.00E-05	4.19E-15	1.81E+03	8E-12	700	1.00E-06	7.00E+08	5.30E-03
10	1.00E-05	4.19E-15	1.81E+03	8E-12	750	1.00E-06	7.50E+08	5.68E-03
10	1.00E-05	4.19E-15	1.81E+03	8E-12	800	1.00E-06	8.00E+08	6.06E-03
10	1.00E-05	4.19E-15	1.81E+03	8E-12	850	1.00E-06	8.50E+08	6.44E-03
10	1.00E-05	4.19E-15	1.81E+03	8E-12	900	1.00E-06	9.00E+08	6.82E-03
10	1.00E-05	4.19E-15	1.81E+03	8E-12	950	1.00E-06	9.50E+08	7.20E-03
10	1.00E-05	4.19E-15	1.81E+03	8E-12	1000	1.00E-06	1.00E+09	7.58E-03

Force calculation for Ni coating in CPT5 composite particle

Velocity (m/s)	Radius (µm)	Radius (m)	Volume (m^3)	Density (Kg/m^3)	Mass (Kg)	Force (N)
200	15	0.000015	9.94E-15	8.91E+03	8.86E-11	1.77E-02
250	15	0.000015	9.94E-15	8.91E+03	8.86E-11	2.21E-02
300	15	0.000015	9.94E-15	8.91E+03	8.86E-11	2.66E-02
350	15	0.000015	9.94E-15	8.91E+03	8.86E-11	3.10E-02
400	15	0.000015	9.94E-15	8.91E+03	8.86E-11	3.54E-02
450	15	0.000015	9.94E-15	8.91E+03	8.86E-11	3.99E-02
500	15	0.000015	9.94E-15	8.91E+03	8.86E-11	4.43E-02
550	15	0.000015	9.94E-15	8.91E+03	8.86E-11	4.87E-02
600	15	0.000015	9.94E-15	8.91E+03	8.86E-11	5.32E-02
650	15	0.000015	9.94E-15	8.91E+03	8.86E-11	5.76E-02
700	15	0.000015	9.94E-15	8.91E+03	8.86E-11	6.20E-02
750	15	0.000015	9.94E-15	8.91E+03	8.86E-11	6.64E-02
800	15	0.000015	9.94E-15	8.91E+03	8.86E-11	7.09E-02
850	15	0.000015	9.94E-15	8.91E+03	8.86E-11	7.53E-02
900	15	0.000015	9.94E-15	8.91E+03	8.86E-11	7.97E-02
950	15	0.000015	9.94E-15	8.91E+03	8.86E-11	8.42E-02
1000	15	0.000015	9.94E-15	8.91E+03	8.86E-11	8.86E-02

Force calculation for Ni coating in CPT10 composite particle

Velocity (m/s)	Radius (μm)	Radius (m)	Volume (m^3)	Density (Kg/m^3)	Mass (Kg)	Force (N)
200	20	0.00002	2.93E-14	8.91E+03	2.61E-10	5.22E-02
250	20	0.00002	2.93E-14	8.91E+03	2.61E-10	6.53E-02
300	20	0.00002	2.93E-14	8.91E+03	2.61E-10	7.83E-02
350	20	0.00002	2.93E-14	8.91E+03	2.61E-10	9.14E-02
400	20	0.00002	2.93E-14	8.91E+03	2.61E-10	1.04E-01
450	20	0.00002	2.93E-14	8.91E+03	2.61E-10	1.18E-01
500	20	0.00002	2.93E-14	8.91E+03	2.61E-10	1.31E-01
550	20	0.00002	2.93E-14	8.91E+03	2.61E-10	1.44E-01
600	20	0.00002	2.93E-14	8.91E+03	2.61E-10	1.57E-01
650	20	0.00002	2.93E-14	8.91E+03	2.61E-10	1.70E-01
700	20	0.00002	2.93E-14	8.91E+03	2.61E-10	1.83E-01
750	20	0.00002	2.93E-14	8.91E+03	2.61E-10	1.96E-01
800	20	0.00002	2.93E-14	8.91E+03	2.61E-10	2.09E-01
850	20	0.00002	2.93E-14	8.91E+03	2.61E-10	2.22E-01
900	20	0.00002	2.93E-14	8.91E+03	2.61E-10	2.35E-01
950	20	0.00002	2.93E-14	8.91E+03	2.61E-10	2.48E-01
1000	20	0.00002	2.93E-14	8.91E+03	2.61E-10	2.61E-01

Force calculation for Ni coating in CPT20 composite particle

Velocity (m/s)	Radius (μm)	Radius (m)	Volume (m^3)	Density (Kg/m^3)	Mass (Kg)	Force (N)
200	30	0.00003	1.09E-13	8.91E+03	9.70E-10	1.94E-01
250	30	0.00003	1.09E-13	8.91E+03	9.70E-10	2.42E-01
300	30	0.00003	1.09E-13	8.91E+03	9.70E-10	2.91E-01
350	30	0.00003	1.09E-13	8.91E+03	9.70E-10	3.39E-01
400	30	0.00003	1.09E-13	8.91E+03	9.70E-10	3.88E-01
450	30	0.00003	1.09E-13	8.91E+03	9.70E-10	4.36E-01
500	30	0.00003	1.09E-13	8.91E+03	9.70E-10	4.85E-01
550	30	0.00003	1.09E-13	8.91E+03	9.70E-10	5.33E-01
600	30	0.00003	1.09E-13	8.91E+03	9.70E-10	5.82E-01
650	30	0.00003	1.09E-13	8.91E+03	9.70E-10	6.30E-01
700	30	0.00003	1.09E-13	8.91E+03	9.70E-10	6.79E-01
750	30	0.00003	1.09E-13	8.91E+03	9.70E-10	7.27E-01
800	30	0.00003	1.09E-13	8.91E+03	9.70E-10	7.76E-01
850	30	0.00003	1.09E-13	8.91E+03	9.70E-10	8.24E-01
900	30	0.00003	1.09E-13	8.91E+03	9.70E-10	8.73E-01
950	30	0.00003	1.09E-13	8.91E+03	9.70E-10	9.21E-01
1000	30	0.00003	1.09E-13	8.91E+03	9.70E-10	9.70E-01

Force calculation for nickel particle (diameter = 40 μm)

Radius (μm)	Radius (m)	Volume (m^3)	Density (Kg/m^3)	Mass (Kg)	Velocity (m/s)	Time (s)	Acceleration (m/s^2)	Force (N)
20	2.00E-05	3.35E-14	8.91E+03	3E-10	200	1.00E-06	2.00E+08	5.97E-02
20	2.00E-05	3.35E-14	8.91E+03	3E-10	250	1.00E-06	2.50E+08	7.46E-02
20	2.00E-05	3.35E-14	8.91E+03	3E-10	300	1.00E-06	3.00E+08	8.95E-02
20	2.00E-05	3.35E-14	8.91E+03	3E-10	350	1.00E-06	3.50E+08	1.04E-01
20	2.00E-05	3.35E-14	8.91E+03	3E-10	400	1.00E-06	4.00E+08	1.19E-01
20	2.00E-05	3.35E-14	8.91E+03	3E-10	450	1.00E-06	4.50E+08	1.34E-01
20	2.00E-05	3.35E-14	8.91E+03	3E-10	500	1.00E-06	5.00E+08	1.49E-01
20	2.00E-05	3.35E-14	8.91E+03	3E-10	550	1.00E-06	5.50E+08	1.64E-01
20	2.00E-05	3.35E-14	8.91E+03	3E-10	600	1.00E-06	6.00E+08	1.79E-01
20	2.00E-05	3.35E-14	8.91E+03	3E-10	650	1.00E-06	6.50E+08	1.94E-01
20	2.00E-05	3.35E-14	8.91E+03	3E-10	700	1.00E-06	7.00E+08	2.09E-01
20	2.00E-05	3.35E-14	8.91E+03	3E-10	750	1.00E-06	7.50E+08	2.24E-01
20	2.00E-05	3.35E-14	8.91E+03	3E-10	800	1.00E-06	8.00E+08	2.39E-01
20	2.00E-05	3.35E-14	8.91E+03	3E-10	850	1.00E-06	8.50E+08	2.54E-01
20	2.00E-05	3.35E-14	8.91E+03	3E-10	900	1.00E-06	9.00E+08	2.69E-01
20	2.00E-05	3.35E-14	8.91E+03	3E-10	950	1.00E-06	9.50E+08	2.83E-01
20	2.00E-05	3.35E-14	8.91E+03	3E-10	1000	1.00E-06	1.00E+09	2.98E-01

Appendix B

Sample Input Files

B.1 Composite Particle

```
/PREP7

!************** ELEMENT DEFINITIONS **************!

ET,1,PLANE182

KEYOPT,1,1,0  $ KEYOPT,1,3,1  $ KEYOPT,1,6,0  $ KEYOPT,1,10,0

!*

ET,2,TARGE169

KEYOPT,2,2,0  $ KEYOPT,2,3,0 $ KEYOPT,2,4,0

!*

ET,3,CONTA171

KEYOPT,3,1,0  $ KEYOPT,3,2,0  $ KEYOPT,3,3,0  $ KEYOPT,3,4,0

KEYOPT,3,5,2  $ KEYOPT,3,6,0  $ KEYOPT,3,7,0  $ KEYOPT,3,8,0

KEYOPT,3,9,1  $ KEYOPT,3,10,1  $ KEYOPT,3,11,0  $ KEYOPT,3,12,0

!*****************************************!

!*********** REAL CONSTANTS*************!

R,1,,,0.5, ,,  $ RMORE,,,, ,,  $ RMORE,,,, ,,  $ RMORE,,,, ,,

!* ***************************************!

!************** MATERIAL PROPERTIES************!
```

MPTEMP,,,,,,,, $ MPTEMP,1,0

MPDATA,EX,1,,116e9

MPDATA,PRXY,1,,0.32

TB,BKIN,1,1,2,1

TBTEMP,0

TBDATA,,830e6,62e9,,,,

MPTEMP,,,,,,,, $ MPTEMP,1,0

MPDATA,DENS,1,,4510

!* !*>>>> MATERIAL PROPERTIES FOR Ti-6Al-4V<<<<*!

MPTEMP,,,,,,,, $ MPTEMP,1,0

MPDATA,EX,2,,170e9

MPDATA,PRXY,2,,0.31

TB,BKIN,2,1,2,1

TBTEMP,0

TBDATA,,35e6,138e9,,,,

MPTEMP,,,,,,,, $ MPTEMP,1,0

MPDATA,DENS,2,,8908

!*>>>>MATERIAL PROPERTIES FOR NICKEL<<<<*!

MPTEMP,,,,,,,, $ MPTEMP,1,0

MPDATA,EX,3,,9.5e9

MPDATA,PRXY,3,,0.18

TB,BKIN,3,1,2,1

TBTEMP,0

TBDATA,,42e6,0.5e9,,,,

MPTEMP,,,,,,,, $ MPTEMP,1,0

MPDATA,DENS,3,,1810

!*>>>>MATERIAL PROPERTIES FOR GRAPHITE<<<<*!

```
!******************* GEOMETRY*****************!

*SET,radius,80e-6  !*>>> length of substrate<<<*!

*SET,thick,80e-6  !*>>> width of substrate<<<*!

*SET,inter,1.6e-10  !*>>> over lap<<<*!

*SET,penet,thick-inter

*SET,partrad,ENTER VALUE  !*>>> Total radius of particle<<<*!

*SET,bnrad,ENTER VALUE !*>>>radius of lube particle<<<*!

*SET,sphY,thick+(partrad-inter)

*SET,twosphY,thick+2*(partrad-inter)

CYL4,0,sphY,bnrad

LSTR,     2,     4

ASBL,     1,     5

ADELE,     3, , ,1

K, ,0,sphY,0,  $ K, ,0,penet,0,  $ K, ,0,twosphY,0,  $ K, ,partrad,sphY,0,

!*

LARC,5,6,7,partrad,

LSTR,     5,     4

LSTR,     6,     2

LPLOT

FLST,2,5,4  $ FITEM,2,3  $ FITEM,2,4  $ FITEM,2,1

FITEM,2,6  $ FITEM,2,2

AL,P51X

APLOT

RECTNG,0,radius,0,thick

!***********************************************!

!*****************MESHING********************!

TYPE,  1
```

```
MAT,      1

REAL,      1

ESYS,      0

SECNUM,

!*

MSHAPE,0,2D

MSHKEY,1

!*

CM,_Y,AREA

ASEL, , , ,      3

CM,_Y1,AREA

CHKMSH,'AREA'

CMSEL,S,_Y

!*

AMESH,_Y1

!*

CMDELE,_Y

CMDELE,_Y1

CMDELE,_Y2

!*

FLST,5,1,5,ORDE,1

FITEM,5,3

CM,_Y,AREA

ASEL, , , ,P51X

CM,_Y1,AREA

CMSEL,S,_Y

CMDELE,_Y
```

```
!*

!*

AREFINE,_Y1, , ,3,0,1,1

CMDELE,_Y1

!*

FLST,5,1,5,ORDE,1

FITEM,5,3

CM,_Y,AREA

ASEL, , , ,P51X

CM,_Y1,AREA

CMSEL,S,_Y

CMDELE,_Y

!*

!*

AREFINE,_Y1, , ,1,0,1,1

CMDELE,_Y1

!*

APLOT

TYPE,   1

MAT,     3

REAL,     1

ESYS,     0

SECNUM,

!*

MSHKEY,0

!*

CM,_Y,AREA
```

```
ASEL, , , ,     2

CM,_Y1,AREA

CHKMSH,'AREA'

CMSEL,S,_Y

!*

AMESH,_Y1

!*

CMDELE,_Y

CMDELE,_Y1

CMDELE,_Y2

!*

APLOT

TYPE,  1

MAT,     2

REAL,    1

ESYS,    0

SECNUM,

!*

CM,_Y,AREA

ASEL, , , ,     1

CM,_Y1,AREA

CHKMSH,'AREA'

CMSEL,S,_Y

!*

AMESH,_Y1

!*

CMDELE,_Y
```

```
CMDELE,_Y1

CMDELE,_Y2

!*

FLST,5,1,4,ORDE,1

FITEM,5,2

CM,_Y,LINE

LSEL, , , ,P51X

CM,_Y1,LINE

CMSEL,S,_Y

CMDELE,_Y

!*

!*

LREFINE,_Y1, , ,1,1,1,1

CMDELE,_Y1

!*

/UI,MESH,OFF

!*********************************************!


!******************** CONTACT ELEMENTS********************!

LSEL,S, , ,      9

NSLL,S,1

TYPE,   2

MAT,     1

REAL,     1

ESYS,     0

SECNUM,

TSHAP,LINE
```

```
!*

FLST,5,25,1,ORDE,17

FITEM,5,5   $ FITEM,5,8  $ FITEM,5,-10  $ FITEM,5,18  $ FITEM,5,-19

FITEM,5,21  $ FITEM,5,30 $ FITEM,5,-31 $ FITEM,5,33  $ FITEM,5,-36

FITEM,5,172  $ FITEM,5,-174  $ FITEM,5,177 $ FITEM,5,-181 $ FITEM,5,184

FITEM,5,215  $ FITEM,5,-217

CM,_Y,NODE

NSEL, , , ,P51X

CM,_Y1,NODE

CMSEL,S,_Y

!*

CMSEL,,_Y1

ESURF, ,TOP,

CMSEL,,_Y

CMDELE,_Y

CMDELE,_Y1

!*

ALLSEL,ALL

LSEL,S, , ,     2

NSLL,S,1

TYPE,   3

MAT,     2

REAL,     1

ESYS,     0

SECNUM,

TSHAP,LINE

!*
```

FLST,5,46,1,ORDE,10

FITEM,5,694 $ FITEM,5,697 $ FITEM,5,700 $ FITEM,5,-713

FITEM,5,725 $ FITEM,5,-726 $ FITEM,5,728 $ FITEM,5,-729

FITEM,5,733 $ FITEM,5,-758

CM,_Y,NODE

NSEL, , , ,P51X

CM,_Y1,NODE

CMSEL,S,_Y

!*

CMSEL,,_Y1

ESURF, ,TOP,

CMSEL,,_Y

CMDELE,_Y

CMDELE,_Y1

!* *******************************!

ALLSEL,ALL

FINISH

!**************** SOLUTION***************!

/SOL

!*

ANTYPE,4   !*>>>>> ANALYSIS TYPE<<<<<*!

!*

TRNOPT,FULL

LUMPM,0

!*

NLGEOM,1

NSUBST,X,X,X !*>>>>> NUMBER OF SUBSTEPS<<<<<*!

```
AUTOTS,1

KBC,0    !*>>>>> RAMPED LOADING<<<<<*!

NEQIT,X  !*>>>>> EQUILIBRIUM ITERATIONS<<<<<*!

TIME,1e-6    !*>>>>> TIME<<<<<*!

!********* BOUNDARY CONDITIONS*****************!

NSEL,S,LOC,X,0

FLST,2,58,1,ORDE,40

FITEM,2,1  $ FITEM,2,8  $ FITEM,2,11  $ FITEM,2,-12

FITEM,2,20 $ FITEM,2,23  $ FITEM,2,27 $ FITEM,2,37

FITEM,2,-38  $ FITEM,2,41 $ FITEM,2,-42 $ FITEM,2,49

FITEM,2,51  $ FITEM,2,182   $ FITEM,2,-183  $ FITEM,2,185

FITEM,2,-186 $ FITEM,2,191 $ FITEM,2,-194  $ FITEM,2,207

FITEM,2,-209  $ FITEM,2,211 $ FITEM,2,627  $ FITEM,2,634

FITEM,2,-645  $ FITEM,2,694  $ FITEM,2,-699  $ FITEM,2,723

FITEM,2,-724  $ FITEM,2,727 $ FITEM,2,730 $ FITEM,2,-732

FITEM,2,772 $ FITEM,2,775  $ FITEM,2,-776  $ FITEM,2,781

FITEM,2,-782  $ FITEM,2,787  $ FITEM,2,792  $ FITEM,2,795

!*

/GO

D,P51X, , , , , ,UX, , , , ,

ALLSEL,ALL

NSEL,S,LOC,Y,0

FLST,2,25,1,ORDE,18

FITEM,2,1  $ FITEM,2,-4  $ FITEM,2,24  $ FITEM,2,26

FITEM,2,28  $ FITEM,2,44  $ FITEM,2,-45  $ FITEM,2,47

FITEM,2,-48 $ FITEM,2,50 $ FITEM,2,52  $ FITEM,2,197

FITEM,2,-200 $ FITEM,2,203 $ FITEM,2,-206 $ FITEM,2,210
```

FITEM,2,212 $ FITEM,2,-214 $

!* ***!

/GO

D,P51X, , , , , ,ALL, , , , ,

ALLSEL,ALL

!**************FORCE APPLICATION***********!

ASEL,S, , ,   2

NSLA,S,1

FLST,2,41,1,ORDE,2

FITEM,2,626

FITEM,2,-666

!*

/GO

F,P51X,FY,-X !*>>>>>>>>>> FORCE ON LUBE<<<<<<<<<<<<<<*!

ALLSEL,ALL

ASEL,S, , ,   1

NSLA,S,1

FLST,2,269,1,ORDE,6

FITEM,2,626

FITEM,2,-633

FITEM,2,641

FITEM,2,-645

FITEM,2,667

FITEM,2,-922

!*

/GO

F,P51X,FY,-X !*>>>>>>>>> FORCE ON NICKEL COATING<<<<<<<*!

```
ALLSEL,ALL

LPLOT

FLST,5,2,4,ORDE,2

FITEM,5,1

FITEM,5,4

LSEL,S, , ,P51X

NSLL,S,1

FLST,2,15,1,ORDE,4

FITEM,2,626

FITEM,2,-634

FITEM,2,646

FITEM,2,-651

FLST,2,15,1,ORDE,4

FITEM,2,626

FITEM,2,-634

FITEM,2,646

FITEM,2,-651

!*

/GO

F,P51X,FY,-1.68E-02 !*>>>>>> FORCE AT INTERFACE<<<<<<<<*!

ALLSEL,ALL

LSWRITE,1,
```

Appendix C

Non-Technical Abstract

Thermal spray technology is used extensively in defense, aerospace and gas turbine industries. Typical applications include fabrication of components, preparation of protective surfaces, refurbishment of mis-machined and service damaged parts, etc. Recently, a new thermal spray process, known as cold spray, has been introduced to produce metal alloy and composite coatings with superior qualities. Cold spray process uses high velocity rather than high temperature to produce coatings, and thereby avoid/minimize many deleterious high temperature reactions, which are characteristics of typical thermal sprayed coatings.

In this research, cold spray process is investigated for the development of self-lubricating coatings on titanium alloy. Two lubricant powders- boron nitride (BN) and molybdenum disulfide (MoS_2) are used in conjunction with nickel powder to develop self-lubricating coatings. It has been observed that the key for the coatings to be self-lubricating is the presence of lubricant powders. As lubricant powders are light and brittle in nature as compared to nickel powder, they accelerate at a higher rate resulting in minimal coating deposition. To alleviate this problem, a composite powder with a lubricant core and nickel coating is used to develop the coating.

For better understanding of the process, it is necessary to study the impact of the composite particles. Computer modeling of process provides a cost-effective technique

for the optimization of the process. A simple computer model based on material behavior when subjected to mechanical load is used to predict the optimum particle velocity for producing self-lubricating coatings.

For the first time, the cold spray process is used to develop Ni-MoS$_2$ and Ni-BN self-lubricating coatings. The modeling results predict a decrease in critical particle velocity (required for bonding) with an increase of nickel coating in the composite particle. Overall, present research provides a strong foundation for composite particle deposition via cold spray process.

VITA

Gaurav Aggarwal

<u>Education:</u>

Ph.D. Engineering Science and Mechanics, August 2007

The Pennsylvania State University, University Park, PA, USA

M.S. Engineering Science, December 2003

The Pennsylvania State University, University Park, PA, USA

B.E. Metallurgical Engineering

Punjab Engineering College, Chandigarh, INDIA

<u>Employment and Internship Record:</u>

Applications Development Engineer, July 2006-present

Diamond Innovations, Columbus, OH, USA

Research Assistant, August 2002-June 2006

CISP, The Pennsylvania State University, University Park, PA, USA

<u>Recent Publications:</u>

G. Aggarwal, I. Smid, A.E. Segall, "Impact-Contact Modeling of Particle Bonding in the Cold Gas Dynamic Spray Process", TMS 2006 Annual Meeting, Orlando, Feb 25-March 1, 2007.

G. Aggarwal, P. Walia, A.E. Segall, I. Smid, T. Eden, "Development of Self-Lubricating Coatings for Ti-6Al-4V Dovetails using a High-Velocity-Particle-Consolidation (HVPC) Process", International Thermal Spray Conference, Seattle, May 15-18, 2006.

G. Aggarwal, I. Smid, A.E. Segall, "Modeling of Deformation and Bonding of Composite Particle during Cold-Spray Deposition", TMS 2006 Annual Meeting, San Antonio, March 12-16, 2006.